Spin and Parity of the Higgs Boson Near $m_H = 126\,\mathrm{GeV/c^2}$ in the $H \to ZZ \to 4\ell$ Channel and a Search for a Doubly Charged Higgs with the CMS Detector at the LHC

by

Donald Austin Belknap

A dissertation submitted in partial fulfillment of

the requirements for the degree of

Doctor of Philosophy

(Physics)

at the

University of Wisconsin – Madison

2015

Defended on August 17, 2015

Dissertation approved by the following members of the Final Oral Committee:

Wesley H. Smith · Bjørn Wiik Professor of Physics

Sridhara R. Dasu · Professor of Physics

Matthew F. Herndon · Professor of Physics

Lisa L. Everett · Professor of Physics

Terry S. Millar · Professor Emeritus of Mathematics

Abstract

Presented here is an analysis of the spin and parity of the Higgs-like boson near 126 GeV in the ZZ decay channel where the Z bosons decay into two muons or electrons. The analysis utilizes $19.7\,\text{fb}^{-1}$ of 8 TeV proton-proton collision data recorded by the CMS experiment. The Standard Model pure-scalar hypothesis is compared against four alternate spin parity hypotheses. The data are consistent with the Standard Model expectations, and the pseudoscalar hypothesis is excluded at the 95% confidence level.

Additionally, we present a search for a doubly charged Higgs boson, which also utilizes $19.7\,\text{fb}^{-1}$ of 8 TeV proton-proton collision data recorded by CMS. The doubly charged Higgs is a member of an $SU(2)_L$ scalar triplet, and is a Type-II "seesaw" mechanism. We search for a four-lepton final state from Drell-Yan pair production of two left-handed doubly charged Higgs bosons. The branching ratio of the doubly charged Higgs is not determined by the model, so we consider a variety of possible branching ratio scenarios. We exclude possible masses of the doubly charged Higgs between 388 and 585 GeV at the 95% confidence level, depending on the branching ratio scenario.

Acknowledgements

When I began college as a freshman at Rice University, I already had the intention of continuing my education through to a doctorate. I remember thinking I still had nearly 10 years of school ahead of me, which is only now finishing with the writing and defense of this thesis. Reaching this point in my life certainly took a great deal of hard work and effort, but it is no exaggeration to say that I would not be here if it weren't for the steadfast support of my family, friends, colleagues, and educators.

First, I wish to thank my family. To my parents, Don and Diana, for giving me so much love and support throughout my lifetime, and for nurturing my love for science from such an early age. I also want to thank my grandfather, Luis Arredondo, for our fascinating discussions about relativity when I was a child, which inspired me to study physics. I want to thank my little sister, Jordan, for being so wonderful and supportive, and for putting up with my antics as we grew up together. Finally, I want to thank my uncle, Steve Belknap, for guiding me through some very tough periods while I completed my degree.

I would also like to thank my seventh grade science teacher, Chris Vanderlinden, for successfully teaching seventh-graders the basics of nuclear science, and for getting me interested in the subject.

I've had so many friends that have been an integral part of my life, and I want to thank all of them. In particular, I want to thank my friends from CERN: Ashley WennersHerron, Amanda Kruse, Stephen Cole, Scarlet Norberg, Blake Burghgrave, Sarah Charley, Chris Martin, Kristin Kaltenhauser, and Eric Takasugi. I also want to thank my girlfriend, Melissa Stoner. She has had a wonderful impact on my life, and I want to thank her for her love and support during the difficult final stages of completing my degree.

I want to extend my thanks to my UW colleagues: to our postdocs, María Cepeda

and Evan Friis; and to my fellow graduate students, Isobel Ojalvo (now a postdoc), Ian Ross, Joshua Swanson, Tom Perry, Aaron Levine, Nate Woods, Laura Dodd, Devin Taylor, Tyler Ruggles, Kenneth Long, and Nick Smith. I especially want to thank María Cepeda for her help and guidance. Additionally, I would like to thank our staff scientists, Pam Klabbers and Sascha Savin.

Finally, I want to thank my professors, Wesley Smith and Sridhara Dasu for the extraordinary opportunity to participate in the CMS experiment at CERN. I never imagined I would travel half way around the world and participate in cutting-edge physics, or be present at CERN during the Higgs discovery announcement. Lastly, I would like to thank them for their guidance and support throughout my graduate career.

Thank you, all!

Contents

List of Figures

List of Tables

1 Introduction

In July 2012, the CMS and ATLAS collaborations at CERN announced the discovery of a Higgs boson. As the particle is crucial to the Standard Model, Peter Higgs and François Englert shared the 2013 Nobel Prize in Physics for its prediction in the 1960's. The Standard Model places constraints on the properties of the Higgs boson. Specifically, it predicts that it has zero spin and even parity. Following its discovery, it is therefore critically important to measure the properties of the Higgs. Presented in this thesis is an analysis examining the spin-parity configuration of the Higgs boson in the $H \to ZZ \to 4\ell$ channel utilizing data from the CMS experiment.

A second analysis presented in this thesis addresses a gap in the Standard Model. Neutrinos are ghostly particles that almost never interact with matter, and are nearly massless. However, they do have a non-zero mass, and this is not accounted for by the Standard Model. One model that accommodates neutrino mass is the addition of a triplet of Higgs bosons to the current spectrum of known particles. The triplet contains a doubly charged Higgs boson, and a search for such a particle utilizing CMS data is presented.

The next section covers some preliminaries: a brief historical overview, relevant quantities and conventions used in high-energy particle physics. Following this is a discussions of fundamental particles, forces, and the Standard Model. The relevant theoretical underpinnings of the spin and parity of the Higgs boson, and the doubly charged Higgs are also discussed.

1.1 From Atoms to Particles

The idea that matter is composed of discrete components is not at all a recent development. Modern atomic theory began with John Dalton in the early 1800's, and it was understood that matter was made of discrete components. It wasn't until the end of the 19th Century that subatomic particles entered the picture with the discovery of the electron by J. J. Thompson. It was believed that electrons were components of atoms, but they were negatively charged whereas atoms were neutral. In 1909, Rutherford directed an experiment in which a beam of alpha particles was aimed at a target of gold foil. Based on the scattering pattern of the alpha particles, it was determined that atoms were mostly empty space, with nearly all of its mass concentrated at a very small, positively charged nucleus. With this, Niels Bohr developed a model of the atom that had the electrons orbiting a central nucleus.

The nucleus of the lightest atom, hydrogen, was called a *proton* by Rutherford. The helium nucleus has two protons, but has four times as much mass as a proton. The extra mass is accounted for by the uncharged *neutron*, which was discovered by Chadwick in 1932. Due to the electromagnetic force, the positively charged protons in the nucleus should fly apart from one another. It was clear that another force was binding them together in the nucleus, which we call the *strong force*.

Classically, the nature of light was understood to be electromagnetic waves, described by Maxwell's equations. In 1900, Max Planck was attempting to explain the spectrum of electromagnetic radiation emanated by hot objects, called *blackbody radiation*. Planck found that the observed spectrum could only be explained if light was quantized, and traveled in discrete packets. Another phenomena, called the *photoelectric effect*, occurs when electromagnetic radiation strikes a metal's surface and ejects an electron. This only occurred when the light's frequency (color) was high enough, and did not depend on the intensity. Einstein's explanation was that light must be quantized, and its energy depends

on its frequency. We call these quanta of light *photons*.

More subatomic particles were discovered throughout the remainder of the 20th century. In 1937 through 1946, the pions were discovered along with the heavier cousin of the electron, the muon. It was later found that the weak force is responsible of the decay of a muon into an electron and two neutrinos. From 1947 through 1960, hundreds of new particles that interact via the strong force were discovered, which we call *hadrons*. In 1964, Gell-Mann and Zweig found that the discovered hadrons could be explained provided they have substructure, and are composed of more primitive components: quarks. It was later revealed that protons and neutrons are composed of quarks as well, and have substructure.

Another problem arose with nuclear beta decay. This is the process in which a radioactive atomic nucleus emits an electron and becomes lighter. If a single nucleus decays into two lighter particles, their energies must be fixed. However, it was observed that the energy of the emitted electron varied considerably. Pauli proposed that this was actually a three-body decay, and the third particle was neutral (so it could not be seen in a detector) and very light. Fermi called this new particle a *neutrino*. In 1933, Fermi presented a model describing an interaction responsible for beta decay that would later become known as the *weak force*.

Fermi's model, though successful at describing beta decay, could not hold at higher energies. In order for it to work, the interaction would need to be mediated by a massive particle. In the 1960's Glashow, Weinberg, and Salam merged the weak force and the electromagnetic force into a single *electroweak* theory. The theory predicted three massive mediator particles for the weak force: $W^{\pm}$ and Z. In 1983, Carlo Rubbia's group announced the discovery of the W, with the discovery of the Z in the months that followed. Electroweak theory hinged on the existence of another particle, the Higgs boson, to give masses to the W and the Z. The Higgs was finally discovered in 2012 by the CMS and ATLAS collaborations at the CERN Large Hadron Collider.

1.2 Kinematics, Decays, and Cross Sections

The particles in high energy physics experiments travel at a significant fraction of the speed of light, so it is necessary to utilize relativistic kinematics to describe their energies and momenta. The speed of a relativistic particle is characterized with the quantities

$$\gamma = \frac{1}{\sqrt{1-\beta^2}} = \frac{E}{mc^2} \tag{1.1}$$

$$\beta = \frac{v}{c} = \frac{pc}{E} \tag{1.2}$$

and the energy of a relativistic particle is given by

$$E = \sqrt{(pc)^2 + (mc^2)^2} = \gamma mc^2 \tag{1.3}$$

In particle physics, matter-energy conversion is commonplace. So, it is convenient to set $c = \hbar = 1$, and express momenta and masses in units of energy. So, $cp \to p$ and $mc^2 \to m$, and are given in units of electron volts ($1\,\text{eV} = 1.602\,176\,57 \times 10^{-19}\,\text{J}$). These are referred to as *natural units* and will be used for the remainder of this thesis. As an example, I weigh 130 lbs or 3.3×10^{28} GeV. Since protons and neutrons have a mass of about 1 GeV, my body is composed of nearly 3.3×10^{28} protons and neutrons. In the Large Hadron Collider, a proton has an energy of 4 TeV for the analyses presented in this thesis. Since a proton has a mass of 938.3 MeV, its Lorentz factor is

$$\gamma = E/m = 1\,\text{TeV}/938.3\,\text{MeV} = 1065.76$$

If such a proton were to wear a watch, it would run 1065.76 times slower than the watch on your own wrist.

The momenta of relativistic particles are expressed as Lorentz four-vectors.

$$p^\mu = \left(E, \vec{p}\right) \tag{1.4}$$

The inner product of this vector is a Lorentz invariant, so its value is the same in all inertial references frames.

$$p^\mu p_\mu = E^2 - \vec{p} \cdot \vec{p} = m^2 \tag{1.5}$$

This quantity is referred to as the *invariant mass*. If a particle decays, and we know the four-momenta of its decay products, we can find the four-momentum of the original particle, and thus its mass.

Most particles have a finite lifetime, and disintegrate into lighter particles. A particle's rate of decay is characterized by its width, Γ, which is given in units of eV. The particle's mean lifetime is $\tau \equiv 1/\Gamma$. A particle may decay into a variety of final states; $Z \to ee$ or $Z \to \mu\mu$, for example. The width of a decay to a specific final state is a *partial width*, and the sum of all possible partial widths is the *total width*. The partial width of a specific decay divided by the total width of the parent particle is the *branching ratio* (BR).

In high-energy physics, we collide beams of particles into one another, and there is some probability that they interact and undergo some scattering process. This probability is characterized by a cross section (σ). If you have two packets of particles, with number N_1 and N_2, the number of scattering events N is given by

$$N = \frac{N_1 N_2}{A}\sigma \tag{1.6}$$

where A is the cross sectional area of the two packets. In a collider experiment, like the LHC, the quantity $N_1 N_2/A$ is constantly increasing with time. This rate is referred to as the instantaneous luminosity, $\mathcal{L}$. So, the total number of scattering events in a collider experiment is given by

$$N = \sigma \int \mathcal{L}\, dt \tag{1.7}$$

where $\mathcal{L}_{int} = \int \mathcal{L}\, dt$ is the integrated luminosity. Cross section and luminosity can be expressed in a natural units, but it is more common to use the *barn*. 1 barn is $10^{-24}\,\mathrm{cm}^2$ or $2568\,\mathrm{GeV}^{-2}$, and is the unit of cross section. Integrated luminosity is given in inverse

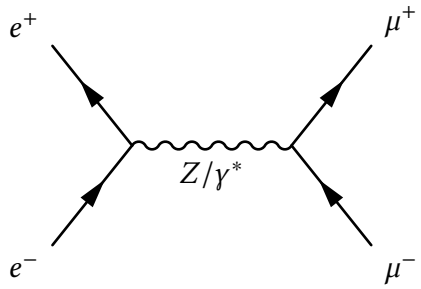

Figure 1.1: The is an example Feynman diagram showing $e^+e^- \to \mu^-\mu^+$. Time flows from left to right in this diagram.

barns (b^{-1}). Instantaneous luminosity can be given in inverse barns per second, but it is more common to express it in units of $cm^{-2}s^{-1}$.

The mathematical framework used to describe the physics of fundamental particles is Quantum Field Theory (QFT), which allows us to incorporate quantum mechanics and special relativity within a single framework. The fields in QFT create and destroy particles, and we define the dynamics of a particular system with a Lorentz-invariant Lagrangian involving the fields. In order to compute observables, such as widths and cross sections, we have to perform a perturbation expansion. This is often accomplished using a diagrammatic method called *Feynman diagrams*, where each topologically distinct diagram is a term in the expansion. An example Feynman diagram of $e^+e^- \to \mu^+\mu^-$ is shown in Figure 1.1. In this thesis, time flows from left to right in Feynman diagrams. Spin-1 bosons are indicated with a wavy line, and spin-0 bosons are indicated with a dashed line. Spin-$1/2$ fermions are indicated with a solid line with an arrow, where the arrow indicates the direction of the fermion's momentum. The momentum of anti-fermions flows backwards in time.

1.3 The Standard Model

Currently, there are four known fundamental forces: the electromagnetic force, weak force, strong force, and gravity (Table 1.1). There are three neutrinos, which only participate in

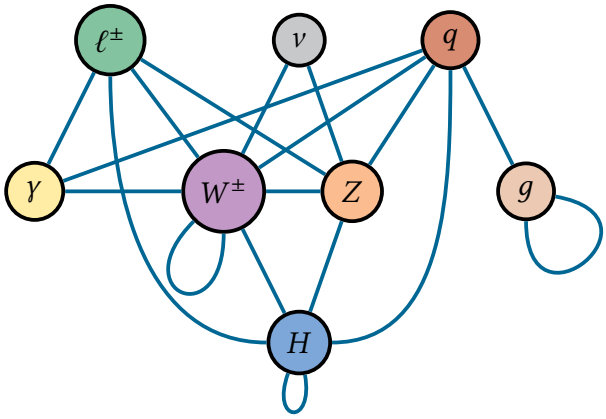

Figure 1.2: This shows the particles and forces of the Standard Model, and which particles they interact with.

weak interactions, three charged leptons which participate in electromagnetic and weak interactions, and six quarks which participate in strong, weak and electromagnetic forces. All of these particles have antiparticles, which have the same mass, but opposite charges. The electron antiparticle is called a *positron* (or anti-electron), the muon antiparticle is the anti-muon, and so on. Conventionally, we refer to a particle and its antiparticle by the particle's original name (e.g. electrons and positrons are referred to collectively as "electrons"), unless the situation merits making the distinction. Since all of these particles have mass, they should, in principle, experience gravity. However, gravity is so extraordinarily weak compared to the other forces that it plays virtually no role in high-energy physics.

Force	Carrier Particle	Mass (GeV)	Relative Strength
Strong	gluon (g)	0	1
Electromagnetic	photon (γ)	0	10^{-2}
Weak	$W^{\pm}$	80.385(15)	10^{-13}
	Z	91.1876(21)	
Gravity	graviton (hypothetical)	0	10^{-42}

Table 1.1: The four known fundamental forces, and their relative strengths [1].

Leptons

The three charged leptons are the electron, muon, and tau (e, μ, and τ), and they carry an electric charge of ±1 times the charge of the positron. Electrons are ubiquitous to everyday life, being responsible for electricity. Electrons are also stable, meaning that they do not decay into any other particles. The muon and tau, however, are not stable, which is why we encounter them so infrequently. The muon has a mean lifetime of 2.196 981 1(22) µs, and the tau, 290.3(5) fs [2]. Each flavor of lepton carries a quantum number called *lepton number*. For instance, the muon has a muon number of +1, and anti-muon has a muon number of -1. Its electron and tau numbers are 0.

A neutrino also carries a lepton number, and as their name suggests, they are neutral and have no electric charge. We do not know what the neutrino masses are, only that they are not zero and extremely small. The electron anti-neutrino is less than 2 eV at the 95% confidence level [2], and the sum of the neutrino masses is less than 0.39 eV at the 95% confidence level [3]. Neutrinos have a very peculiar property where a single neutrino can change flavor, which we call *neutrino oscillations*. Neutrinos propagate through space in one of three mass eigenstates (ν_1, ν_2, ν_3) with masses $m_{1,2,3}$, but they can be observed in any of the three flavor eigenstates (ν_e, ν_μ, ν_τ). Neutrino oscillations are brought about by the mixing of these eigenstates, which we characterize with the unitary Pontecorvo-Maki-Nakagawa-Sakata (PMNS) matrix,

$$U = \begin{pmatrix} 1 & 0 & 0 \\ 0 & c_{23} & s_{23} \\ 0 & -s_{23} & c_{23} \end{pmatrix} \begin{pmatrix} c_{13} & 0 & s_{13}e^{-i\delta} \\ 0 & 1 & 0 \\ -s_{13}e^{i\delta} & 0 & c_{13} \end{pmatrix} \begin{pmatrix} c_{12} & s_{12} & 0 \\ -s_{12} & c_{12} & 0 \\ 0 & 0 & 1 \end{pmatrix} \begin{pmatrix} e^{-i\alpha_1} & 0 & 0 \\ 0 & e^{i\alpha_2} & 0 \\ 0 & 0 & 1 \end{pmatrix} \tag{1.8}$$

where $c_{ij} = \cos\theta_{ij}$, $s_{ij} = \sin\theta_{ij}$, and δ is a CP violating phase. CP symmetry is the situation in which the laws of physics are unchanged if we exchange a particle for its antiparticle (C), and invert spatial coordinates (P). Neutrinos could conceivably be their own antiparticles.

Such neutrinos are called *Majorana neutrinos*, and are not part of the Standard Model. α_1 and α_2 are the Majorana CP violating phases, should neutrinos prove to be Majorana. Current measurements on the mixing angles yield

$$\sin^2\theta_{12} = 0.314(1^{+0.18}_{-0.15}) \qquad \sin^2\theta_{23} = 0.45(1^{+0.35}_{-0.20}) \qquad \sin^2\theta_{13} = 0.8(1^{+2.3}_{-0.8}) \times 10^{-2} \tag{1.9}$$

The CP violating angles haven't been determined by experiment and could take on values between 0 and 2π [4]. The neutrino masses have not been measured individually, but the square of the mass differences have been measured [2]. If $m_1 < m_2 < m_3$, we call this the *normal hierarchy* of neutrino masses. The case where $m_3 < m_1 < m_2$ is called the *inverted hierarchy*.

With the exception of neutrino oscillations, lepton number is a conserved quantity. There are no known processes which change the total lepton number. The charged leptons, along with their corresponding neutrinos, are given in Table 1.2.

Charged Lepton		Mass (MeV)	Neutrino	Mass (eV)
Electron	e	0.520 998 928(11)	ν_e	< 2
Muon	μ	105.658 371 5(35)	ν_μ	< 2
Tau	τ	1776.82(16)	ν_τ	< 2

Table 1.2: The charged leptons with their corresponding neutrinos and their masses [2].

Quarks

The quarks carry fractional electric charge. For example, the Up (u) quark carries $+2/3$ times the charge of the positron. Quarks carry another type of charge which we call *color charge*. The term "color" is actually just an analogy, and doesn't indicate color as we are accustomed to it in everyday life. A quark can be either red, green, or blue (RGB), and an antiquark could be anti-red, anti-green, or anti-blue ($\bar{\text{R}}\bar{\text{G}}\bar{\text{B}}$). The quarks with their charges and their masses are given in Table 1.3.

Quark		Charge	Mass (MeV)
Up	u	$+2/3$	1.8 to 3.0
Down	d	$-1/3$	3.3 to 4.2
Charm	c	$+2/3$	$1.275(25) \times 10^3$
Strange	s	$-1/3$	95(5)
Top	t	$+2/3$	$173.21(110) \times 10^3$
Bottom	b	$-1/3$	$4.66(3) \times 10^3$

Table 1.3: The quarks with their charges and masses [2].

Quarks are never found outside of bound states. That is, a lone quark has never been observed [1]. Bound states of quarks are called *hadrons*, and they come in two varieties: *mesons* and *baryons*. Mesons are composed of a quark and an antiquark, and baryons are composed of three quarks or three antiquarks. This is where the color analogy comes into play. We say that any particle found in nature must be colorless. A meson, made of a quark and antiquark, could have color charges of red and anti-red. The combination is white, so the meson is colorless. For baryons, with three quarks, you could have red, green, and blue, the combination of which is also white. So, the analogy of color neatly describes how hadrons are found in two and three-quark bound states [5].

Two familiar baryons are protons and neutrons. The quark content of a proton is uud, and ddu for a neutron. Protons are generally thought to be stable in nature. If a proton does decay, its mean lifetime is $> 10^{31}$ to 10^{33} years [2]. Outside of an atomic nucleus, the neutron has a mean lifetime 880.3(11) s, and it decays into a proton, electron, and an electron-type neutrino. This decay can occur since a neutron is slightly more massive than a proton with $m_n = 939.565\,379(32)$ MeV and $m_p = 938.272\,046(21)$ MeV [2].

Mesons are commonplace in hadron beam collisions, like those at the LHC. The lightest mesons are the pions. There are two charged pions, π^+ and π^- with a mass of 139.570 18(35) MeV, and their quark contents are $u\bar{d}$ and $\bar{u}d$, respectively. Their mean lifetime is $2.6033(5) \times 10^{-2}$ μs, and they decay to $\mu^{\pm}\nu_{\mu}$ more than 99% of the time [2]. There

is also a neutral pion, π^0, which has a mass of 134.9766(6) MeV, and a quark content of $\sqrt{\frac{1}{2}}\left(u\bar{u} - d\bar{d}\right)$. It decays much quicker than its charged counterparts, with a mean lifetime of $8.52(18) \times 10^{-11}$ μs, and it decays to $\gamma\gamma$ more than 98% of the time [2].

Forces

One of the more familiar forces is the electromagnetic force. Classically, the electromagnetic force is described by Maxwell's equations, where the electric and magnetic fields are treated as classical fields. In quantum field theory, forces are quantized and mediated by particles. In electromagnetism, the force is carried by the massless photon. The quantum field theory for electromagnetism is quantum electrodynamics (QED). The Lagrangian for QED that describes the interactions between fermions and photons is

$$\mathcal{L}_{QED} = \bar{\psi}\left(i\partial^\mu\gamma_\mu - m\right) - F_{\mu\nu}F^{\mu\nu} - iQeA_\mu\bar{\psi}\gamma^\mu\psi. \tag{1.10}$$

An important feature of this Lagrangian is that the substitution

$$\psi(x) \to e^{i\alpha(x)}\psi(x) \tag{1.11}$$

leaves the Lagrangian invariant. This is called a *local gauge transformation.* Because the Lagrangian is invariant under this transformation, we say it obeys a $U(1)$ gauge symmetry. Fermions are created and destroyed by the field ψ, and the spin-1 photons are created and destroyed by the field $\vec{A}$, and $F_{\mu\nu}$ is the electromagnetic field strength tensor: $F_{\mu\nu} = \partial_\mu A_\nu - \partial_\nu A_\mu$.

The weak force is responsible for the decays of atomic nuclei, as well as the decays of leptons like muons and taus. There are three vector bosons that mediate the weak force: the Z, W^+ and W^-. Unlike the photon, the Z and W bosons are massive (Table 1.1), and have a very short range on the order of 10^{-18} m. The Ws couple only to left-handed

fermions, which we arrange in $SU(2)$ doublets

$$\Psi_i = \begin{pmatrix} \nu_i \\ \ell_i^- \end{pmatrix}_L \quad \text{and} \quad \begin{pmatrix} u_i \\ d_i' \end{pmatrix}_L \tag{1.12}$$

where $d_i' \equiv \sum V_{ij} d_j$. V is the Cabibbo-Kobayashi-Maskawa mixing matrix for quarks [2]. The doublets carry a quantum number called *weak isospin*, which is $T = 1/2$. The third component of the isospin, T_3, has values of $+1/2$ for the upper portion of the doublet, and $-1/2$ for the lower portion. Right-handed fermions are singlets in $SU(2)$, and have a weak isospin of $T = 0$. The interaction Lagrangian for the Ws and fermions is

$$\mathcal{L}_W = -\frac{g}{2\sqrt{2}} \overline{\Psi} \gamma^\mu \left(1 - \gamma^5\right) \left(T^+ W_\mu^+ + T^- W_\mu^-\right) \Psi \tag{1.13}$$

where $T^\pm$ are the weak isospin raising and lowering operators. The Z boson couples to left and right-handed fermions via

$$\mathcal{L}_Z = -\frac{g}{\cos\theta_W} \overline{\psi} \gamma^\mu \left(g_V - g_A \gamma^5\right) \psi Z_\mu \tag{1.14}$$

The constants g_V and g_A represent the vector and axial couplings respectively, are are given by

$$g_V^i \equiv T_3(i) - 2Q_i \sin^2\theta_W \tag{1.15}$$

$$g_A^i \equiv T_3(i) \tag{1.16}$$

where T_3 is the weak isospin of the fermion, Q is the electric charge in units of e, and θ_W is the weak mixing angle where $\sin^2\theta_W \approx 0.23$. Muons and electrons have a weak isospin of $-1/2$ and a charge of 1, therefore they couple with the same strength to the Z. The total width of the Z is $\Gamma_Z = 2.4952(21)\,\text{GeV}$, and the partial width to charged leptons is $\Gamma_Z(\ell^+\ell^-) = 83.984(86)\,\text{MeV}$ [2].

Electroweak Unification and Symmetry Breaking

At sufficiently high energies, the masses of the weak bosons become negligible, and the weak force becomes indistinguishable from the electromagnetic force. Glashow, Weinberg, and Salam unified the electromagnetic and weak forces into a single Electroweak Theory which obeys $SU(2)_L \times U(1)_Y$ gauge symmetry [6, 7, 8]. The theory utilizes four vector fields: B_μ, and $W_\mu^{a=1,2,3}$. In order for these fields to obey the gauge symmetry, they must be massless. The photon is known to be massless, which leaves the $U(1)$ symmetry unbroken. The $W^\pm$ and Z, however, are not. Therefore the theory requires a mechanism to spontaneously break the $SU(2)_L$ symmetry and give masses to the weak vector bosons, while preserving the $U(1)$ symmetry.

In the Standard Model the Brout-Englert-Higgs Mechanism brings about electroweak symmetry breaking, which we refer to colloquially as the Higgs Mechanism [9, 10, 11]. A complex scalar $SU(2)_L$ doublet is added to the Lagrangian

$$\phi = \begin{pmatrix} \phi^+ \\ \phi^0 \end{pmatrix} \tag{1.17}$$

which obeys the following interaction potential

$$V(\phi) = \mu^2 \phi^\dagger \phi + \frac{\lambda^2}{2} \left(\phi^\dagger \phi\right)^2 . \tag{1.18}$$

where λ and μ are free parameters. This potential is invariant under $U(1)_Y$ for any value of λ and μ, preserving the symmetry as required.

By itself, this potential does not necessarily provide spontaneous symmetry breaking of $SU(2)_L$; it depends on the value of μ^2. If $\mu^2 \geq 0$, then the minimum of $\phi^\dagger \phi$ is 0. In this situation, the vacuum expectation value (VEV) of ϕ is 0, and the symmetry is unbroken. If $\mu^2 < 0$, then the minimum of $\phi^\dagger \phi$ becomes nonzero, as does its vacuum expectation value,

$$\left(\phi^\dagger \phi\right)_{min} = \frac{v^2}{2} \tag{1.19}$$

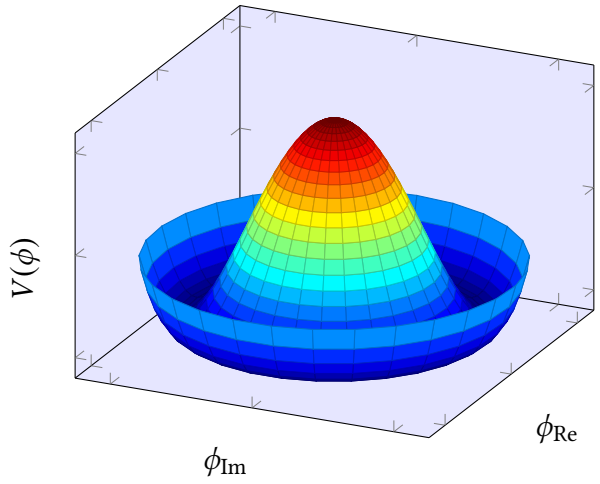

Figure 1.3: Qualitative plot of the Higgs potential, which is colloquially called the "Mexican hat" potential. The top of the "hat" corresponds to a VEV of zero, and the symmetry is not broken. The symmetry breaks spontaneously when the minimum of the field falls into the rim, and the VEV is no longer zero.

where $v = \sqrt{-\mu^2/\lambda^2}$. This is shown qualitatively in Figure 1.3. In the Standard Model this value is directly related to the masses of the weak vector bosons.

$$M_W = \frac{1}{2}gv \tag{1.20}$$

$$M_Z = \frac{1}{2}\sqrt{g^2 + g'^2}v \tag{1.21}$$

The photon appropriately remains massless.

The introduction of the ϕ field, and the subsequent spontaneous symmetry breaking, predict an additional massive scalar particle, H, with a mass of

$$M_H = \lambda v. \tag{1.22}$$

We refer to this particle as the Higgs boson. Because of the crucial role this particle plays in the Standard Model, searching for it has been a primary goal of particle physics since its prediction in the 1960's.

The Higgs couples directly to the weak vector boson via the following interaction

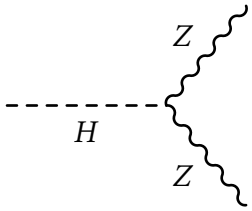

Figure 1.4: A single Higgs couples to two Z bosons with a vertex factor of $ig^{\mu\nu}\left(g^2+g'^2\right)v/2$.

Lagrangian

$$\mathcal{L}=\frac{(v+H)^2}{4}\left(g^2W_\mu^+W^{-\mu}+\frac{1}{2}\left(g^2+g'^2\right)Z_\mu Z^\mu\right). \tag{1.23}$$

In particular, the Higgs can decay to a pair of Z bosons as shown in Figure 1.4. Within the context of the model, the branching ratio of the Higgs to two Z bosons is dependent on the mass of the Higgs. For a Higgs with a mass of 125.0 GeV, the branching ratio of $H\rightarrow ZZ$ is 2.64×10^{-2} [2].

The Higgs can also couple to fermions. For electrons, the relevant portion of the Lagrangian would look like

$$\mathcal{L}=-\frac{Y_e}{\sqrt{2}}(v+H)\left(\bar{e}_Le_R+\bar{e}_Re_L\right) \tag{1.24}$$

where Y_e is the Yukawa coupling of the Higgs field to the electron. In this way, the Higgs field can also provide mass to the fermions. However, in order for this to work, you must have both right and left-handed varieties of the particle in question. Neutrinos have never been observed being produced in a right-handed configuration. In the absence of right-handed neutrinos, they cannot acquire mass through the Higgs Mechanism.

The Yukawa couplings provide a means for the Higgs to be produced in pp collisions at the LHC. The dominant Higgs production mode in pp collisions is $gg\rightarrow H$. Gluons do not have mass, therefore they cannot directly couple to the Higgs. Instead they couple indirectly through a quark loop shown in Figure 1.5.

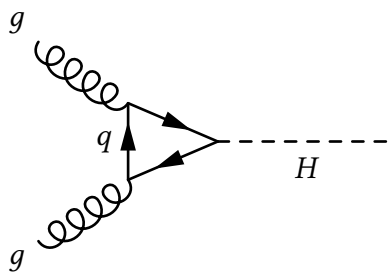

Figure 1.5: Two gluons from colliding protons form a quark loop which can produce a Higgs boson. Since the Higgs couples strongly to high-mass particles, the top quark is the dominant contribution in the loop. We call this process *gluon fusion*.

1.4 Spin and Parity of the Standard Model Higgs Boson

The Standard Model specifically predicts that the Higgs boson is a scalar particle. That is, it has a spin of 0 and even parity ($J^P = 0^+$). These properties are manifest in the kinematics of the final decay products of a Higgs particle.

A Higgs boson is capable of decaying directly to two Z bosons. In turn, the Z can decay to two charged leptons. So, one of the possible final states of a Higgs decay is to four charged leptons: $H \to ZZ \to 4\ell$ (Figure 1.6). This is sometimes called the "golden channel", since it has a very clean signature in a detector. The momenta of charged leptons, specifically muons and electrons, can be directly measured by a detector. Taus decay far too quickly to be measured directly, and neutrinos are nearly impossible to measure directly since they interact with matter so infrequently. Quarks immediately hadronize, creating a collimated spray of particles called *jets*, which are much more difficult to reconstruct than individual electrons and muons. As a result, the 4ℓ final state is very well suited for performing precision measurements of the properties of the Higgs.

When a Z decays, the decay products must have the same flavor, but opposite charge. If we consider only decays to light-leptons (muons and electrons), this restricts us

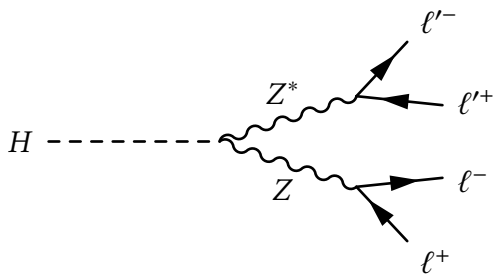

Figure 1.6: A Higgs can decay to two Z bosons, which can then decay to a total of four charged leptons. For a Higgs at 126 GeV, one of the Z bosons must necessarily be off-shell, since the Z mass is 91.2 GeV. The off-shell Z is denoted by Z^*.

to the following possible final states: 4μ, $4e$, and $2e2\mu$.

The kinematics of the 4ℓ final state of a Higgs decay can be fully characterized with five angles, $\vec{\Omega} = (\theta^*, \theta_1, \theta_2, \Phi, \Phi_1)$, and the invariant masses of the opposite-sign same-flavor lepton pairs, denoted m_{Z_1} and m_{Z_2} [12]. Thus, they can be utilized to determine the spin and parity of the Higgs. The angles are shown in Figure 1.7, and they describe the following:

θ^* The angle between Z_1's trajectory and the beam axis.

Φ_1 The angle between the Z_1 decay plane and the H decay plane.

$\theta_{1,2}$ The angle between the negatively-charged lepton trajectory and the trajectory of its parent Z.

Φ The angle between the decays planes of the two Zs.

A method for determining the spin and parity of the Higgs in the $ZZ \to 4\ell$ final state is described in *Inferring the Nature of the Boson* [13]. The method takes into account the fact that the Higgs is near 125 GeV in mass, so one of the Z bosons must be off-shell. It is also assumed that the discovered Higgs is not spin-1 and has positive charge conjugation, since it has been observed decaying to two photons.

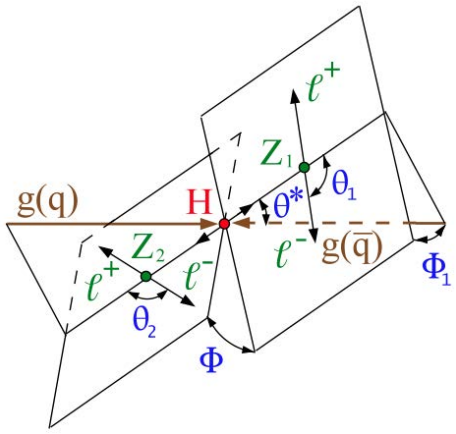

FIGURE 1.7: The five kinematic angles used to characterize the decay of a Higgs boson to a four-lepton final state.

The Higgs differential decay rate is decomposed into three uni-angular distributions that utilize three of the five angles: $\theta_{1,2}$ and ϕ.

$$\frac{1}{\Gamma_f}\frac{d^2\Gamma}{dq_2^2\, d\cos\theta_1} = \frac{1}{2} + T_2 P_2(\cos\theta_1) - T_1 \cos\theta_1 \tag{1.25}$$

$$\frac{1}{\Gamma_f}\frac{d^2\Gamma}{dq_2^2\, d\cos\theta_2} = \frac{1}{2} + T_2 P_2(\cos\theta_1) - T_1 \cos\theta_1 \tag{1.26}$$

$$\frac{2\pi}{\Gamma_f}\frac{d^2\Gamma}{dq_2^2\, d\phi} = 1 + U_2 \cos 2\phi + V_2 \sin 2\phi + U_1 \cos\phi \tag{1.27}$$

where ϕ is the same as Φ in Figure 1.7, and q_2^2 is the invariant mass of the off-shell Z. P_2 is a second-order Legendre polynomial. By determining the T, U, and V coefficients, the observed Higgs can be distinguished between the SM pure-scalar 0^+, a pseudoscalar 0^-, and spin-2 configurations 2^+ or 2^-.

1.5 Higgs Triplet and Neutrino Masses

It is well established experimentally that neutrinos do have non-zero mass. However, this is not accounted for in the Standard Model. Several models exist that can accommodate neutrino masses. One of them is a Higgs triplet, which is a Type II "seesaw" mechanism

[4]. This model extends the Standard Model particle spectrum with a scalar triplet, $\Phi = (\Phi^0, \Phi^+, \Phi^{++})$, that has $SU(2)_L \times U(1)_Y$ quantum numbers $\Phi \sim (3, 2)$.

The left-handed Higgs triplet field couples to leptons with the following Lagrangian

$$\mathcal{L} = i\bar{\ell}_{Li}\tau_2 Y_\Phi^{ij} (\tau \cdot \Phi) \ell_{Lj} + h.c. \tag{1.28}$$

where the τ's are Pauli matrices, Y_{ij} are the Yukawa couplings, and ℓ_L is an $SU(2)_L$ lepton doublet (Equation 1.12). This yields the following partial widths for the decay of the doubly charged portion of the triplet

$$\Gamma\left(\Phi^{\pm\pm} \to \ell_i^\pm \ell_j^\pm\right) = \begin{cases} \frac{1}{8\pi}|(Y_\Phi)_{ij}|^2 m_{\Phi^{\pm\pm}} & i = j \\ \frac{1}{4\pi}|(Y_\Phi)_{ij}|^2 m_{\Phi^{\pm\pm}} & i \neq j \end{cases} \tag{1.29}$$

An important feature of this model is that lepton flavor-violating decays are allowed. The neutrino mass matrix is directly related to the Yukawa couplings and the triplet vacuum expectation value (VEV): $(m_\nu)_{ij} = 2(Y_\Phi)_{ij}\, v_\Phi$. The individual neutrino masses are found by diagonalizing $(m_\nu)_{ij}$. Because the neutrino masses are so small, it is natural to assume that the VEV, v_Φ, would be small in order to avoid unnaturally small Yukawa couplings. Assuming a small VEV suppresses a possible decay of the doubly charged Higgs to WW, the width of which is proportional to v_Φ^2.

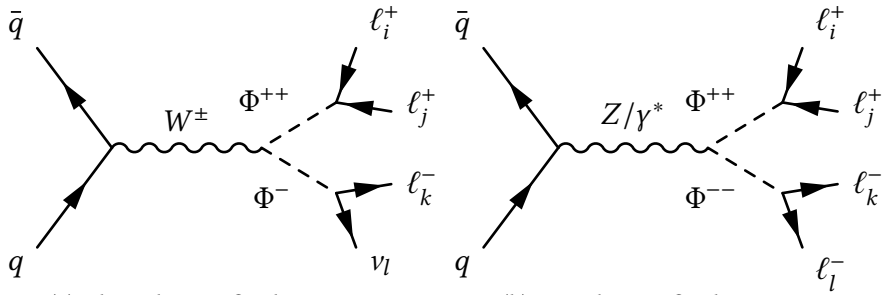

(a) Three-lepton final state (b) Four-lepton final state

Figure 1.8: Associated and pair production of a doubly charged Higgs, which produce 3ℓ and 4ℓ final states.

Should such a doubly charged Higgs be found, the branching ratios would be of principal interest. Measuring the branching fractions would give us access to neutrino parameters such as

- The masses: m_1, m_2, m_3
- Majorana Phases: α_1, α_2, or $\Delta\alpha = |\alpha_1 - \alpha_2|$
- CP-violating angle δ
- Higgs triplet VEV

In this way, LHC pp collisions can be utilized to explore neutrino physics [4].

The doubly charged Higgs can be produced either by associated production, or by Drell-Yan pair production (Figure 1.8). In the first case, a W decays to the doubly charged and singly-charged bosons in the triplet. The doubly charged Higgs decays to two same-sign charged leptons, and the singly charged Higgs decays to a charged lepton and a neutrino. So, the final state includes three charged leptons, which we call the 3ℓ final state. In the 4ℓ final state, a Z/γ^* decays to Φ^{++} and Φ^{--}, and each decays to two charged leptons.

The branching fractions are not fixed by the model, but different configurations of the branching fractions carry different implications, and are therefore of interest. Four "benchmark points" that target different neutrino mass hierarchies are (Table 1.4),

BP1 Tri-bi-maximal neutrino mixing (Equation 1.30) is assumed, no CP violation, normal neutrino mass ordering, and the lowest neutrino mass vanishing

BP2 Same as BP1, but with an inverted neutrino mass ordering

BP3 Same as BP1, but the lightest neutrino mass is assumed to be 0.2 eV, which is consistent with the cosmological limit for degenerate (or nearly degenerate) masses [14].

BP4 All BRs are assumed to be equal

Benchmark Point	ee	$e\mu$	$e\tau$	$\mu\mu$	$\mu\tau$	$\tau\tau$
BP1	0	0.01	0.01	0.30	0.38	0.30
BP2	0.5	0	0	0.125	0.25	0.125
BP3	0.34	0	0	0.33	0	0.33
BP4	1/6	1/6	1/6	1/6	1/6	1/6

Table 1.4: Branching fraction scenarios for the decays of $\Phi^{\pm\pm}$.

The tri-bi-maximal model of mixing predicts the following mixing angles

$$\sin^2\theta_{12} = \frac{1}{3} \qquad \sin^2\theta_{23} = \frac{1}{2} \qquad \sin^2\theta_{13} = 0 \tag{1.30}$$

which are consistent with measurements on the neutrino mixing angles, given in Equation 1.9 [4]. Tri-bi-maximal mixing predicts that the ν_2 mass eigenstate is maximally mixed among the three flavor eigenstates, and ν_3 is maximally mixed between ν_μ and ν_τ. This produces a neutrino mixing matrix (PMNS Matrix, Equation 1.8) of

$$\begin{array}{c} \\ \nu_e \\ \nu_\mu \\ \nu_\tau \end{array} \begin{array}{c} \begin{array}{ccc} \nu_1 & \nu_2 & \nu_3 \end{array} \\ \begin{pmatrix} 2/3 & 1/3 & 0 \\ 1/6 & 1/3 & 1/2 \\ 1/6 & 1/3 & 1/2 \end{pmatrix} \end{array} \tag{1.31}$$

where the individual elements have been squared.

CMS is capable of searching for the doubly charged Higgs in both Drell-Yan pair production and associated production modes. Utilizing both modes substantially increases the sensitivity to higher doubly charged Higgs mass hypotheses. Since the masses and the

branching ratios of the doubly charged Higgs are not determined by the model, searches must be performed over a range of mass hypotheses as well as different possible branching ratio configurations. There is no individual Standard Model particle that can decay to same-sign lepton pairs like the doubly charged Higgs. However, Standard Model ZZ production can produce two pairs of same-sign leptons, and is the dominant background to doubly charged Higgs pair production. CMS has performed a search utilizing 7 TeV LHC data, which is described in Chapter 2. The analysis presented in this thesis is the continuation of the previous CMS search utilizing the 8 TeV dataset, however we only focus on the pair production-mode.

2 Previous Results

2.1 Spin-Parity of the Higgs Boson

The most extensive measurements of the properties of the Higgs boson come from the CMS and ATLAS experiments at the LHC. Property measurements of the Higgs boson relied heavily on the $H \to ZZ \to 4\ell$ channel. Analyses performed in this channel utilize electrons and muons, which can be fully reconstructed and therefore perform well for precision measurements. Other channels involving jets and missing transverse energy have lower energy resolution. The 4ℓ channel also has the distinct advantage of having few backgrounds, the dominant of which is $gg/q\bar{q} \to ZZ$, which is a known and well-understood process. Spin-parity measurements have also been performed using $H \to WW$ and $H \to b\bar{b}$. The fact that the Higgs has been observed decaying to a pair of photons [15, 16] indicates that it cannot be spin-1.

Prior work on the Higgs boson focused on searching for it. Direct searches for the Higgs boson have been performed by the Large Electron-Positron (LEP) and Tevatron colliders, as well as the LHC. LEP, which ran from 1989 to 2000, set a lower bound on the Higgs mass of 114.4 GeV at the 95% confidence level [17], and the Tevatron excluded the mass range of 162 to 166 GeV [18]. The Higgs was finally discovered by the CMS and ATLAS collaborations in 2012 with a mass near 125 GeV [19]. In 2013, the Tevatron observed a local significance of 3.0 standard deviations at $m_H = 125$ GeV, consistent with

the LHC discovery [20]. The most recent measurement of the mass combines both CMS and ATLAS measurements to give $m_H = 125.09 \pm 0.21\ (\text{stat}) \pm 0.11\ (\text{syst})$ GeV [21].

CMS Spin-Parity Measurements in $H \to ZZ \to 4\ell$

The latest spin-parity measurements in the $H \to ZZ \to 4\ell$ channel performed by CMS utilized $5.1\,\text{fb}^{-1}$ of pp collision data at 7 TeV, and $19.7\,\text{fb}^{-1}$ at 8 TeV [22]. Earlier CMS spin-parity results are described in reference [23]. They compare the Standard Model pure-scalar hypothesis against several alternate spin-parity configurations with different production modes. These include pseudoscalar, spin-1, and spin-2 hypotheses with + and − parity, as well as hypotheses with modified couplings. Descriptions of the models are listed in Table 2.1. The spin-0 hypotheses are built using a general decay amplitude of a spin-0 particle to two vector bosons

$$
\begin{aligned}
A(H \to ZZ) &= v^{-1}\left(a_1 \cdot m_Z^2 \epsilon_1^* \epsilon_2^* + a_2 \cdot f_{\mu\nu}^{*(1)} f^{*(2),\mu\nu} + a_3 \cdot f_{\mu\nu}^{*(1)} \tilde{f}^{*(2),\mu\nu}\right) \qquad (2.1)\\
f^{(i),\mu\nu} &= \epsilon_i^\mu q_i^\nu - \epsilon_i^\nu q_i^\mu \\
\tilde{f}_{\mu\nu}^{(i)} &= 1/2 \epsilon_{\mu\nu\alpha\beta} f^{(i),\alpha\beta} = \epsilon_{\mu\nu\alpha\beta} \epsilon_i^\alpha q_i^\beta
\end{aligned}
$$

where v is the Higgs VEV, and $f^{(i),\mu\nu} = \epsilon_i^\mu q_i^\nu - \epsilon_i^\nu q_i^\mu$ is the field-strength tensor of a gauge boson with momentum q and polarization vector ϵ.

The CMS analysis constructs two discriminants, $\mathcal{D}_{J^P}$ and $\mathcal{D}_{bkg}$. The first discriminant separates the pure-scalar hypothesis from a given alternate spin-parity hypothesis, and the second discriminates signal from background. The discriminants are built using the full set of kinematic information available in the 4ℓ event. This includes the 4ℓ invariant mass, the masses of the two Z candidates, and five kinematic angles (see Figure 1.7). From this, they build a log-likelihood ratio test statistic to discriminate between the pure-scalar

J^P	Production	Description
0^+	Any	SM pure scalar (a_1 dominates)
0^-	Any	Pseudoscalar (a_3 dominates)
0_h^+	Any	Non-SM scalar with higher-dimension operators (a_2 dominates)
1^+	$q\bar{q}$, Any	Pseudovector
1^-	$q\bar{q}$, Any	Vector
2_m^+	gg, $q\bar{q}$, Any	Graviton-like with minimal couplings
2_b^+	gg	Graviton-like where SM fields propagate in the bulk of extra dimensions
2_h^+	gg	Tensor with higher-dimension operators
2_h^-	gg	Pseudotensor with higher-dimension operators

Table 2.1: The spin-parity hypotheses and production modes tested in the CMS spin-parity analysis [22], which follows references [12, 24, 25]. The a_i parameters are part of the general spin-0 decay amplitude described in Equation 2.1.

and alternate hypotheses,

$$q = -2 \ln \left[\frac{\mathcal{L}_{J^P}}{\mathcal{L}_{0^+}} \right] \tag{2.2}$$

where the likelihood function is constructed from a two-dimensional p.d.f. with the $\mathcal{D}_{J^P}$ and $\mathcal{D}_{bkg}$ discriminants: $\mathcal{L}_{J^P} \equiv \mathcal{L}_{J^P}\left(\mathcal{D}_{bkg},\ \mathcal{D}_{J^P}\right)$. The results are summarized in Table 2.2, and are shown graphically in Figure 2.1, and all are compatible with the expectation of the Standard Model. The pseudoscalar and spin-1 hypotheses are excluded at the 99% confidence level. All spin-2 hypotheses are excluded at the 95% confidence level or higher.

CMS Spin-Parity Measurements in $H \to WW$

CMS has also performed a spin-parity measurement in the WW channel with a leptonic final state [26]. This analysis utilizes data corresponding to $4.9\,\text{fb}^{-1}$ at 7 TeV and $19.4\,\text{fb}^{-1}$ at 8 TeV. Their analysis compared the Standard Model against a pseudoscalar and spin-2 hypotheses. The results are summarized in Table 2.3, and are consistent with Standard Model predictions.

J^P	J^P Production	Expected ($\mu = 1$)	Obs. 0^+	Obs. J^P	CL_s
0^-	Any	2.4σ (2.7σ)	-0.9σ	$+3.6\sigma$	0.09%
0_h^+	Any	1.7σ (1.9σ)	-0.0σ	$+1.8\sigma$	7.1%
1^-	$q\bar{q} \to X$	2.6σ (2.7σ)	-1.4σ	$+4.8\sigma$	0.001%
1^-	Any	2.6σ (2.6σ)	-1.7σ	$+4.9\sigma$	0.001%
1^+	$q\bar{q} \to X$	2.1σ (2.3σ)	-1.5σ	$+4.1\sigma$	0.03%
1^+	Any	2.0σ (2.1σ)	-1.9σ	$+4.5\sigma$	0.01%
2_m^+	$gg \to X$	1.7σ (1.8σ)	-0.8σ	$+2.6\sigma$	1.9%
2_m^+	$q\bar{q} \to X$	1.6σ (1.7σ)	-1.6σ	$+3.6\sigma$	0.03%
2_m^+	Any	1.5σ (1.5σ)	-1.3σ	$+3.0\sigma$	1.4%
2_b^+	$gg \to X$	1.6σ (1.8σ)	-1.2σ	$+3.1\sigma$	0.9%
2_h^+	$gg \to X$	3.7σ (4.0σ)	$+1.8\sigma$	$+1.9\sigma$	3.1%
2_h^-	$gg \to X$	4.0σ (4.5σ)	$+1.0\sigma$	$+3.0\sigma$	1.7%

Table 2.2: Results of the CMS spin-parity analysis in the $H \to ZZ \to 4\ell$ channel [22]. The expected separation is shown when the signal strength is calculated from data, and when it is fixed to 1. The observed values reflect the consistency with the 0^+ or J^P models where the signal strength is allowed to float.

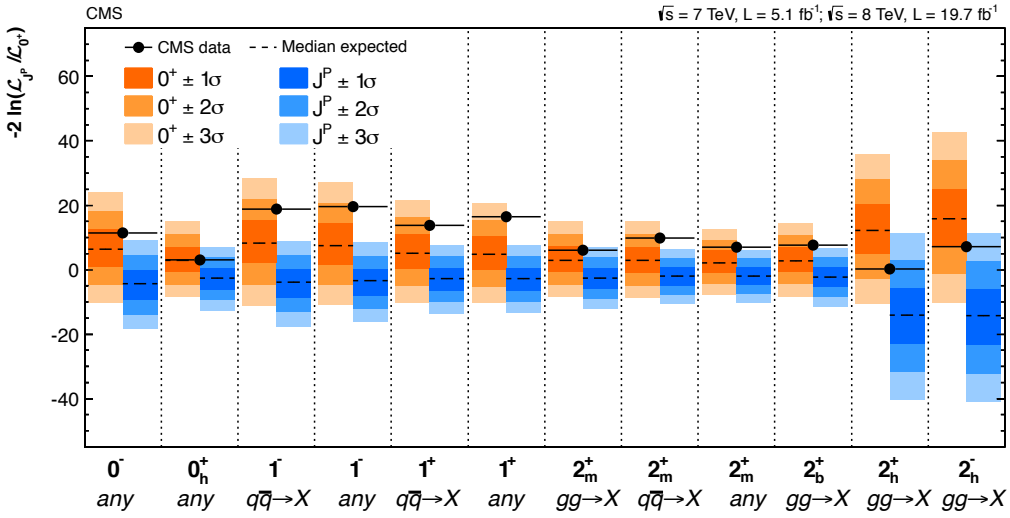

Figure 2.1: Results of the CMS $H \to ZZ \to 4\ell$ spin-parity analysis shown graphically [22]. The values of q are shown for the standard model in orange, and the alternate spin-parity hypothesis in blue. The expected distributions are created by generating MC toys assuming $m_H = 125.6$ GeV. The observed values of q is indicated with a black point.

J^P	J^P Production	Expected ($\mu = 1$)	Obs. 0^+	Obs. J^P	CL_s
2^+_m	$q\bar{q}$ (0%)	1.8σ (2.6σ)	$+0.6\sigma$	$+1.2\sigma$	16.3%
2^+_m	$q\bar{q}$ (50%)	2.3σ (3.2σ)	$+0.2\sigma$	$+2.1\sigma$	3.3%
2^+_m	$q\bar{q}$ (100%)	2.9σ (3.9σ)	-0.2σ	$+3.1\sigma$	0.2%
0^-	Any	0.8σ (1.1σ)	-0.5σ	$+1.2\sigma$	34.7%

Table 2.3: Results of the CMS spin-parity analysis in the $H \to WW$ channel with leptonic final states [26]. The spin-2 production mode is assumed to be gg and $q\bar{q}$, with the given fraction of $q\bar{q}$ contribution.

ATLAS Spin-Parity Results

The ATLAS spin-parity results utilize data corresponding to 4.6 fb^{-1} at 7 TeV and 20.7 fb^{-1} at 8 TeV [27, 16]. They use a similar strategy to CMS, which is to test the Standard Model hypothesis against alternate spin-parity configurations, and the two hypotheses are separated utilizing a log-likelihood ratio test statistic. They combine results from $H \to \gamma\gamma$, $H \to ZZ \to 4\ell$, and $H \to WW \to \ell\nu\ell\nu$ channels. Only the $ZZ \to 4\ell$ channel uses the 7 TeV dataset. The ATLAS results, summarized in Table 2.4, also show consistency with Standard Model expectations.

J^P	J^P Production	Exp. $P(0^+)$ (0^- assumed)	Exp. $P(J^P)$ (J^P assumed)	Obs. 0^+	Obs. J^P	CL_s
0^-	Any	3.0σ	2.7σ	$+0.5\sigma$	$+2.2\sigma$	2.2%
1^+	Any	2.8σ	3.3σ	-0.3σ	$+3.7\sigma$	0.03%
1^-	Any	3.0σ	2.7σ	$+0.4\sigma$	$+2.9\sigma$	0.27%
2^+_m	$q\bar{q}$(0%)	2.9σ	3.3σ	-0.3σ	$+3.6\sigma$	0.042%
2^+_m	$q\bar{q}$(25%)	2.5σ	2.9σ	-0.8σ	$+3.7\sigma$	0.046%
2^+_m	$q\bar{q}$(50%)	2.2σ	2.8σ	-1.0σ	$+3.8\sigma$	0.053%
2^+_m	$q\bar{q}$(75%)	2.3σ	3.1σ	-0.9σ	$+4.0\sigma$	0.017%
2^+_m	$q\bar{q}$(100%)	2.7σ	3.8σ	-0.9σ	$+4.7\sigma$	0.001%

Table 2.4: Combined ATLAS spin-parity results [27, 16]. The expected separation is given for the median value of q for 0^+ given the J^P distribution, and vice versa. The p-values are quoted as standard deviations, and the CL_s values are quoted as percentages to allow easier comparison with CMS results.

Tevatron Spin-Parity Results

The Tevatron performed a spin-parity analysis of the associated production of a Higgs decaying to a pair of bottom quarks: $WH \to \ell\nu b\bar{b}$, $ZH \to \ell^+\ell^- b\bar{b}$, and $WH + ZH \to \not{E}_T b\bar{b}$ [28]. The analysis combines results from the D0 and CDF experiments, which utilized about $10\,\text{fb}^{-1}$ of 1.96 TeV proton-antiproton collisions. They test the Standard Model hypothesis against a pseudoscalar (0^-) and spin-2 (2^+) hypotheses. The analysis relies on the fact that the kinematics of Higgs associated production differs depending on its spin-parity configuration. They exclude the 0^+ and 2^+ hypotheses with significances of 5.0σ and 4.9σ, respectively.

2.2 Search for a Doubly Charged Higgs

The earliest limits placed on the mass of the doubly charged Higgs utilized data from the PEP and PETRA e^+e^- storage rings at SLAC and DESY, and were based on how $\Phi^{\pm\pm}$ contributes to Bhabha scattering [29]. They exclude masses at 90% CL from 14.0 to 21.8 GeV, depending on the branching ratio hypothesis. The results are summarized in Table 2.5.

ee	$\mu\mu$	$\tau\tau$	$M(\Phi^{\pm\pm})$ Limits (GeV)
1	0	0	21.5
0	1	0	21.8
0	0	1	14.0
1/3	1/3	1/3	20.9

Table 2.5: Upper exclusion limits on the mass of $\Phi^{\pm\pm}$ with data from PEP and PETRA [29]. They are given for different branching ratio hypotheses for the doubly charged Higgs. The limits are given at the 90% confidence level.

The first direct search for a doubly charged Higgs was with the MARK II detector at SLAC, which utilized $19.7\,\text{nb}^{-1}$ of e^+e^- collisions at $\sqrt{s} \approx 90\,\text{GeV}$ [30]. In particular, they looked for pair-production of $\Phi^{++}\Phi^{--}$ from the decay of a Z, however they only

considered decays to same-flavor lepton pairs. Associated production of a doubly charged Higgs is forbidden at e^+e^- colliders because it would result in a charged final state. They found no doubly-charged Higgs candidates from 528 Z decays, and they excluded the mass range of 6.5 to 36.5 GeV at the 95% confidence level.

Doubly Charged Higgs Searches at LEP and the Tevatron

The searches performed by experiments at the LEP collider also searched for pair production of a doubly charged Higgs, and they were expanded to include lepton flavor violating decays. The analyses used 614 pb^{-1} of LEP e^+e^- collisions at $\sqrt{s}$ = 189 to 209 GeV to the OPAL, DELPHI, and L3 experiments. The OPAL and L3 experiments covered all final states: ee, $e\mu$, $e\tau$, $\mu\mu$, $\mu\tau$, and $\tau\tau$ [31, 32]. The DELPHI experiment focused on τ final states only, for the reason that many models expected the $\tau\tau$ coupling to be the strongest [33]. The mass limits are summarized in Table 2.6.

Searches were also performed at the Tevatron, with $p\bar{p}$ collisions at $\sqrt{s}$ = 1.96 TeV. The CDF experiment made two separate publications. Their electron and muon final states were published with 240 pb^{-1} [34], and their tau final states were published on 350 pb^{-1} [35]. D0 published results on the double-muon final state only with 1.1 fb^{-1} [36]. The results from both experiments are summarized in Table 2.6. Neither LEP nor the Tevatron observed a signal.

Doubly Charged Higgs Searches at the LHC

The strongest limits on the doubly charged Higgs mass are set by the CMS and ATLAS experiments at the LHC. The current CMS analysis used the 7 TeV dataset of 4.9 fb^{-1}, and covered all final states from pair-production as well as associated production. Specifically, they searched for a “left-handed” doubly charged Higgs boson [37]. Because of the rela-

Experiment	ee	$\mu\mu$	$\tau\tau$	$e\mu$	$e\tau$	$\mu\tau$
LEP						
OPAL	99.9	100.1	98.5	100.0	98.7	99.3
L3	100.1	99.1	97.6	99.7	95.5	93.8
DELPHI			97.3			
Tevatron						
CDF	133	113		115	114	112
D0		127				

Table 2.6: The mass limits for the doubly charged Higgs are given in GeV at the 95% confidence level [31, 32, 33, 34, 35, 36]. OPAL, CDF and D0 performed separate analyses for "left" and "right-handed" doubly charged Higgs bosons for some final states. The lower limit between the two is given. The doubly charged Higgs was assumed to decay 100% to each final state.

tionship between the doubly charged Higgs's branching ratios and neutrino parameters, CMS also examined different configurations of branching ratios. These are defined and discussed in section 1.5, and Table 1.4. The CMS limits are summarized in Table 2.7.

ATLAS performed the search using the 7 and 8 TeV datasets separately. The 7 TeV results utilized 4.7 fb^{-1}, and covered muon and electron final states [38]. The 8 TeV results utilized 20.3 fb^{-1} [39], which also covered electron and muon final states only. In addition to setting mass limits, the 8 TeV analysis also computed upper limits on the cross section for a hypothetical mass of the doubly charged Higgs. The ATLAS mass limits are summarized in Table 2.7.

The search for a doubly charged Higgs boson presented in this thesis continues the 7 TeV search performed by CMS. The 8 TeV dataset of 19.7 fb^{-1} is used, and the strategy closely follows that of the 7 TeV CMS analysis. As seen in the ATLAS results, moving from the 7 TeV dataset of 4.7 fb^{-1} to the 8 TeV dataset of 20.3 fb^{-1} extends the sensitivity of the search to higher masses, and similar improvements are expected when including the 8 TeV dataset with CMS.

Experiment	ee	$\mu\mu$	$\tau\tau$	$e\mu$	$e\tau$	$\mu\tau$	BP1	BP2	BP3	BP4
CMS (7 TeV, H_L^{++})	382	395	169	391	293	300	333	359	355	353
ATLAS (7 TeV, H_L^{++})	409	398		375						
ATLAS (7 TeV, H_R^{++})	322	306		310						
ATLAS (8 TeV, H_L^{++})	551	516		468						
ATLAS (8 TeV, H_R^{++})	374	438		402						

Table 2.7: The LHC mass limits for the doubly charged Higgs are given in GeV at the 95% confidence level. CMS performed searches with different branching ratio configurations in addition to the 100% BR cases [37]. These are denoted as BP1 to BP4, and are defined in Table 1.4. ATLAS performed searches for "left" and "right-handed" doubly charged Higgs bosons separately, and limits for both are shown [38, 39].

3 The Compact Muon Solenoid

The Compact Muon Solenoid (CMS) detector is one of two general-purpose detectors at the Large Hadron Collider; the other is ATLAS. One of the primary goals of the CMS and ATLAS experiments was to search for the Higgs boson. Other physics goals include searches for supersymmetry and other signatures of physics beyond the Standard Model. The major performance goals of the CMS detector are

- Good identification and momentum resolution of muons over a wide range of momenta and solid angles, as well as unambiguous charge measurement of muons with $p_T < 1\,\text{TeV}$
- Good identification and momentum resolution of charged particles in the inner tracker, as well as good resolution of secondary vertices
- A calorimeter with sufficient resolution and granularity to measure di-photon and di-electron invariant mass with a resolution of $\approx 1\%$ at 100 GeV, and to efficiently measure photon and electron isolation at high luminosity
- A hermetic calorimeter to provide good resolution of missing transverse energy

To accomplish these goals, CMS features an inner tracker, electromagnetic and hadronic calorimeters within a large-bore superconducting solenoid, a muon spectrometer, and

low and high-level triggers [40]. These systems, as well as the Large Hadron Collider, are discussed in subsequent sections.

3.1 The Large Hadron Collider

The Large Hadron Collider (LHC) is a proton synchrotron particle accelerator at CERN, located near Geneva, Switzerland. It was originally designed to collide two proton beams at a center of mass energy of $\sqrt{s} = 14.0\,\text{TeV}$. The accelerator is built within the 26.7 km tunnel originally used for the LEP experiment, which is located 45 to 170 m underground on a 1.4% incline [41]. The collider delivered pp collisions for data-taking from 2010 through 2012. The first run spanned 2010 to 2011, and collided protons at a center of mass energy of $\sqrt{s} = 7\,\text{TeV}$, and the second run in 2012 collided beams at $\sqrt{s} = 8\,\text{TeV}$. The LHC is the highest-energy collider in the world, surpassing Fermilab's Tevatron, which collided proton and anti-proton beams at $\sqrt{s} = 1.96\,\text{TeV}$ [2]. The LHC shut off for "Long Shutdown 1" (LS1) in early 2013, which lasted for two years. During this time-period, the LHC and the detectors prepared for running at 13 TeV and higher luminosities.

The LHC has four main experiments located at various points along the ring. The two general-purpose experiments, CMS and ATLAS, are located at Points 5 and 1 on the LHC ring, respectively (Figure 3.1). ALICE and LHCb are located at Points 2 and 8. ALICE is a heavy-ion experiment, and LHCb is a specialized b-physics experiment.

The LHC employs two beam-pipes with counter-rotating proton beams. For 14 TeV beams, 8.33 T magnetic fields are required to steer the protons around the ring. These fields are provided by 1232 dipole magnets made of Niobium-Titanium (NbTi) superconductors, which must be cooled to 2 K with superfluid helium. At 14 TeV beam energy, the dipoles carry 11 850 A of current [41].

During the $\sqrt{s} = 8\,\text{TeV}$ run period, the LHC delivered $23.3\,\text{fb}^{-1}$ of pp collisions

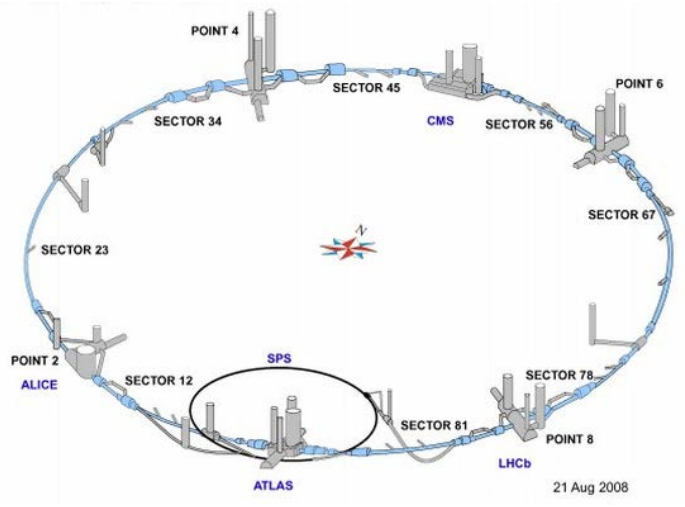

FIGURE 3.1: The layout of the LHC ring, with the experiments and access-points indicated. ATLAS, at Point 1, is located at the main CERN campus in Meyrin, Switzerland. CMS is located at Point 5, near Cessy, France.

and ran at an instantaneous luminosity of $\mathcal{L} = 7.7 \times 10^{33}\,\mathrm{cm^2 s^{-1}}$ (Figure 3.2). The proton beams are not continuous, and are grouped into discrete bunches of protons. During Run I, the LHC ran 1380 bunches per ring with 16×10^{10} protons per bunch [2]. On June 3, 2015, the LHC began delivering pp collisions at $\sqrt{s} = 13\,\mathrm{TeV}$ for data-taking.

3.2 Geometry

CMS is a cylindrical detector that is 15.0 m in diameter, 28.7 m long, and weighs 14 000 metric tons. The detector is laid out like an onion, with several layers of subdetectors. A particle produced in the beam-pipe at the center of the detector will encounter the subdetectors in the following order: tracker, electromagnetic calorimeter (ECAL), hadronic calorimeter (HCAL), superconducting solenoid, and muon system with the magnetic return yoke. The hadronic-forward (HF) calorimeter sits outside the endcaps very close to the beam-pipe (Figure 3.2).

CMS uses a right-handed coordinate system, with the y-axis pointing upwards,

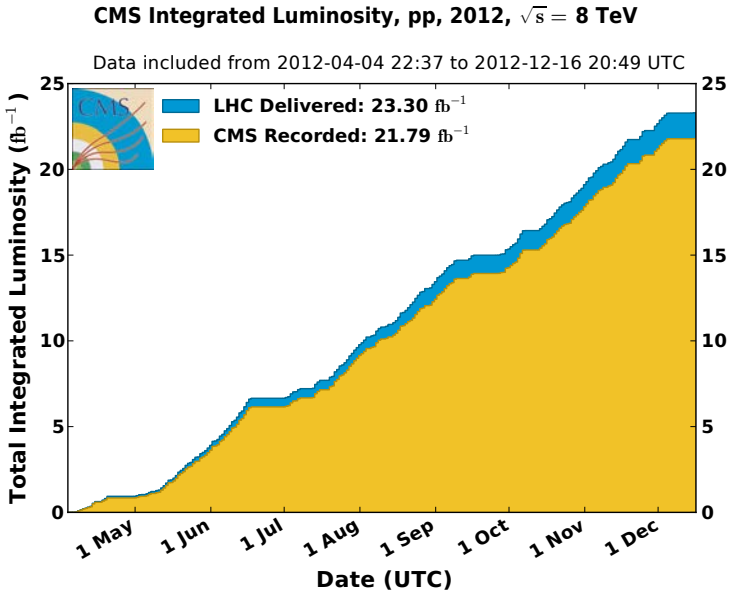

FIGURE 3.2: The integrated luminosity delivered by the LHC and recorded by CMS in 2012. This corresponds to *pp* collisions at a center of mass energy of 8 TeV.

and the x-axis pointing towards the center of the LHC ring. The azimuthal angle, ϕ, is measured from the x-axis in the x-y plane. The polar angle, θ, is measured from the z axis. In practice, we use a Lorentz-invariant quantity called *pseudorapidity*.

$$\eta = -\ln \tan\left(\frac{\theta}{2}\right) \tag{3.1}$$

An important property of η is that the particle occupancy per unit η is constant across the detector. η is 0 along the y-axis, infinity along the z-axis, and 0.88 at $\theta = 45°$.

In addition to η and ϕ, the detector measures the transverse momentum of a particle (p_T), which is the component of a particle's momentum in the x-y plane. In the high-energy limit, a particle's Cartesian three-momentum is

$$(p_x,\ p_y,\ p_z) = (p_T \cos\phi,\ p_T \sin\phi,\ p_T \sinh\eta) \tag{3.2}$$

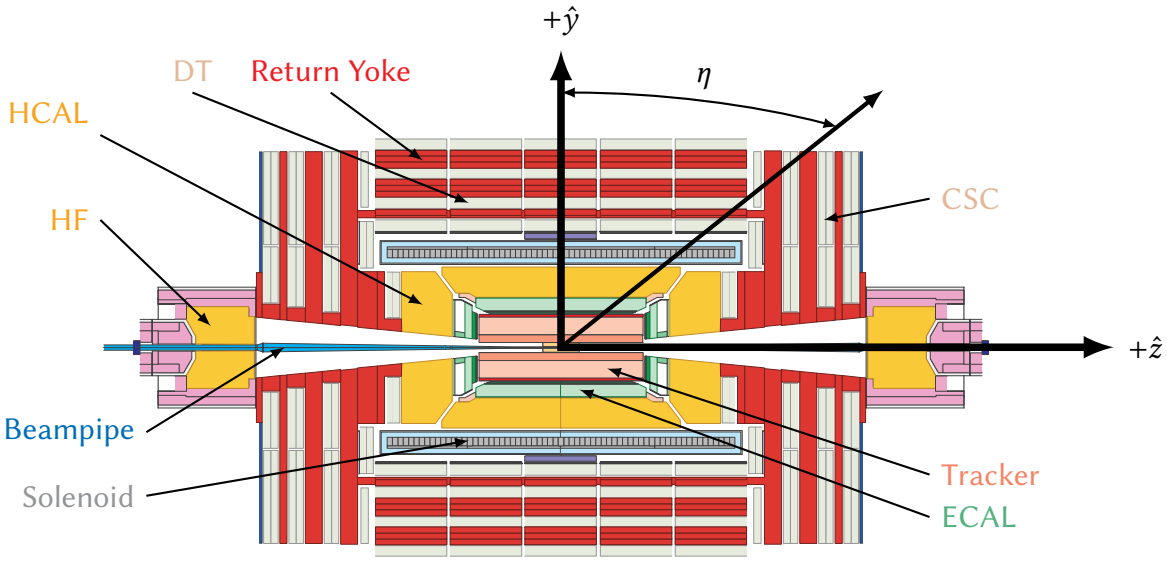

Figure 3.3: This is a longitudinal cross section of the CMS detector, showing the x and y axes, η, and the subdetectors.

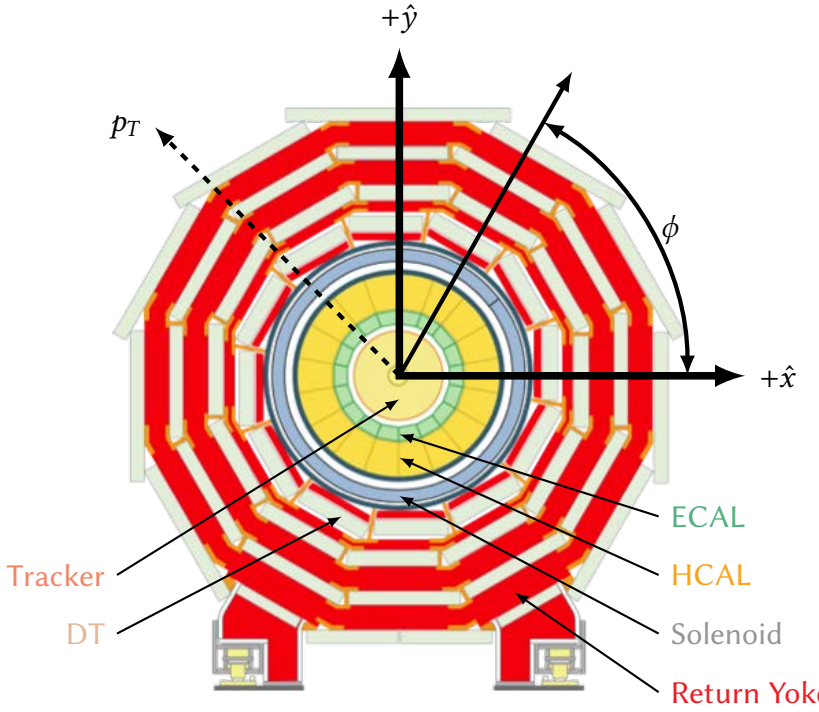

Figure 3.4: This is a transverse cross section of the CMS detector, showing the x and y axes, ϕ, p_T, and subdetectors.

3.3 Magnet

Since the trajectories of charged particles bend in the presence of a magnetic field, we can use a uniform magnetic field, B, to measure the p_T of charged particles,

$$p_T = qrB \tag{3.3}$$

where q is the charge of the particle, and r is its radius of curvature. The CMS magnetic field is produced with a large-bore superconducting solenoid, which is one of the detector's distinguishing features.

The solenoid provides a uniform 3.8 T magnetic field inside its bore, and is made of superconducting NbTi, which is kept at a temperature of 4.6 K. The solenoid is 12.5 m long, and has a bore diameter of 6 m. The magnet's large size allows the tracker and both calorimeters to be housed inside the solenoid, which has never been done before in a high-energy physics experiment. This reduces the energy loss of particles before they reach the calorimeters where their energies can be measured.

Outside of the solenoid is the iron return yoke. The yoke's purpose is to contain the return flux of the solenoid, and to provide a uniform 2 T field inside the muon system for measuring the momenta of muons. The field in the return yoke is limited to 2 T since iron saturates at that field strength.

3.4 Tracker

The tracker is the subdetector located closest to the beam-pipe, and is designed to measure the trajectories of charged particles. The entire tracking system is 5.8 m in length and 2.5 m in diameter, with an acceptance of $|\eta| < 2.5$. The tracker provides precise and efficient reconstruction of the trajectories of charged particles with $p_T > 1\,\text{GeV}$, and precise measurement of secondary vertices and impact parameters. Additionally, it must

operate in a high-radiation environment for the 10-year expected lifetime of the device. The entire tracker assembly consists of 1440 pixel and 15 148 silicon strip modules, which have a combined surface area of 200 m^2 [40].

The tracker system relies on silicon semiconductors for detection of charged particles. When a charged particle passes through the semiconductor, it releases an electron and a corresponding positive "hole" in the material. A high voltage is applied to the semiconductor, which gathers the released charges and registers the resulting electric pulse as a "hit". The tracker is segmented into two main components: the pixel detector, and silicon strip detector.

The pixel detector is the portion of the tracker nearest the interaction point, and it measures secondary vertices and impact parameters. It is composed of three barrel layers with radii of 4.4, 7.3, and 10.2 cm and two endcap disks (Figure 3.5(b)). The pixel size is $100 \times 150\,\mu m^2$, and 66 million of them cover roughly a $1\,m^2$ area. These provide a spatial resolution of 15-20 μm.

The silicon strip detector is segmented into two inner and outer sections. The tracker inner barrel (TIB) is composed of four layers covering radii 20 to 116 cm, and three endcap disks (TID) (Figure 3.5(a)). The tracker outer barrel (TOB) consist of 6 layers that extend out to a radius of 116 cm, with 9 outer disks (TOD). The silicon strips are 10 cm long, with pitches ranging from 80 to 184 μm.

Particle trajectories are formed by "connecting the dots" between the hits left in the tracker layers. By fitting a helix to a trail of tracker hits, one can determine the radius of curvature of a charged particle, and equivalently, its transverse momentum. For a 100 GeV charged particle, the tracker provides a p_T resolution of 1 to 2%. Additionally, it has an impact parameter resolution of $\approx 15\,\mu m$.

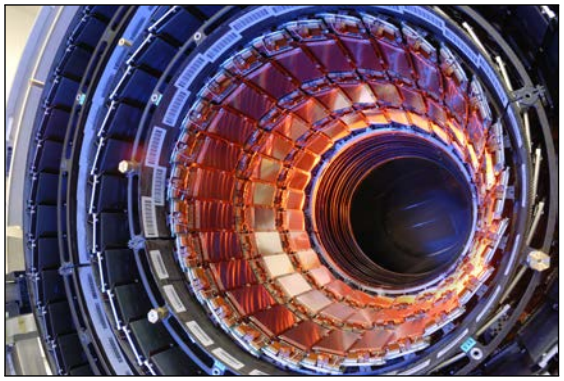

(a) Tracker Inner Barrel

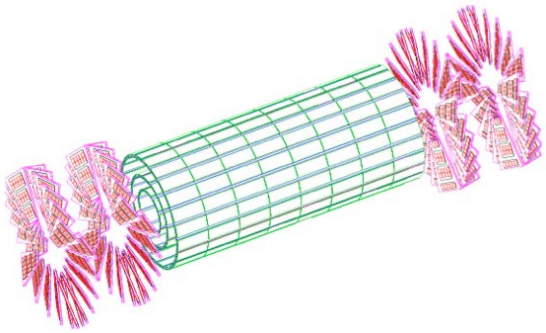

(b) Pixel Detector

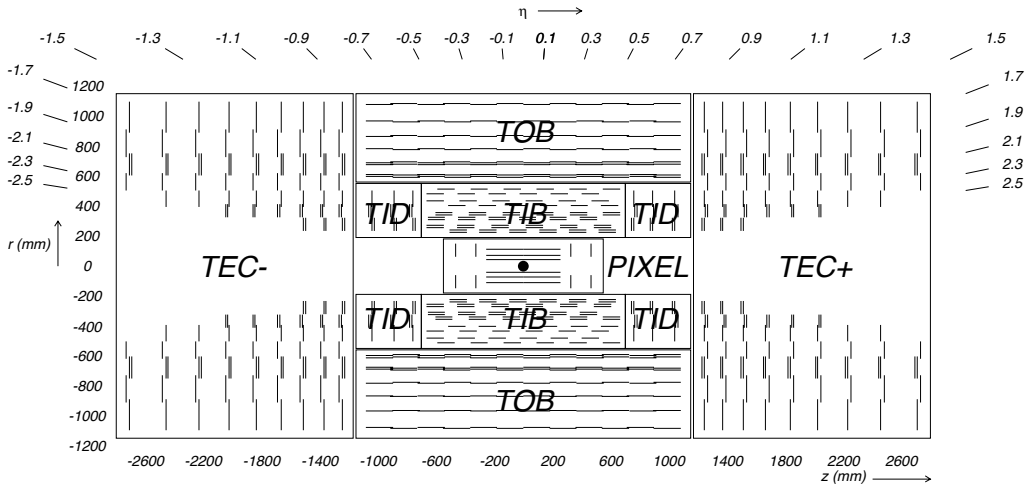

(c) Tracker Layout

Figure 3.5: A photograph of the CMS Tracker Inner Barrel (TIB) is shown on the left. On the right is a diagram of the pixel detector, showing the two endcap disks and three barrel layers. The bottom diagrams shows the entire layout of the tracker assembly, including the silicon strip detector and pixel detector sections.

3.5 Electromagnetic Calorimeter

The electromagnetic calorimeter (ECAL) is designed to measure the energies of particles that interact via the electromagnetic force: primarily photons and electrons. One of the driving goals behind the design of ECAL was to detect a di-photon event for the $H \to \gamma\gamma$ analysis. High-Z materials are effective for capturing the energy of high-energy photons. To that end, ECAL employs optically transparent lead-tungstate ($PbWO_4$) crystals. These

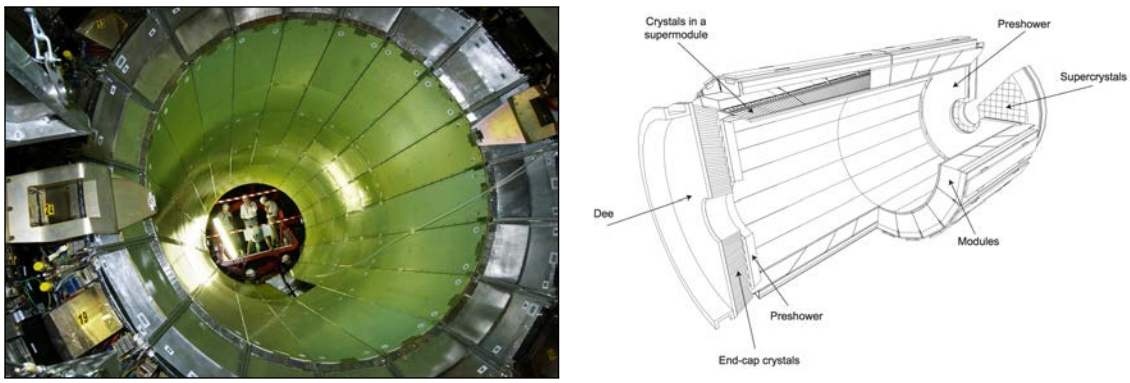

(a) ECAL Photograph (b) ECAL Schematic

Figure 3.6: A photograph of ECAL is shown on the left. A schematic of ECAL is on the right, which shows the placement of the lead tungstate crystals, and the overall layout of the endcap, barrel, and preshower.

are high density ($8.28\,\mathrm{g/cm^3}$), have a short radiation length ($X_0 = 0.89\,\mathrm{cm}$), and a small Molière radius (2.2 cm). This allows for a compact design of the calorimeter, enabling it to be placed inside the solenoid.

The ECAL barrel covers $|\eta| < 1.479$. It is composed of 61 200 crystals, which are arranged quasi-projectively. An individual crystal covers an area 0.0174×0.0174 in η-ϕ space. The barrel crystals are 230 mm long, which corresponds to $25.8X_0$. A radiation length, X_0, is the length scale for characterizing electromagnetic showers in matter. It corresponds to 1) the mean distance an electron travels before its energy is reduced to $1/e$ of its original energy, and 2) $7/9$ of the mean free path of a photon before it pair produces. For every MeV of captured energy, the crystals produce roughly 4.5 blue-green scintillation photons. The scintillation light is measured using avalanche photodiodes (APDs). As a photon enters the device, it releases an electron-hole pair within the semiconductor material. A high electric field in the device imparts enough energy in the charge carriers to produce additional electron-hole pairs via impact ionization. These, in turn, may create additional pairs, forming an avalanche. This produces a current that can be read out by an external circuit.

The ECAL endcap covers $1.479 < |\eta| < 3$, and is composed of 7324 crystals. The endcap crystals are $24.7X_0$ long, and their scintillation light is read out by vacuum phototriodes (VPTs). VPTs are basically photomultipliers with a single gain stage, and they are used in the endcaps because they receive much more radiation than the barrel.

Groups of ECAL crystals are formed into clusters and superclusters. These, in turn, are used alongside tracking information to produce particle candidates: photons, electrons, etc. The energy resolution of ECAL is

$$\left(\frac{\sigma(E)}{E}\right)^2 = \left(\frac{2.8\%}{\sqrt{E}}\right)^2 + \left(\frac{0.12}{E}\right)^2 + (0.30\%)^2 \tag{3.4}$$

where E is given in GeV. The first term is stochastic. It arises from shower fluctuations and from scintillation photon statistics. The second term is the result of noise from the electronics and pile-up. The third term is a constant, arising from detector non-uniformity, calibration uncertainties, and energy leakage in the crystals.

3.6 Hadronic Calorimeter

The hadronic calorimeter (HCAL) encloses the tracker and the electromagnetic calorimeter, and is designed to measure the energies of particles that interact via the strong force. An important use of HCAL is measuring the energies of neutral hadrons, as they cannot be measured with the tracker, and do not interact strongly via the electromagnetic force. The calorimeter must also be hermetic in order to provide a good measurement of missing transverse energy, $\not{E}_T$, which is necessary for inferring the presence of neutrinos. HCAL is a sampling calorimeter, and is composed of alternating layers of brass absorber and plastic scintillator. Brass is not ferromagnetic, which is important since it operates in a 3.8 T magnetic field. The detector itself is divided into three main components: barrel (HB), endcap (HE), and forward calorimeter (HF). HCAL as a whole provides coverage of $|\eta| < 5$.

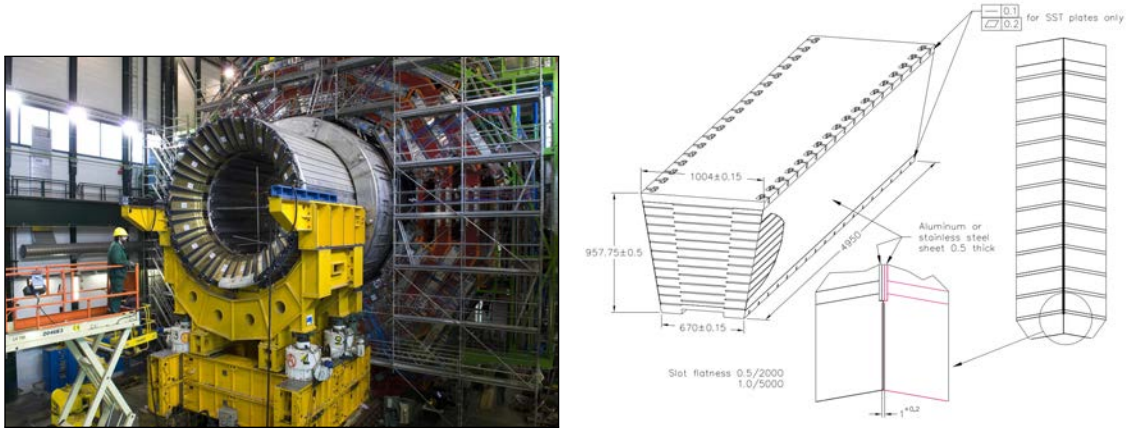

(a) HCAL Photograph (b) HCAL Wedge Schematic

FIGURE 3.7: A photograph of HCAL is shown on the left, which shows the barrel section situated inside of the solenoid cryostat. A schematic of an HCAL wedge is shown on the right, which shows the alternating layers of brass absorber and scintillator tiles.

The HCAL barrel (HB) covers $|\eta| < 1.3$. HB employs 70 000 scintillating tiles arranged in 16 η sectors with a segmentation of $\Delta\eta \times \Delta\phi = 0.087 \times 0.087$. These are longitudinally interleaved with two steel and 14 brass plates of absorber material. This provides 5.82 interaction lengths (λ_I) at $|\eta| = 0$, and $10.6\lambda_I$ at $|\eta| = 1.3$. An interaction length corresponds to the mean free path of a hadron before undergoing a hadronic interaction.

The HCAL endcaps (HE) cover $1.3 < |\eta| < 3$, which corresponds to 13.2% of the total solid angle. HE is composed of 20 916 scintillating tiles, which provide a total of 10 interaction lengths (including the contribution from ECAL). The tile segmentation is $\Delta\eta \times \Delta\phi = 0.087 \times 0.087$ for $|\eta| < 1.6$, and 0.17×0.17 for $|\eta| \geq 1.6$.

The forward hadronic calorimeter (HF), sits about 11.2 m from the interaction point very close to the beam-pipe, and experiences extremely high levels of radiation (see Figure 3.2). It is expected to receive 760 GeV of energy per pp interaction, as opposed to an average of 100 GeV for the rest of the detector. It extends the coverage of HCAL out to $|\eta| < 5$. HF is a Cherenkov detector, which uses quartz fibers instead of plastic scintillator as the active medium, and steel absorber instead of brass. It has a segmentation

of $\Delta\eta \times \Delta\phi = 0.175 \times 0.175$.

The barrel and endcap portions of HCAL provide an energy resolution of

$$\left(\frac{\sigma(E)}{E}\right)^2 = \left(\frac{90\%}{\sqrt{E}}\right)^2 + (4.5\%)^2 \tag{3.5}$$

and HF has an energy resolution of

$$\left(\frac{\sigma(E)}{E}\right)^2 = \left(\frac{172\%}{\sqrt{E}}\right)^2 + (9.0\%)^2 . \tag{3.6}$$

The first term is stochastic resulting from shower fluctuations and scintillation photon statistics. The constant term is from non-uniformity and calibration uncertainties.

3.7 Muon System

Muons are critically important for $H \to ZZ^* \to 4\ell$, as they are relatively easy to detect, and suffer from less radiative loss than electrons, making them well suited for precision studies. The CMS muon system has three main goals: identification of muons, momentum measurement, and triggering. The muon chambers are situated outside of the solenoid, and interleaved with the iron return yoke. The area is immersed in a 2 T magnetic field, which provides a lever arm for bending the paths of muons, making it possible to measure their momenta. All of the inner detectors, and the solenoid itself, serve as a hadron absorber. Including the muon system, this accounts for upwards of $16\lambda_I$, which makes punch-through negligible. Punch-through occurs when a charged hadron makes it into the muon system and fakes a muon. Three technologies are used in the muon system: drift tubes (DTs), cathode strip chambers (CSCs), and resistive plate chambers (RPCs). The layout of the CSCs, DTs, and RPCs within the CMS detector are shown in Figure 3.8.

The drift tubes are used in the barrel section which covers $|\eta| < 1.2$. The DTs are arranged into four stations, forming concentric circles around the beam-pipe. The drift

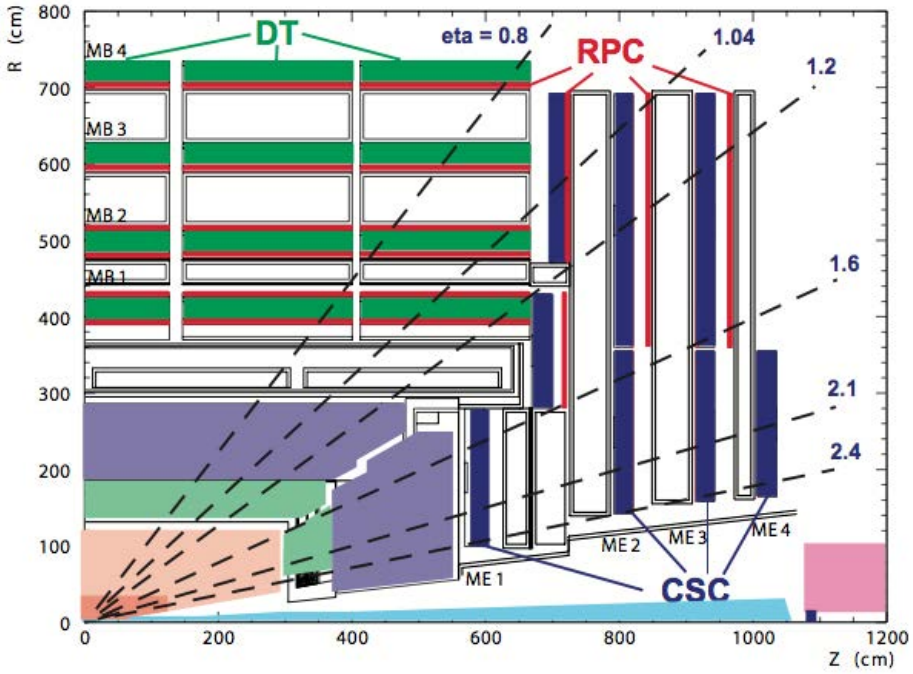

FIGURE 3.8: The positions of the CSCs, DTs, and RPCs are shown within the CMS detector.

tubes are filled with an 85% Ar and 15% CO_2 gas mixture, and a wire held at high voltage runs down the center (Figure 3.9(b)). As a charged particle passes through the gas, it leaves an ionization trail. The resulting charges are collected by the wire, and are read out as an electrical pulse in the wire. The charges drift through the gas towards the wire with a constant velocity called the *drift velocity*. The transverse dimension of a drift cell is 21 mm, which corresponds to a maximum drift time of 380 ns, and a linear relationship between drift path and drift time. Additionally, the individual DT cells are offset by one-half of a cell. By measuring the drift times in the cells, we can resolve the position of the muon, and provide standalone bunch crossing identification. That is, we have sufficient timing resolution to know specifically which proton-proton bunch crossing a muon came from, which is essential for triggering. Each DT chamber is composed of three or two superlayers. The two outer superlayers consist of three layers of staggered drift cells. Their wires are oriented parallel to the beam axis, and measure the coordinate in the $r - \phi$ plane. The

center superlayer is only present in the first three stations, and measures the z coordinate. The layout of the superlayers inside a drift tube chamber is shown in Figure 3.9(a).

Cathode strip chambers are used in the endcaps, which cover $0.9 < |\eta| < 2.4$. This leaves an overlap region between the DTs and CSCs of $0.9 < |\eta| < 1.2$. CSCs are very robust detectors: they can operate in a non-uniform magnetic field, and they do not require precise tuning of gas, temperature, or pressure. This makes them suitable for use in the high-radiation, variable B-field region of the endcaps. The CSCs are multiwire proportional chambers, with 6 anode wires interleaved with 7 cathode panels. The strips are milled on the cathode panels and run radially, and are of fixed width in ϕ. The chambers themselves are trapezoidal, and cover 10° and 20° areas in ϕ, with the exception of ME1/3 which covers the gaps. The ϕ coordinate is found by interpolating between the charges induced on the strips.

The resistive plate chambers (RPC) are gaseous parallel-plate detectors that are able to provide timing resolution of about 1 ns, well within the 25 ns between LHC bunch crossings, which is necessary for triggering. RPCs are capable of resolving position, but they are not as good as DTs or CSCs for this purpose. However, the ability to resolve position is important for resolving $x - y$ ambiguities in the CSCs. The barrel is instrumented with six layers of RPCs, and three layers in the endcaps. This provides a coverage of $|\eta| < 1.6$.

3.8 Trigger

The overwhelming majority of the pp collisions at the LHC are glancing, low-energy collisions. These events do not contain physics processes of interest, and we do not want to read out these events and store them. Proton bunches cross at a rate of 40 MHz, or every 25 ns. Each bunch crossing corresponds to about 1 MB of data from the entire detector. This leads to an enormous data rate of about 40 TB per second. CMS employs a fast hardware-

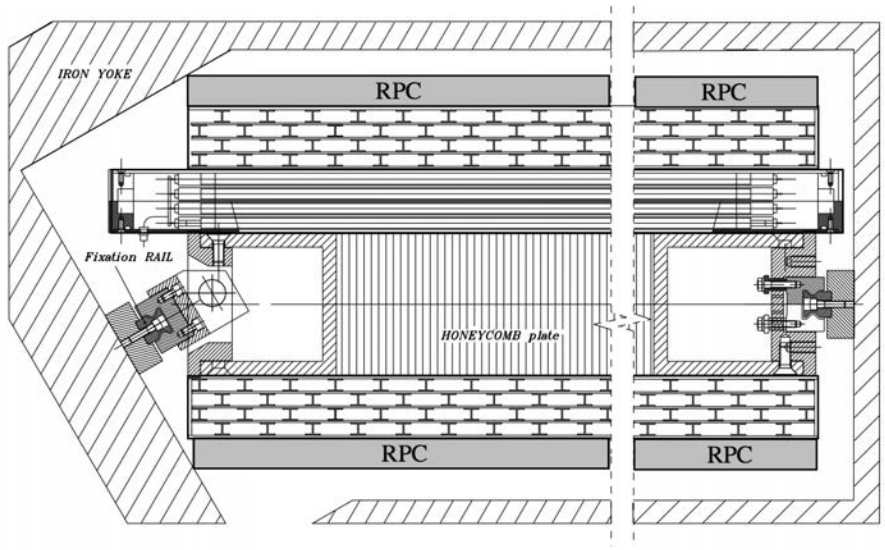

(a) Drift Tube Chamber

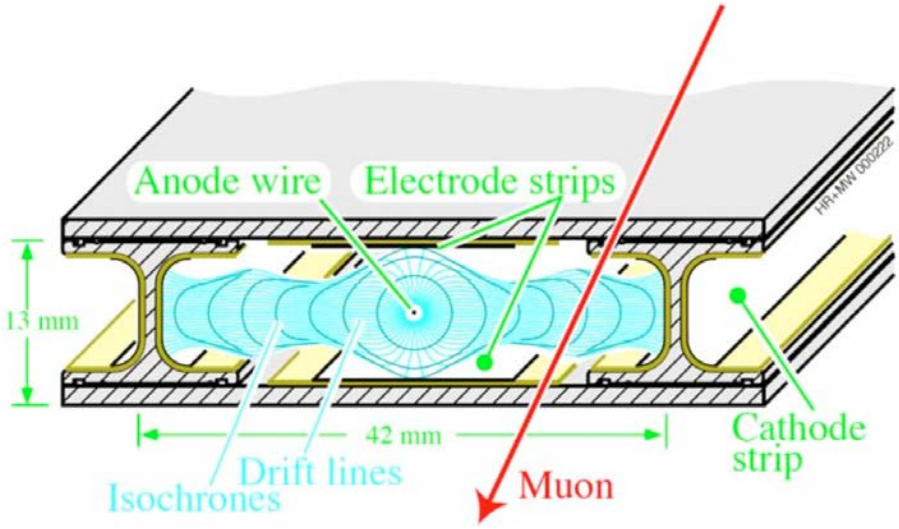

(b) Drift Cell

Figure 3.9: The top figure shows the layout of a drift tube chamber situated inside the iron return yoke. Three superlayers are shown with two along the direction of the beam-pipe, and the other perpendicular to it. The location of the RPCs in the chamber is also shown. The bottom figure shows the inside of a drift cell. The location of the wire, and the drift lines are shown.

based trigger system to provide a first round of selection, followed by a software-based trigger to provide a final layer of selection and categorization before storing the event. The hardware-based trigger is the Level-1 Trigger (L1), and the software-based trigger is the High-Level Trigger (HLT). L1 is designed to reduce the data rate from 40 MHz to a maximum of 100 kHz, and HLT is designed to further reduce the rate to on the order of several hundred hertz.

L1 accepts low-resolution data from the calorimeters and muon system for making keep/reject decisions about a collision event. The high-resolution data is stored in pipelined memory on the front-end electronics, until the final decision is made on whether or not to keep an event. The data-flow of the L1 Trigger is shown in Figure 3.10. The individual subdetectors generate trigger primitives, which are then passed onto the trigger electronics. Regional trigger electronics produce ranked trigger objects in specific areas of the detector. These are passed to global triggers which combine the region information to examine the entire detector. The L1 Global Trigger combines information from both the calorimeter and muon global trigger outputs to make the final decision.

Regional Calorimeter Trigger

The Regional Calorimeter Trigger (RCT) accepts trigger primitives from both HCAL and ECAL. The calorimeters are divided into trigger towers that span $\Delta\eta \times \Delta\phi = 0.087 \times 0.087$. This corresponds to 5×5 ECAL crystals, and a single HCAL tower. The calorimeters are segmented into regions of 4×4 trigger towers, with the exception of HF, where 1 tower is 1 region. The RCT electronics consist of 18 VME crates. Each crate has 7 Receiver Cards (RC), 7 Electron Isolation Cards (EIC), and one Jet/Summary Card (JSC), which utilize ASICs and lookup tables for fast processing. Each card processes two regions, so each crate handles 14 regions.

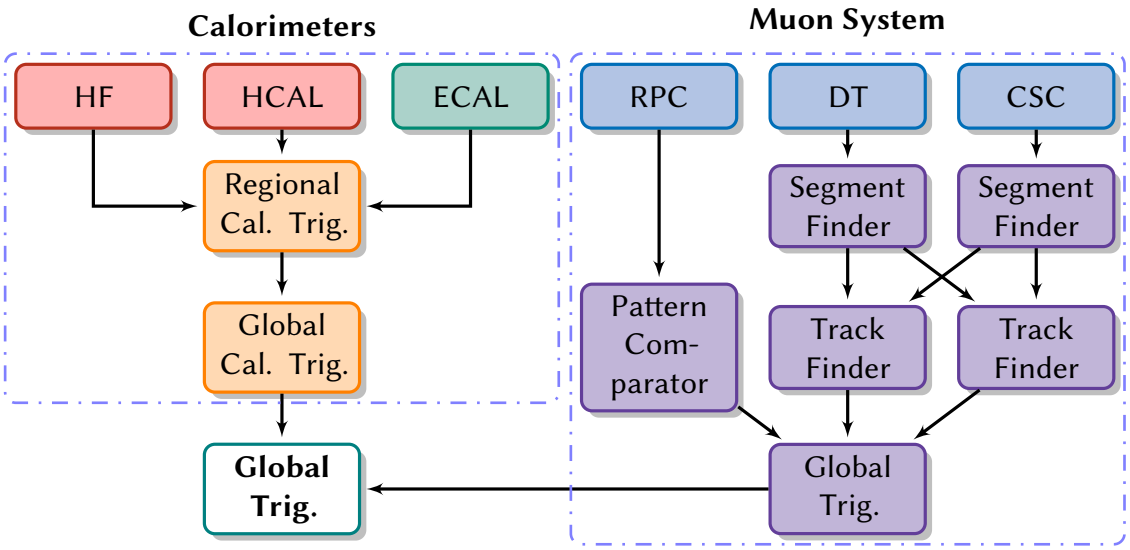

FIGURE 3.10: Data-flow for the level-1 trigger, showing the regional and global stages of the trigger.

RCT identifies the most energetic trigger towers in a region to form e/γ (EG) candidates. Tracking is required to distinguish electrons from photons, which is not used in L1. The EG candidates are categorized as being isolated or non-isolated, and are generated with the EICs. The JSC in each crate identifies the 4 most energetic isolated and 4 non-isolated EG candidates from its 14 regions, and sends them to the Global Calorimeter Trigger (GCT) for further processing. The total transverse energy of each region is computed, and the JSC sends the 4 highest region sums from its crate to the GCT.

High-Level Trigger

The High-Level Trigger (HLT) utilizes software-based triggers that run on the order of 10 000 commercial computing cores. After the initial selection performed by L1, HLT has a larger time budget for performing more sophisticated algorithms for analyzing and selecting events, including the use of tracker data. HLT categorizes the events into different reconstruction "paths". These different paths may specify different combinations

of leptons, isolation requirements, p_T thresholds, etc. For the analyses presented in this thesis, two-electron, three-electron, two-muon, and muon-electron high-level trigger paths are utilized.

4 Event Simulation

A necessary step in studying the physics of LHC *pp* collisions is to model the theoretical predictions of the signal and backgrounds as they would appear in the CMS detector. Computer simulations are the only practical way to create these models. Computing observables and their distributions from the models, as well as including effects from the detector and LHC *pp* collision conditions, requires enormously complex integrals. The "Monte Carlo Method" is the only practical way to evaluate these integrals [42]. Essentially, you use a random number generator to produce outputs that follow a desired probability distribution function. In high-energy physics, we generate individual events of a desired physics process.

To obtain a full picture of a *pp* collision and the detector response, multiple stages of simulation are required. The first step is to calculate the *matrix element* of a particular *hard scattering* process, from which we can obtain the differential cross section for that process. Different software may be used for handling the *underlying event* of a *pp* collision. This involves modeling the low-energy QCD behavior of quarks and gluons that do not directly participate in the hard interaction. Additionally, individual quarks and gluons sometimes appear in the final state of a hard interaction. Another program handles the *showering* and *hadronization* of these particles to form the hadronic jets that appear in the final state. Separate software is used to simulate the passage of radiation through matter, and detector response.

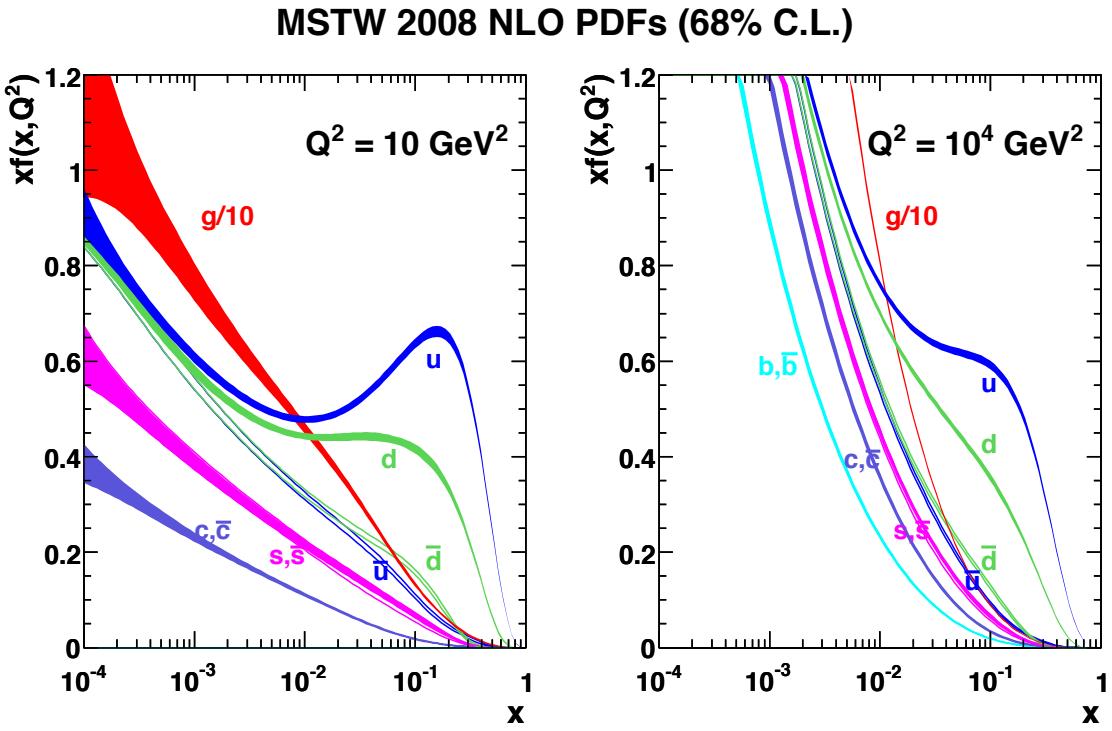

FIGURE 4.1: An example of a parton distribution function computed to NLO provided by the MSTW2008 group, reproduced from [44].

4.1 Parton Distribution Function and Hard Scattering

An important feature of hadron collisions is that the center of mass energy of the hard scattering process is not fixed. This is because the constituents of the protons, the partons, carry some variable fraction, x, of the overall momentum of the proton. The functions that describe how the values of x are distributed are called *parton distribution functions* (PDF). QCD cannot be calculated perturbatively to produce the PDFs, so they are produced by making a global fit to data. Three major groups, CTEQ [43], MSTW [44], and NNPDF [45] compute PDFS and provide periodic updates.

Generation of the hard scattering event starts with sampling the PDF to obtain the energies of the two colliding partons. Next, we have to consider the matrix element for

the interaction of interest. The matrix element is sampled over the relevant phase-space to obtain momenta for the final state particles. The matrix elements themselves come from the relevant Feynman diagrams in the perturbation series. Generators use leading-order (LO, "tree-level") or next-to-leading-order (NLO) terms in the matrix elements. The overall cross section of the process may be computed using a different software package.

4.2 Parton Showers and Underlying Event

The hard scattering portion of the simulation process does not address what happens to quarks and gluons that appear in the final state, or the other partons that did not participate in the hard scattering event (spectators). Specialized generators called Showering and Hadronization Generators (SHGs) are used for modeling these processes.

Perturbative QCD works over very small distance scales or at very high energies. The energy scales for parton showers and the interactions of spectators are outside this regime, so phenomenological models have to be used. One is the Lund string model [46]. As partons separate, the attractive force between them increases. Eventually, the potential energy is sufficient to create a new pair of partons ($q\bar{q}$, gg). Higher-order processes are also considered where a quark can radiate a gluon, and a gluon can produce a quark-antiquark or gluon-gluon pair. This constitutes the parton shower. The partons are then grouped into color singlets, in a process called *hadronization*. Any short-lived resonances that appear after hadronization are decayed (e.g. $\pi^0 \to \gamma\gamma$). The resulting hadrons form a collimated spray of particles called a *jet*. The spectator quarks, though they aren't directly involved in the hard scattering process, are connected to the same hadronization system. So, they are included in the parton showering and hadronization process.

As proton bunches cross, several pairs of protons may interact at the same time. In the LHC, on average 20-30 protons interact during a single bunch crossing during the 7

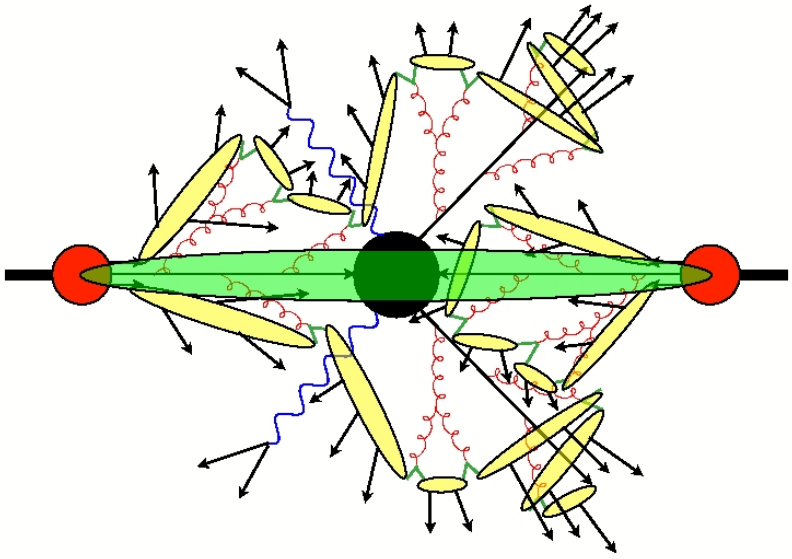

Figure 4.2: This is a diagram of a hadron collision. The hard scattering event is shown in black. The underlying event is highlighted in green, which occurs from interactions between the remaining partons. Quarks and gluons from the underlying event and hard scattering form parton showers. These are grouped into color singlets during hadronization, shown in yellow. The figure is reproduced from [47].

and 8 TeV run periods. This is referred to as *pile-up*. As a final step, soft QCD processes are added to the event in accordance with the number of pile-up events per bunch crossing.

4.3 Event Generators

A variety of software tools are needed to complete the full simulation chain for LHC pp collisions, and the subsequent detection by CMS. Discussed in the next few subsections are the different generators used, and their purposes.

Pythia 6.4

Pythia 6.4 is a general-purpose event generator [48]. It is capable of generating hard scattering events to leading order in perturbation theory. Pythia 6.4 is an SHG, and it is commonly used to perform the hadronization and underlying event step of the event simulation process. For the doubly charged Higgs analysis, Pythia 6.4 is used to simulate pair-production and decay to charged leptons of a doubly charged Higgs signal.

Pythia 6.4 is also used to model the $Z + jets$ reducible background for the spin-parity analysis. The $Z + jets$ samples have been weighted to replicate the data-driven reducible background estimate for the $H \to ZZ \to 4\ell$ analysis performed by CMS [22].

MadGraph 4

MadGraph 4 is a matrix element generator, which will automatically assemble the relevant amplitudes for a desired process. These matrix elements are used to generate events by MadEvent to leading-order or next-to-leading order [49, 50]. Both generators are often referred to collectively as simply "Madgraph". MadGraph 4 is capable of assembling the amplitudes for multiple final states at tree level, making it a natural choice for processes with high-multiplicity final states. This is especially useful for multi-jet final states, so it is used for simulating the $Z + jets$ backgrounds for the doubly charged Higgs analysis. MadGraph 4 is also used to produce double top and WZ backgrounds. MadGraph 4 does not perform the parton showering and hadronization step, so it must be interfaced with Pythia 6.4 to provide these features.

Powheg

Powheg (POsitive Weight Hardest Emission Generator) is a next-to-leading-order event generator [51]. Powheg generates the hardest (most energetic) emission first to NLO,

independently of the parton shower. During the parton showering process, the hard emission is omitted, and other emissions are not included if they are more energetic than the hard event. POWHEG is needed for vector boson and Higgs production, since these processes occur at NLO.

It is used to generate $q\bar{q} \to ZZ \to 4\ell$ background samples. An important component of this background is a single Z decaying to two leptons where one lepton radiates another Z/γ. This, in turn, decays to two leptons to give a four-lepton final state. This process can only be modeled at NLO. POWHEG is used to generate the single top backgrounds used in the doubly charged Higgs analysis.

POWHEG must also handle the production of the Standard Model Higgs and alternate spin-parity configurations tested against the SM signal. Higgs production through gluon fusion (Figure 1.5) requires a quark-loop, and is a NLO process. The decays are handled by JHUGEN 2 to properly model the spin and polarization correlations of the final state. The doubly charged Higgs analysis also makes use of a simulated Higgs signal, although it does not need the spin-parity information provided by JHUGEN 2. In this case, we use POWHEG to handle production and decays for $gg \to H \to 4\ell$.

GG2ZZ

The ZZ diboson background can also occur via a gluon fusion process. GG2ZZ is a dedicated tool used to generate $gg \to ZZ$ decaying to a four-lepton final state at NLO [52]. This process only occurs at $O(\alpha_s^2)$ compared to that of $q\bar{q}$, but it becomes significant in the high gluon flux environment of LHC pp collisions.

JHUGen 2

The JHU Generator, or JHUGen 2, is a specialized event generator for providing full spin and polarization correlations of the final state particles from the decay of some resonance, X [12, 24, 25]. JHUGen 2 also takes into account the effects of the production mode of X, which could be $q\bar{q}$, gg, vector-boson fusion (VBF), or associated production (VH). The resonance itself can be spin-0, spin-1, or spin-2, with couplings that can be specified according to the needs of the study. Powheg is used to handle the production of the resonance from partons, and JHUGen 2 is used to handle the decays for the standard model Higgs signal sample with $m_H = 126\,\text{GeV}$ as well as the alternate spin-parity configurations tested against the SM signal.

The Higgs cross section is computed to next-to-leading-logarithmic order and next-to-next-to-leading-order (NNLL + NNLO) [53]. The same cross section is used for the SM Higgs and alternate spin-parity samples. The samples are listed in Table 4.1.

4.4 Detector Simulation

Up to this point, we've covered the simulation of a pp collision, the hard scattering event, and the propagation to the final state particles, including hadronization. The next step is to simulate how the final state particles behave as they pass through the detector. The software package Geant4 is used to accomplish this [54]. Ultimately, Geant4 simulates the passage of particles through matter. This includes the energy loss and decays of particles as they pass through the different materials that compose the detector, as well as how the detector itself responds to the presence of particles. From this information, the electronic responses can modeled to produce the raw digital output of the CMS detector. From this point forward, simulated data and real pp collision data follow the same processing and analysis chain. The agreement between simulation and data is verified using control plots,

which are given in Chapters 7 and 8.

4.5 Simulated Samples

The simulated Monte Carlo samples for the $H \to ZZ \to 4\ell$ spin-parity analysis and the doubly charged Higgs search are listed in the following tables. The signal samples are in Table 4.1 and the background samples are listed in Table 4.2.

Process	Generator	$\sigma \cdot$ BR (fb)	Boson Mass (GeV)
Higgs Boson Spin-Parity $H \to ZZ^* \to 4\ell$			
$gg \to H(0^+)$	JHUGen 2	2.79317	126
$gg \to H(0^-)$	JHUGen 2	2.79317	126
$gg \to H(0_h^+)$	JHUGen 2	2.79317	126
$gg \to H(2_m^+)$	JHUGen 2	2.79317	126
$q\bar{q} \to H(2_m^+)$	JHUGen 2	2.79317	126
Doubly-Charged Higgs			
$gg \to H \to 4\ell$	Powheg	5.31852	125
$q\bar{q} \to \Phi^{++}\Phi^{--} \to 4\ell$	Pythia 6.4	352.49	110
	Pythia 6.4	186.21	130
	Pythia 6.4	106.55	150
	Pythia 6.4	64.641	170
	Pythia 6.4	33.209	200
	Pythia 6.4	12.714	250
	Pythia 6.4	5.5458	300
	Pythia 6.4	2.6413	350
	Pythia 6.4	1.3414	400
	Pythia 6.4	0.71531	450
	Pythia 6.4	0.39604	500
	Pythia 6.4	0.13271	600
	Pythia 6.4	0.0483282	700

Table 4.1: Signal Monte Carlo samples. They have been generated for pp collisions of $\sqrt{s} = 8$ TeV. They include the different spin-parity configurations examined, including the SM pure-scalar 0^+ hypothesis. The different mass points used in the doubly charged Higgs search are included. The JHUGen 2 samples have been normalized to NNLL + NNLO in cross section, and the Pythia 6.4 samples have been normalized to NLO in cross section.

Process	Generator	$\sigma \cdot$ BR (pb)
Diboson		
$ZZ \to 4e,\ 4\mu,\ 4\tau$	Powheg	0.07691
$ZZ \to 2e2\mu,\ 2e2\tau,\ 2\mu2\tau$	Powheg	0.1767
$gg \to ZZ \to 4\ell$	gg2ZZ	0.0048
$gg \to ZZ \to 2\ell2\ell'$	gg2ZZ	0.01203
$WZ \to 3\ell\nu$	MadGraph 4	1.058
$WZ \to 2\ell2q$	MadGraph 4	2.207
Drell-Yan with Jets		
$Z + 1jet$	MadGraph 4	666.30
$Z + 2jet$	MadGraph 4	214.97
$Z + 3jet$	MadGraph 4	60.691
$Z + 4jet$	MadGraph 4	27.364
Drell-Yan with Jets (inclusive)		
$Z + jets$	Pythia 6.4	†
Single Top		
$t(s)$	Powheg	3.79
$\bar{t}(s)$	Powheg	1.56
$t(t)$	Powheg	56.4
$\bar{t}(t)$	Powheg	30.7
$t(t)W$	Powheg	11.1
$\bar{t}(t)W$	Powheg	11.1
Double Top		
$t\bar{t} \to 2l2\nu$	MadGraph 4	25.35
$t\bar{t} \to 2q2\nu$	MadGraph 4	105.79
$t\bar{t}\gamma$	MadGraph 4	2.166
$t\bar{t}W$	MadGraph 4	0.2057
$t\bar{t}WW$	MadGraph 4	0.002
$t\bar{t}Z$	MadGraph 4	0.232

Table 4.2: Background Monte Carlo samples. They have been generated for pp collisions of $\sqrt{s} = 8$ TeV. All of these are used in the doubly charged Higgs analysis. The spin-parity analysis uses the ZZ samples. They have been reweighted to NLO in cross section. † These have been weighted to replicate the data-drive reducible background estimate in the CMS $H \to ZZ \to 4\ell$ analysis.

5 Event Reconstruction

The raw, digitized output of the CMS subdetectors are not immediately useful for performing a physics analysis. The electronic signals have to be abstracted into higher-level objects that are of use to an analyst. Tracker hits have to be formed into continuous tracks, calorimeter deposits need to be translated into energy values, etc. These are then utilized to form particle candidates. In particular, we are concerned with reconstructing muon and electron candidates. CMS employs a suite of complex algorithms for performing these tasks, which are implemented in C++ to take advantage of object-oriented programming and the speed of a compiled language.

5.1 Electrons

Electrons are reconstructed using the tracker and the electromagnetic calorimeter. As electrons travel through the detector, they leave hits in the tracker until they hit ECAL, where they deposit virtually all of their remaining energy, forming a cluster of energy in ECAL. As their trajectories bend through the magnetic field, the electrons emit bremsstrahlung photons. These photons form more ECAL clusters that extend in the ϕ direction from the electron cluster. These clusters are grouped together into a supercluster (Figure 5.1).

Electrons are reconstructed using two complementary methods: *tracker driven* and *ECAL driven* seeding [55]. The former is optimized for low p_T electrons that often occur

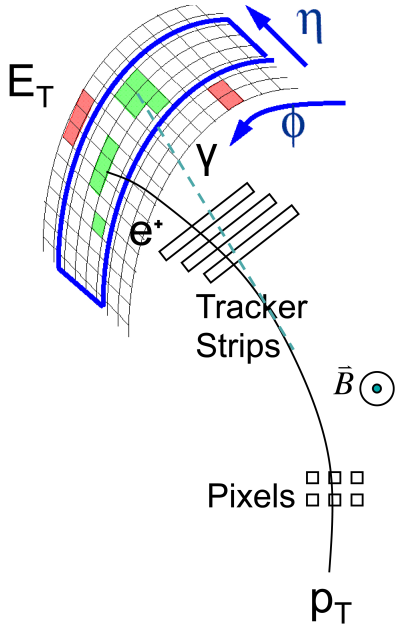

FIGURE 5.1: Diagram of an electron candidate in the CMS detector. The arc of the electron's path is shown as it passes through the magnetic field. The ECAL clusters from the electron and its bremsstrahlung photons are shown as green squares in ECAL. The supercluster is boxed in blue.

inside jets. The latter is optimized for higher p_T electrons that come from W or Z decays, which is relevant to the spin-parity and doubly charged Higgs analyses.

The ECAL driven method begins by forming ECAL superclusters (SC) with $E_T >$ 4 GeV. The clusters are narrow in η, but extend out in ϕ from bremsstrahlung, which is taken into account when forming the supercluster. Superclusters are matched to track seeds, which are formed from two to three hits in the inner tracker layers. This forms the basis of the electron track. The rest of the track is generated by fitting the tracker hits using a Gaussian Sum Filter [56]. As electrons lose energy to bremsstrahlung, the radius of their trajectories becomes smaller, and kinks appear when a photon is emitted. The Gaussian Sum Filter takes these effects into account when fitting the track.

5.2 Muons

Muon candidates are reconstructed utilizing signals in the tracker and the muon system. Muons are about 200 times more massive than electrons. As a result, they experience relatively little energy loss as they travel through the detector. They are referred to as minimum ionizing particles (MIPs) and deposit only minimal amounts of their energy in the calorimeters, so the calorimeters do not play a central role in reconstructing muons.

Reconstruction of a muon can follow an inside-out or outside-in approach [57]. The first is what is referred to as a *Tracker Muon*. This starts with tracks from the silicon tracker with $p_T > 0.5\,\text{GeV}$ and $p > 2.5\,\text{GeV}$. The tracks are extrapolated out to the muon system, accounting for curvature due to the magnetic field, expected energy loss, and multiple Coulomb scattering in the detector. Tracks that align with at least one track segment from a DT or a CSC are identified as tracker muons.

The outside-in approach produces *Global Muons*, which start with tracks present in the muon system. A matching silicon tracker track is found by propagating the muon and tracker tracks to a common surface. Once track pairs have been found, the tracks are merged using a Kalman-filter technique [58].

Tracker muons are more efficient at lower p_T since only a single segment is required from the muon system. Higher p_T muons will register in multiple muon system segments which make Global Muons more efficient in this situation. For muons with p_T less than about 200 GeV, the p_T resolution is dominated by the silicon tracker. At p_T values of about 200 GeV, the muon system begins to contribute more significantly to the p_T resolution.

5.3 Particle Flow

Particle-flow is a powerful technique utilized by CMS which combines information from all of the CMS subdetectors to reconstruct all stable particles in the event [59]. This includes electrons, muons, photons, charged hadrons, and neutral hadrons. An important feature is that these are exclusive categories, and there is no overlap between them. In turn, these can be used to construct higher-level physics objects, like missing transverse energy, jets, and taus.

The algorithm utilizes charged-particle tracks, calorimeter clusters, and muon tracks as basic elements. The particle-flow "link" algorithm links these together, and uses the distance between linked elements as a measure of the quality of the link. These linked elements are grouped into blocks of elements connected directly or indirectly. Particles are then identified within each block. Global muons are identified first if a muon's combined momentum is compatible with the tracker measurement only. The elements corresponding to the muon are removed from the block, and the algorithm proceeds with reconstructing electrons using the criteria discussed earlier in this chapter. Elements remaining in the block may be identified as charged hadrons, neutral hadrons, or photons.

For the purpose of the spin-parity and doubly charged Higgs analyses, particle-flow is used to compute the amount of energy surrounding each lepton candidate. Placing an upper limit on the allowed amount of the surrounding energy is called *isolation*, and will be discussed in Chapter 6. Additionally, the muon candidates used in the analyses are identified using particle-flow criteria. Because the analyses rely so heavily on electrons and muons, it is important that electron and muon candidates are disambiguated, which the particle-flow algorithm ensures.

6 Event Selection

The spin-parity and doubly-charged Higgs analyses share much of the initial selection and identification of the leptons, as well as the datasets and triggers. Both of them examine 4ℓ final states where $\ell = e$ or μ. The initial selections on the individual leptons are relatively loose in order to attain high efficiency. However, the topology of 4ℓ final states is quite rare, as there are very few Standard Model processes that can produce it. This helps reduce the backgrounds significantly. Selecting the specific combination of four leptons for each analysis are discussed in later chapters.

6.1 Online Selection

The data collected by the CMS experiment are organized into *primary datasets*, which contain collections of related high-level trigger paths. The spin-parity and doubly charged Higgs analyses use double-muon, double-electron, and muon-electron primary datasets. There is overlap between the muon-electron dataset and the other two. Each recorded event is uniquely identified by a run number, luminosity section, and event number. These numbers are utilized to ensure that events are not double-counted. The datasets consist of $19.7\,\text{fb}^{-1}$ of $\sqrt{s} = 8\,\text{TeV}$ LHC pp collisions taken during the 2012 run period.

The high-level trigger paths utilized in the two analyses are listed in Table 6.1. The p_T values given indicate the threshold energies for those triggers. Because p_T resolution

isn't perfect, the efficiency doesn't immediately jump to its maximum value after the threshold. Instead, it rises up to maximum efficiency a few GeV past the threshold. This rise is referred to as a *turn-on curve*. To ensure that the analysis is performed well above the turn-on curve, the leptons are sorted from highest to lowest in p_T, and we impose the following requirement:

$$p_T^{\text{leading}} > 20\,\text{GeV} \quad \text{and} \quad p_T^{\text{sub-leading}} > 10\,\text{GeV} \tag{6.1}$$

Trigger Type	HLT Path	L1 Seed
Electron	$2e$ with $p_T > 17,\ 8$ $3e$ with $p_T > 15,\ 8,\ 5$	$2e/\gamma$ with $E > 13,\ 7$ $3e/\gamma$ with $E > 12,\ 7,\ 5$
Muon	2μ with $p_T > 17,\ 8$ 2μ with $p_T > 17,\ 8$ (tracker)	2μ with $E > 10,$ any 2μ with $E > 10,$ any
Electron/Muon	$e\mu$ with $p_T > 17,\ 8$ $e\mu$ with $p_T > 8,\ 17$	$e/\gamma, \mu$ with $E > 12,$ any $e/\gamma, \mu$ with $E > 6,\ 12$

Table 6.1: The high-level trigger paths and their L1 trigger seeds. The p_T and E values are given in GeV. "Tracker" indicates that the muon is only required at tracker level, whereas the others are global muons. Calorimeter and tracking isolation and ID are applied to the electron HLT paths. "Any" means that any value of E is allowed.

6.2 Electron Selection

Electrons are reconstructed following the procedure outlined in the previous chapter. We begin by requiring that the electrons have $p_T > 15\,\text{GeV}$ for the doubly charged Higgs analysis, and $p_T > 7\,\text{GeV}$ for spin-parity. They are also required to be in the fiducial range of the detector, with $|\eta| < 2.5$. After track fitting occurs, electrons are required to have no more than 1 missing hit in the tracker to reject converted photons. This occurs when a photon produces an e^+e^- pair when it interacts with the material in the tracker.

Requirements on impact parameter, isolation, and identification are described in the following subsections. For the spin-parity analysis only, the electrons receive energy

corrections which enhance the 4ℓ invariant mass resolution. This is important, as the Higgs signal appears as a resonance in the 4ℓ invariant mass distribution, which is used to select the signal.

Impact Parameters

We want to ensure that the electrons used in the analysis are produced at the primary vertex of a pp collision, rather than a secondary process. These are referred to as *prompt* electrons. The relevant quantities are related to the distance of the electron's impact parameter to the primary vertex of the event. We place requirements on the transverse ($d_{xy} < 0.5\,\text{cm}$) and longitudinal ($d_z < 1.0\,\text{cm}$) impact parameters where d refers to the distance between the primary vertex and the electron's impact parameter. We also place a requirement on the significance of the impact parameter

$$\text{SIP}_{3\text{D}} = \left|\frac{\text{IP}}{\sigma_{\text{IP}}}\right| < 4 \tag{6.2}$$

where IP is the 3D total distance between the electron's impact parameter and the primary vertex, and σ_{IP} is the uncertainty of the value.

Isolation

Isolation refers to the amount of energy deposits surrounding a lepton, and it is a powerful quantity for discriminating against fake lepton signatures commonly found in jets. Electron isolation is computed by summing the p_T from charged hadron, neutral hadron, and photon collections generated using particle-flow (PF) [59]. We restrict the particles used in the isolation sum to be in the vicinity of the electron by imposing the following requirement:

$$\Delta R = \sqrt{\Delta\phi^2 + \Delta\eta^2} \tag{6.3}$$

$$\Delta R < 0.4 \tag{6.4}$$

where $\Delta\phi$ and $\Delta\eta$ are the differences between the electron's and another particle's ϕ and η coordinates.

The isolation sum needs to be computed from particles originating in the same hard scattering event as the electron. Because of pile-up, the energy sum could become contaminated with extraneous particles, which degrades the effectiveness of isolation. To mitigate the pile-up contamination from charged particles, we assert a requirement called "`pfNoPileup`" on the charged PF particles, which ensures that their tracks originate at the primary vertex.

The `pfNoPileup` procedure does not work for the neutral components as they have no tracks. The expected energy density, ρ, from neutral hadrons and photons is computed using an algorithm called FastJet [60, 61]. In this procedure, the average energy density from all jet activity is computed as a function of the number of pile-up vertices. To obtain the expected energy contribution, we have to multiply ρ by an effective area A_{eff}. A_{eff} is the slope of the average isolation divided by ρ as a function of the number of pile-up vertices. The effective areas used in the analyses are computed from selected $Z \to ee$ events, and are provided by the electron/photon Physics Object Group (POG).

Another effect to be accounted for is the fact that the average energy present around an electron increases with its p_T. By placing a hard cutoff on the isolation energy, we would eliminate otherwise good electrons with high p_T. To avoid this, the isolation sum is divided by the electron's p_T. We call this *relative isolation*.

Putting everything together, the isolation for an electron is defined as

$$I_{rel}^{pf} = \frac{1}{p_T^{(e)}}\left[\sum p_T^{(ch)} + \max\left(\sum p_T^{(nh)} + \sum p_T^{(\gamma)} - \rho \cdot A_{\text{eff}},\ 0.0\right)\right] \tag{6.5}$$

where $p_T^{(e)}$, $p_T^{(ch)}$, $p_T^{(nh)}$, and $p_T^{(\gamma)}$ are from the electron, charged hadrons, neutral hadrons, and photons respectively. The max statement is to ensure that the corrected neutral energy component does not drop below zero. This is referred to as particle-flow relative isolation

at CMS. We require that all electrons have $I_{rel}^{pf} < 0.4$.

Identification

Electrons undergo an additional identification process to further improve the purity of the selected electrons. The method employs a Boosted Decision Tree (BDT) machine-learning technique [62, 63]. The BDT is constructed from observables sensitive to electron bremsstrahlung, geometrical and momentum matching between the electron track and calorimeter clusters, and shower shape. The BDT was trained with simulated Higgs boson signal events, and $W+1$ fake electron background samples taken from data. A cut is placed on the BDT output values depending on the p_T and η value of a particular electron. The cuts are summarized in Table 6.2.

p_T	$\lvert\eta\rvert$	BDT Output
5 – 10 GeV	< 0.8	> 0.47
	$0.8 - 1.479$	> 0.004
	> 1.479	> 0.295
> 10 GeV	< 0.8	> -0.34
	$0.8 - 1.479$	> -0.65
	> 1.479	> 0.60

Table 6.2: Electron multivariate identification utilizing a Boosted Decision Tree (BDT). The cut on the BDT value is dependent on the p_T and η of the particular electron.

Energy Regression and Calibration

The momentum assigned to an electron candidate is a combination of the p_T inferred from its track and the energy it deposits in ECAL. A Boosted Decision Tree is utilized to calculate the momentum values, as well as track and cluster quality variables [64, 65]. The BDT is trained on a simulated di-electron sample for the ECAL barrel and endcap sections separately. The BDT corrects for effects such as non-containment of the electron shower

in the reconstructed clusters, energy leakage in the calorimeters, pile-up, and overlapping electron showers.

The electron energies receive corrections to further improve their energy resolution. These aim to correct for discrepancies in tracker alignment, ECAL crystal imperfections, and crystal transparency loss from radiation damage. The procedure originated in the CMS $H \to \gamma\gamma$ analysis [66].

The first step is comparing the displacement of the $Z \to ee$ resonance peak in data and simulation. This is done in different η regions which are divided into two categories based on the amount of bremsstrahlung. These corrections are time-dependent, since the transparency of the ECAL crystals varies with time as they accumulate radiation damage. The corrections obtained in the comparison are applied to the data.

The second step is correcting the p_T-dependent differences between data and simulation. This is done by comparing the $Z \to ee$ peaks binned in p_T and η of one of the two electrons. The resulting linearity corrections to the momentum scale are applied to the data.

Finally, the resolution of the simulated electrons needs to be adjusted so they model the data properly. To do this, the supercluster energies of individual simulated electrons are smeared by applying a Gaussian factor of mean 1 and width $\Delta\sigma$. The degree of smearing is chosen to match the simulated Z resonance shape to data.

6.3 Muon Selection

Muons are first reconstructed using the tracker and muon system, as described in the last chapter. Muons used in both analyses are required to have $p_T > 5\,\text{GeV}$ with $|\eta| < 2.4$.

Impact Parameters

Muons receive the same impact parameter requirements as electrons: $d_z < 1\,\text{cm}$, $d_{xy} < 0.5\,\text{cm}$, and $|\text{SIP}_{3\text{D}}| < 4$.

Isolation

The isolation of muons in the spin-parity analysis is computed in the same way as the electrons, with the requirement that $I_{rel}^{pf} < 0.4$. They also include the ρ correction for pile-up.

The isolation is computed differently for doubly charged Higgs analysis. The difference is in how we correct for pile-up. Rather than ρ corrections, they receive what are referred to as $\Delta\beta$ corrections, following the CMS Muon Physics Object Group recommendation. The isolation is defined as

$$I_{rel}^{pf} = \frac{1}{p_T^{(\mu)}}\left[\sum p_T^{(ch)} + \max\left(\sum p_T^{(nh)} + \sum p_T^{(\gamma)} - \Delta\beta,\ 0.0\right)\right] \tag{6.6}$$

where $p_T^{(\mu)}$, $p_T^{(ch)}$, $p_T^{(nh)}$, and $p_T^{(\gamma)}$ are from the muon, charged hadrons, neutral hadrons, and photons, as before. The definition of $\Delta\beta$ is

$$\Delta\beta = \frac{1}{2}\sum p_T^{(ch,PU)}. \tag{6.7}$$

$p_T^{(ch,PU)}$ refers to the total p_T of reconstructed charged hadrons that are not associated with the primary vertex. Neutral hadrons comprise about 1/3 of the energy of a jet [67]. This means that the neutral hadron contribution is about 1/2 of the charged hadron contribution, hence the factor of 1/2. The performance of $\Delta\beta$-corrected isolation has nearly identical performance to ρ-corrected, so it receives the same isolation requirement of

$$I_{ref}^{pf}(\Delta\beta) < 0.4$$

Identification

The muons used in both analyses may be reconstructed as either Tracker or Global muons, and they follow the *Particle-Flow Muon* selection prescription [68]. Three criteria are applied sequentially to select muons from the raw reconstructed (RECO) muons.

1. Isolated – A RECO muon may be identified as isolated if the sum of the p_T from tracks and the E_T from calorimeter deposits within $\Delta R < 0.3$ of the muon are less than 10% of the muon's p_T. In addition, these muons are required to be Global Muons to ensure that a valid track exists between the tracker and muon system [57].

2. PF-Tight – A RECO muon must first be constructed as a Global Muon, with $\chi^2/d.o.f. < 10$ for the track fit. The tracker track must match at least two muon stations, use > 10 inner tracker hits, and ≥ 1 pixel hit [57].

3. PF-Loose – A RECO muon must be a Tracker Muon, and the track must match at least one muon segment [57].

Muons passing these requirements are passed through the particle-flow procedure to create the collection of muons used for analysis [59].

6.4 Final State Radiation Recovery

When a Z decays to two leptons, a lepton may radiate a nearly collinear photon, producing a final state of $Z \rightarrow \ell\ell\gamma$. These consist of higher energy photons that might not be captured as part of an electron's bremsstrahlung photons. Muons are not reconstructed in association with photons at all. These photons are referred to as final-state radiation (FSR). Since they carry away some of the energy of the Z decay, they harm the invariant mass resolution of the two leptons. Therefore, it is desirable to include them. This procedure is

only used in the spin-parity analysis since we look for a Higgs decaying to two Z bosons. Including FSR photons provides better resolution of the Z masses, and the 4ℓ invariant mass.

Two collections of photons are used for FSR recovery. The first are particle-flow photons with a dedicated clustering algorithm efficient down to 230 MeV in the ECAL barrel and 600 MeV in the endcap [67]. The second collection is formed from the particle-flow muon collection. Muons can produce showers in ECAL, although rarely. During the particle-flow process, these ECAL deposits are linked to the muon, and are not categorized as separate particles. Some of these deposits are collinear FSR photons, so we include ECAL deposits from particle-flow muons as FSR candidates.

The FSR photon candidates are required to have $p_T > 2.0\,\text{GeV}$ and $|\eta| < 2.4$. We also place an isolation requirement on the photons. The particles used in the isolation sum must be within $\Delta R < 0.3$ from the photon, $p_T > 0.2\,\text{GeV}$ for charged hadrons, and $p_T > 0.5\,\text{GeV}$ for photons and neutral hadrons, including ones from vertices other than the primary vertex.

$$I_{rel} = \frac{1}{p_T^{(FSR)}}\left(\sum p_T^{(ch)} + \sum p_T^{(nh)} + \sum p_T^{(\gamma)}\right) \tag{6.8}$$

For each photon, we consider its closest lepton (closest in ΔR). If ΔR between the photon and lepton is < 0.07, we accept the photon. If ΔR between the photon and lepton is < 0.5, we accept the photon if it has $p_T > 4.0\,\text{GeV}$ and $I_{rel} < 1.0$. The final selection on the individual FSR photons occurs when the $H \to ZZ \to 4\ell$ candidate is constructed, and it described in Chapter 7.

6.5 Scale Factors

An important part of the analysis is understanding the selection efficiency of electrons and muons. Since the Monte Carlo simulations do model detector response, and use the same reconstruction algorithms as the data, they do provide an estimate of the expected efficiency. To make sure that efficiency is properly represented in the simulation, we calculate the efficiencies from simulation and data. We then apply weights (scale factors) to the simulated events to bring them into agreement with data. In particular, we are interested in measuring the efficiency of selecting muons and electrons after isolation, identification, and impact parameter requirements.

The efficiency is measured for the leptons using the *tag-and-probe* method, which is nearly ubiquitous in high-energy physics [69]. You begin with selecting di-lepton events, where you apply very strict requirements on one of the leptons to ensure high purity. This lepton is referred to as the *tag*. The second *probe* lepton does not have the isolation, identification, and impact parameter selections applied. The invariant mass of the two leptons are plotted around the Z resonance. By fitting the Z resonance and background, we get an estimate of the number of events in the Z signal region.

Next, we apply the lepton selections to the probe lepton, and repeat the plotting and fitting of the invariant mass, and obtain the number of events in the signal region. The number of events after selection divided by the number of events before selection gives us an estimate of the efficiency.

This is performed in bins of p_T and η for the probe lepton, and is done for both simulation and data. We then calculate the correction factors that bring the simulation efficiency into agreement with data.

6.6 Pile-Up

Pile-up is part of the Monte Carlo simulation process, however it does not necessarily reflect the conditions in the real LHC *pp* collisions. As with the efficiencies, we apply weighting factors to the individual simulated events to bring the pile-up distribution into agreement with data.

The procedure begins by histogramming the number of reconstructed vertices per event for simulation, and again separately for data. We then divide the data histogram by the simulation histogram. The result is a histogram where the bin value is the correction factor for a given number of reconstructed vertices. Each simulated event is assigned one of these correction factors based on how many reconstructed vertices it has. This brings the simulated pile-up distribution into agreement with data.

7 Spin-Parity of the Higgs Boson in $H \to ZZ \to 4\ell$ at 8 TeV

As discussed in Chapter 2, CMS has performed a spin-parity analysis of the Higgs boson in the $H \to ZZ \to 4\ell$ channel [22]. They have utilized the 4ℓ invariant mass, the masses of the Z candidates, and five kinematic angles to provide discrimination between the standard model pure-scalar hypothesis and alternate spin-parity hypotheses. The spin-parity analysis presented here is a complementary approach based on *Inferring the Nature of the Boson* [70], where only three of the five kinematic angles are used in uni-angular distributions: θ_1, θ_2, and Φ.

$$\frac{1}{\Gamma_f}\frac{d^2\Gamma}{dq_2^2\, d\cos\theta_1} = \frac{1}{2} + T_2 P_2(\cos\theta_1) - T_1 \cos\theta_1$$
$$\frac{1}{\Gamma_f}\frac{d^2\Gamma}{dq_2^2\, d\cos\theta_2} = \frac{1}{2} + T_2 P_2(\cos\theta_1) - T_1 \cos\theta_1$$
$$\frac{2\pi}{\Gamma_f}\frac{d^2\Gamma}{dq_2^2\, d\phi} = 1 + U_2 \cos 2\phi + V_2 \sin 2\phi + U_1 \cos\phi$$

There are a few difficulties that arise from using the exact method outlined in the paper. The T_i parameters are not constants, but are functions of the off-shell Z mass. Additionally, the method employs a complex decision tree that requires exact knowledge of the coefficients in the uni-angular distributions. So, rather than fitting to the uni-angular distributions, a 3D p.d.f. is formed from the three angles, and is used to compute a log-likelihood ratio test statistic to discriminate between different signal hypotheses.

In this analysis, the Standard Model 0^+ hypothesis is compared against 0^-, 0_h^+, $2_m^+(gg)$, and $2_m^+(q\bar{q})$ hypotheses. The models and notation follow the CMS prescription, and are described in Table 2.1 with the previous CMS results. Like the original CMS analysis, we consider electrons and muons in the final state, so we have the following categories: $4e$, 4μ, and $2e2\mu$.

7.1 Event Reconstruction and Selection

We begin with electron and muon candidates with the p_T, η, impact parameter, momentum calibrations, and identification requirements outlined in Chapter 6. For the photons selected as final state radiation (FSR) candidates, we assign a photon to its closest lepton in ΔR for all selected leptons.

For all opposite-sign, same-flavor (OSSF) lepton pairs, we choose the pair with an invariant mass closest to the nominal Z mass, and assign that pair to be Z_1. Of the remaining leptons, we choose the OSSF pair with the largest scalar p_T sum, and assign that pair to be Z_2. For the photons assigned to the leptons of a Z candidate, we select a photon if the inclusion of its 4-momentum brings the Z candidate's mass closer to nominal, and $4\,\text{GeV} < m(\ell\ell\gamma) < 100\,\text{GeV}$. If more than one photon passes, we select the one with the highest p_T provided it is greater than 4 GeV. Otherwise, we choose the photon with the smallest ΔR to its lepton. No more than one FSR photon may be assigned to a Z candidate. Next, we apply the following selections:

- Requirements on the Z candidates' invariant masses

$$40 < m_{Z_1} < 120\,\text{GeV} \tag{7.1}$$

$$12 < m_{Z_2} < 120\,\text{GeV} \tag{7.2}$$

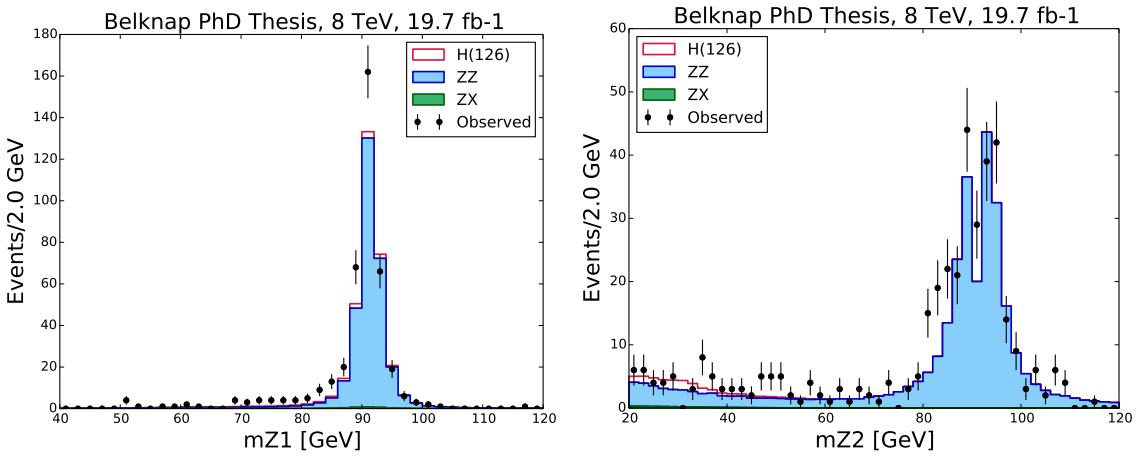

(a) m_{Z_1} (b) m_{Z_2}

FIGURE 7.1: The di-lepton invariant mass distributions for the Z_1 and Z_2 candidates. They include contributions from all final states: $4e$, 4μ, and $2e2\mu$.

- Isolation requirement for the leptons, $I_{rel}^{pf} < 0.4$. We, ensure that the energy of any FSR photons do not appear the leptons' isolation sums.

- Trigger threshold (see section 6.1)

$$p_T^{\text{leading}} > 20.0\,\text{GeV} \text{ and } p_T^{\text{sub-leading}} > 10.0\,\text{GeV}$$

- To suppress QCD contamination, we require that all opposite-sign leptons (regardless of flavor) have an invariant mass $> 4\,\text{GeV}$.

- We apply a mass window around the signal region: $121.5 < m_{4\ell} < 130.5\,\text{GeV}$.

With the exception of the mass window, the 4ℓ invariant mass distributions after final selection are shown in Figure 7.2. The di-lepton invariant mass distributions for Z_1 and Z_2 are shown in Figure 7.1.

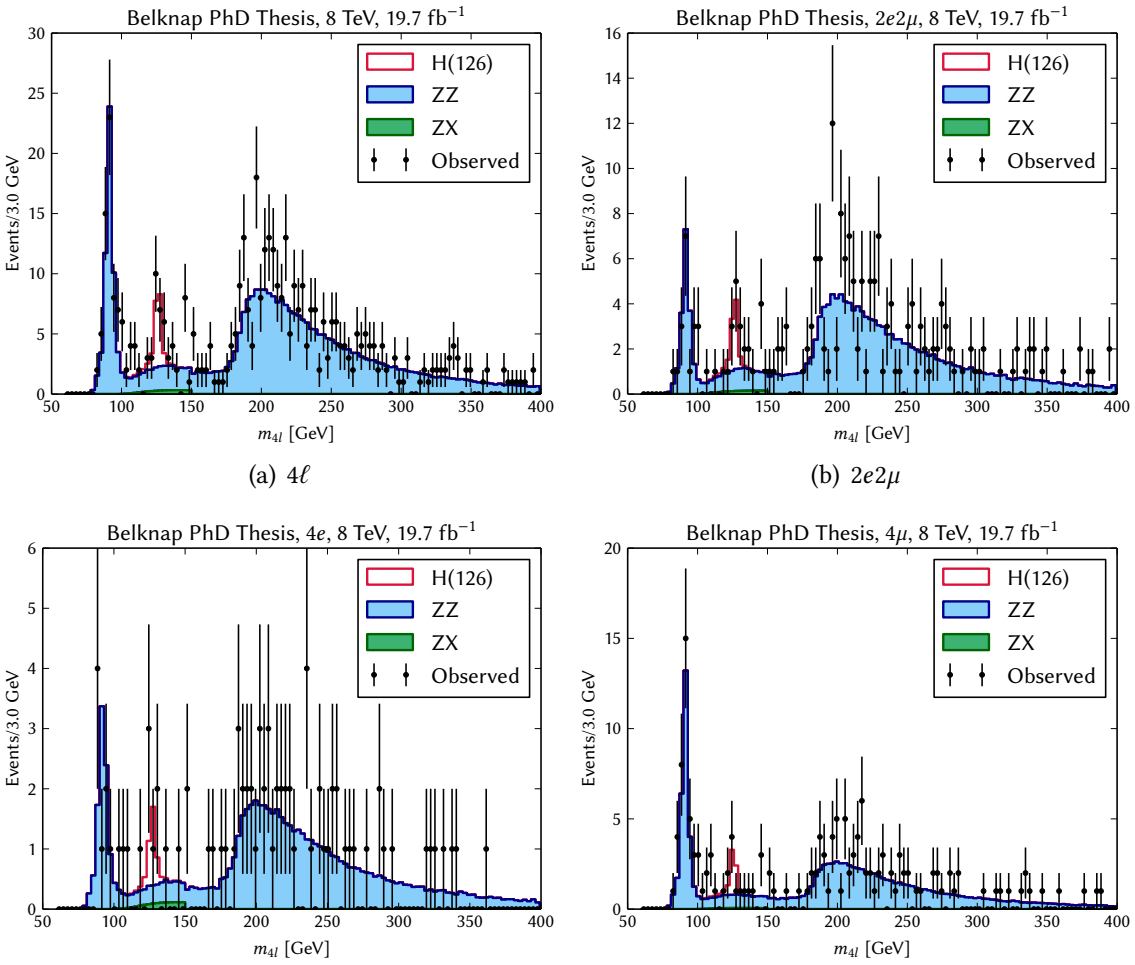

(a) 4ℓ (b) $2e2\mu$

(c) $4e$ (d) 4μ

Figure 7.2: 4ℓ invariant mass distributions, broken down by final state. The combination of all final states in shown in Figure (a). The Standard Model Higgs signal is indicated in red, ZZ background in blue, and $Z + X$ reducible background in green. The data are indicated with black points. The $Z + X$ background is not simulated past 150 GeV.

7.2 Signal, Backgrounds, and Systematics

Signal

At the time this analysis was performed, the latest CMS mass measurement of the Higgs in $H \to ZZ \to 4\ell$ was 126.2 ± 0.6 (stat) ± 0.2 (syst) GeV [23], so the signal Monte Carlo samples were generated assuming a Higgs mass of 126 GeV. Although, the most recent mass measurements are closer to 125 GeV [21], which is still well within the mass window used in this analysis.

The uncertainties in the cross sections are due to uncertainties in the parton distribution function (PDF) plus the strong coupling (α_s), and QCD scaling. They are evaluated using MCFM [71]. The PDF+α_s systematic errors are provided by the LHC working group PDF4LHC [72], which use three sets of PDFs: CT10 [43], MSTW08 [44], and NNPDF [45]. For $q\bar{q}$, the systematic uncertainty is 2.7%; and 7.2% for gg. The QCD scale systematics are found by looking at variations in $d\sigma/dm_{4\ell}$ as the renormalization and factorization scales are moved up and down by a factor of 2. The QCD systematic is 7.5% for gg, and 0.2% for $q\bar{q}$. PDF+α_s also affects the signal acceptance, which evaluates to a 2% systematic error. The uncertainty on the Higgs branching ratio evaluates to 2%, and is provided by the LHC working group [53].

Irreducible Background

The dominant background in this analysis is Standard Model ZZ production, and both $q\bar{q}$ and gg production modes are considered. POWHEG [51] samples are used for $q\bar{q}$ production, and GG2ZZ [52] is used for the gg production mode.

The diboson backgrounds also receive PDF+α_s and QCD scale systematics, and they are computed following the same procedure used for the Higgs signal samples.

Unlike the Higgs samples, they vary with the four-lepton invariant mass. For PDF+α_s, the parameterized systematics are

$$ZZ(q\bar{q}) : \kappa(m_{4\ell}) = 1 + 0.0035\sqrt{m_{4\ell} - 30} \tag{7.3}$$

$$ZZ(gg) : \kappa(m_{4\ell}) = 1 + 0.0066\sqrt{m_{4\ell} - 10} \tag{7.4}$$

and for QCD,

$$ZZ(q\bar{q}) : \kappa(m_{4\ell}) = 1.00 + 0.01\sqrt{(m_{4\ell} - 20)/13} \tag{7.5}$$

$$ZZ(gg) : \kappa(m_{4\ell}) = 1.04 + 0.10\sqrt{(m_{4\ell} - 10)/40} \tag{7.6}$$

For the spin-parity analysis, these are evaluated at 126 GeV, the center of the mass window.

Reducible Background

The reducible background arises from the production of a single Z in association with jets that fake two leptons, which we denote $Z + X$. The Pythia 6.4 $Z + jets$ [48] Monte Carlo are used to model this background. The published CMS results perform a data-driven estimation of this background, which is described elsewhere [73]. For the purposes of this analysis, the Pythia 6.4 Monte Carlo are weighted to reproduce the $Z + X$ yields and four-lepton invariant mass shape from the CMS results. We conservatively assign a 100% systematic to this background.

Additional Systematics and Yields

All Monte Carlo samples (except $Z+X$, which is directly normalized to the expected yields) must be normalized to the integrated luminosity, which has an uncertainty of 2.6% for 8 TeV. The scale factors used for data/MC efficiency corrections have uncertainties which are separated for lepton flavor and final state. All uncertainties, include the efficiency/scale

factor uncertainties, are summarized in Table 7.1. The expected and observed yields are shown in Tables 7.2 and 7.3.

		$gg \to H$	$q\bar{q} \to H$	$q\bar{q} \to ZZ$	$gg \to ZZ$	ZX
Luminosity Norm.	2.6%	•	•	•	•	
μ Efficiency	(4μ) 4.3%	•	•	•	•	
	$(2e2\mu)$ 2.6%	•	•	•	•	
e Efficiency	$(4e)$ 10.1%	•	•	•	•	
	$(2e2\mu)$ 4.6%	•	•	•	•	
Z+Jets Norm.	100%					•
gg PDF		7.2%			7.11%	
$q\bar{q}$ PDF			2.7%	3.43%		
HZZ4L Accept. PDF		2.0%	2.0%			
QCD Scale $gg \to H$		7.5%				
QCD Scale $q\bar{q} \to H$			0.2%			
QCD Scale $gg \to VV$					24.37%	
QCD Scale $q\bar{q} \to VV$				2.86%		
Higgs BR		2.0%	2.0%			

Table 7.1: The systematic errors used in the Spin-Parity analysis. The ZZ systematics are evaluated for a four-lepton invariant mass of 126 GeV. Systematic values that appear on the same row are taken to be 100% correlated.

	4μ	$4e$	$2e2\mu$
$H(126)$	4.5 ± 0.5	2.5 ± 0.4	6.2 ± 0.8
$ZZ(q\bar{q})$	2.1 ± 0.1	0.9 ± 0.1	2.7 ± 0.2
$ZZ(gg)$	0.04 ± 0.01	0.02 ± 0.01	0.05 ± 0.01
$Z + X$	0.2 ± 0.2	0.3 ± 0.3	0.4 ± 0.4
Total	6.8 ± 0.6	3.7 ± 0.5	9.3 ± 0.9
Observed	7	4	10

Table 7.2: The simulated and observed yields within the mass window of $121.5 < m_{4\ell} < 130.5$ GeV. The uncertainties in the yields reflect those listed in Table 7.1.

	4μ	$4e$	$2e2\mu$
$H(126)$	5.4 ± 0.6	3.0 ± 0.5	7.3 ± 0.9
$ZZ(q\bar{q})$	91.5 ± 6.2	60.3 ± 6.8	143.4 ± 10.6
$ZZ(gg)$	5.0 ± 1.3	3.6 ± 1.0	10.3 ± 2.7
$Z + X$	0.8 ± 0.8	1.2 ± 1.2	1.8 ± 1.8
Total	102.7 ± 6.8	68.2 ± 7.7	162.8 ± 11.9
Observed	128	78	202

Table 7.3: The simulated and observed yields within a wider mass window of $100 < m_{4\ell} < 1000$ GeV. The $Z + X$ yields are underestimated in this mass window, since the simulation cuts off at 150 GeV. The uncertainties in the yields reflect those listed in Table 7.1.

7.3 Signal Discrimination

In order to discriminate between the Standard Model pure-scalar hypothesis and the alternate spin parity hypotheses, we define a log-likelihood ratio test statistic

$$q = -2 \ln \left[\frac{\mathcal{L}_{J^P}}{\mathcal{L}_{0^+}} \right] \tag{7.7}$$

The probability distribution functions used to define the likelihood functions are created from the three kinematic angles.

$$f(P_2(\cos\theta_1),\ P_2(\cos\theta_2),\ \cos(2\Phi)) \tag{7.8}$$

The p.d.f.'s are represented as $8 \times 8 \times 8$-bin histogrammed templates, which are populated using signal + background Monte Carlo. The binning was chosen to ensure sufficient statistics in the template bins. A separate template is created for each signal hypothesis. The 1D distributions of the angles comparing Standard Model and alternate hypotheses are shown in Figures 7.3-7.5.

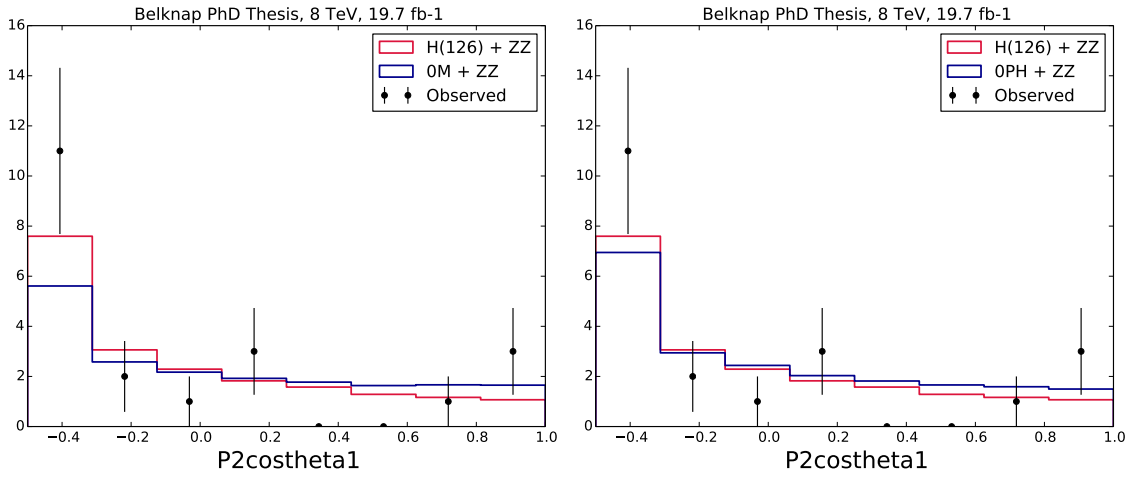

(a) 0^- (b) 0_h^+

(c) $2_m^+(gg)$ (d) $2_m^+(q\bar{q})$

FIGURE 7.3: Distributions of $P_2(\cos\theta_1)$. The Standard Model plus background is shown in red, and the alternate spin-parity hypothesis plus background is shown in blue. The data are shown as black points.

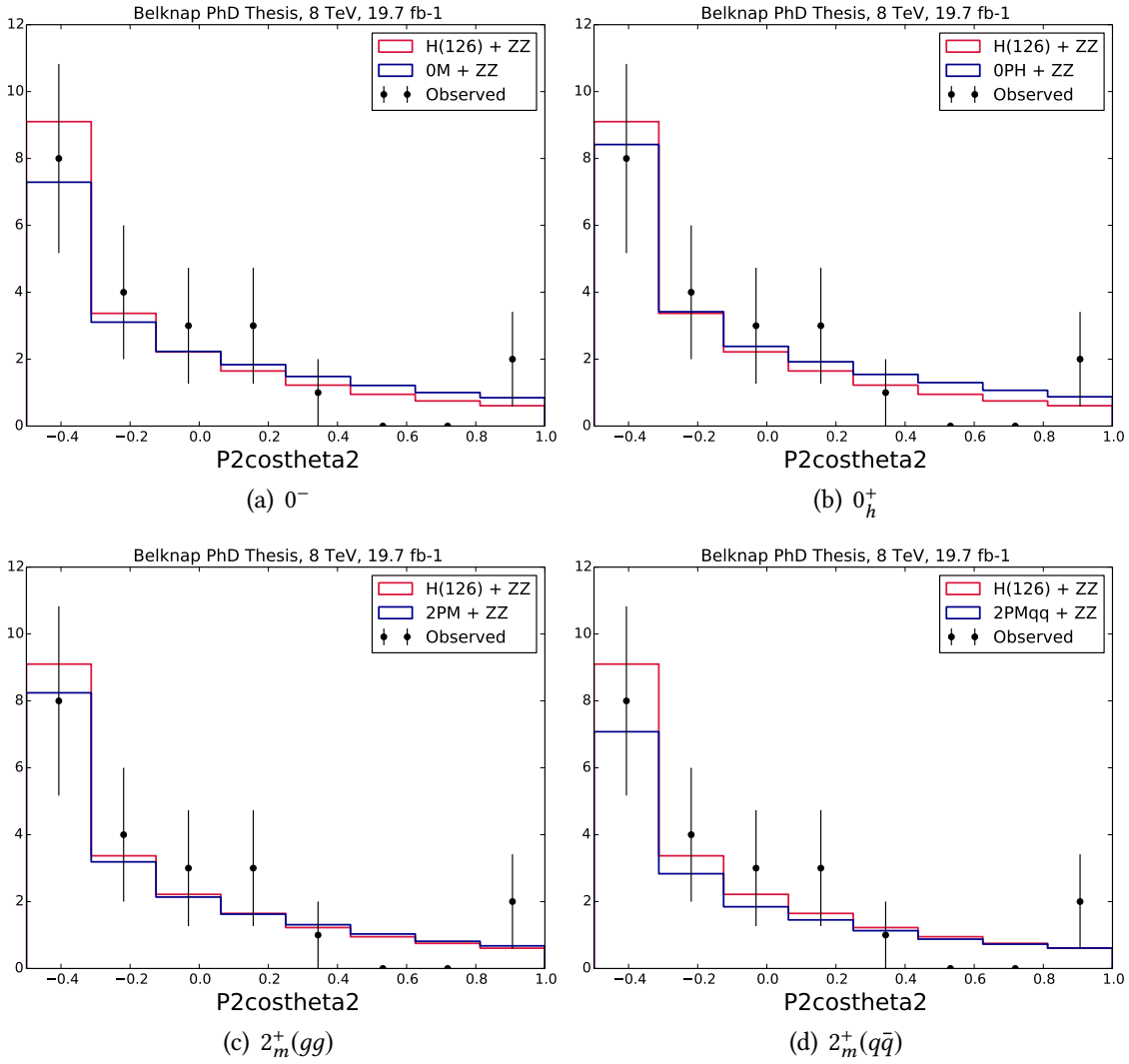

(a) 0^- (b) 0_h^+

(c) $2_m^+(gg)$ (d) $2_m^+(q\bar{q})$

FIGURE 7.4: Distributions of $P_2(\cos\theta_2)$. The Standard Model plus background is shown in red, and the alternate spin-parity hypothesis plus background is shown in blue. The data are shown as black points.

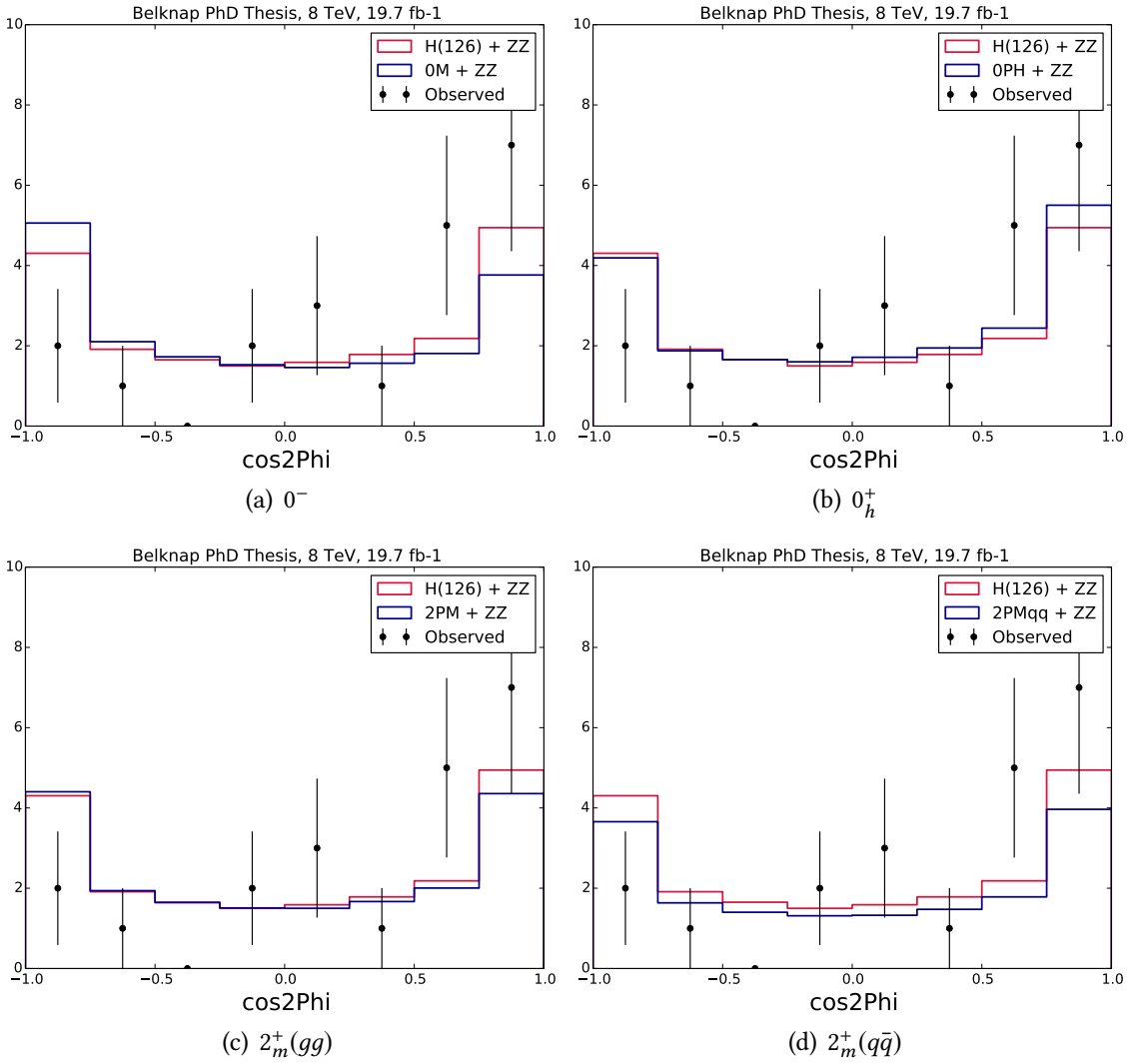

(a) 0^- (b) 0^+_h

(c) $2^+_m(gg)$ (d) $2^+_m(q\bar{q})$

FIGURE 7.5: Distributions of cos(2Φ). The Standard Model plus background is shown in red, and the alternate spin-parity hypothesis plus background is shown in blue. The data are shown as black points.

Before q is computed, the signal strength, μ, is fit to the data to maximize each likelihood function separately. The next step is determining the distributions of q for the Standard Model and alternate hypotheses. 50 000 Monte Carlo simulated "toy" events are generated from the templates for the Standard Model and the alternate hypothesis separately, taking the systematic uncertainties into account. Finally, we compute the value of q corresponding to the data. Comparing this with the distributions of q for the two signal hypotheses, we can measure how strongly the data prefers one hypothesis over the other.

The distributions of q, and the measured value of q are shown in Figure 7.6. The numerical values for the expected hypothesis separation, the separation between the observed value of q and the expectation for the two hypotheses, and the CL_s values are given in Table 7.4. The data are consistent with the Standard Model expectation, excluding the 0^- pseudoscalar hypothesis at the 95% confidence level.

The published CMS analysis [22] utilizes a much more sophisticated method, as they use the full set of kinematic information to discriminate between the signal hypotheses and the backgrounds. They were able to exclude the pseudoscalar at 99% CL, the spin-2 hypotheses at 95% CL, and 0_h^+ at 90% CL. The analysis presented in this thesis is much simpler and more straightforward, as it utilizes only information of the angles to discriminate between signal hypotheses. The cost of the improved simplicity is a decrease in discrimination power. This method was unable to effectively discriminate between 0_h^+ and $2_m^+(q\bar{q})$, as their CL_s values were near 50%. However, the results are consistent with those of the published CMS analysis, and an angles-only approach is capable of excluding the pseudoscalar hypothesis at 95% CL.

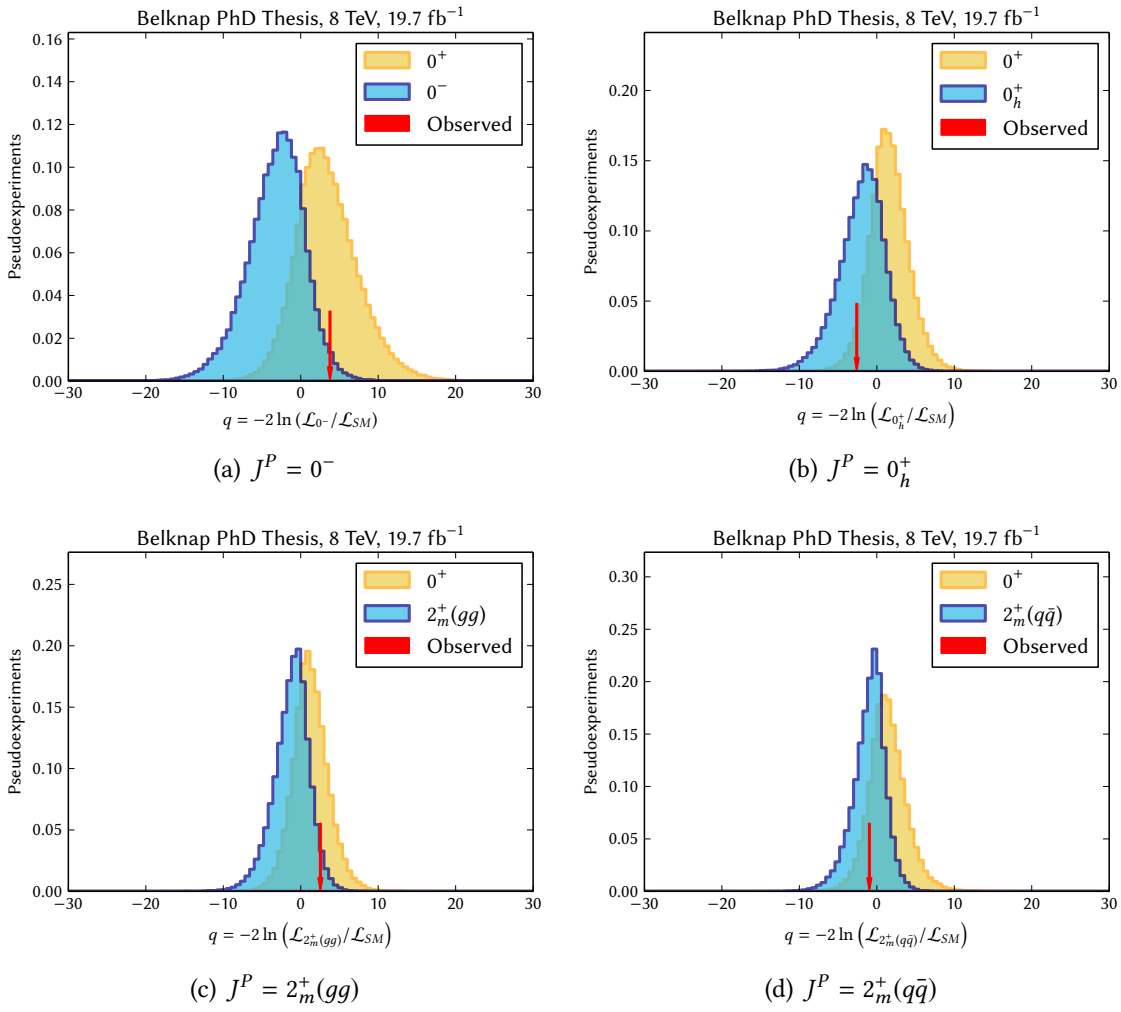

(a) $J^P = 0^-$ (b) $J^P = 0_h^+$

(c) $J^P = 2_m^+(gg)$ (d) $J^P = 2_m^+(q\bar{q})$

FIGURE 7.6: The test statistic $q = -2\ln\left(\mathcal{L}_{JP}/\mathcal{L}_{SM}\right)$ is shown for SM 0^+ (yellow), and the alternate J^P hypothesis (blue). The expected distributions are created by generating a total of 100 000 Monte Carlo toys assuming $m_H = 126$ GeV. The value observed from CMS data is indicated by the red arrow.

J^P	Expected Sep. (σ)	P (SM < Obs) (σ)	$P\left(J^P > \text{Obs}\right)$ (σ)	CL_s	CL_s (σ)	q_{obs}
0^-	1.83	−0.17	2.04	0.05	1.67	3.78
0^+_h	1.33	1.73	−0.30	0.65	−0.37	−2.59
$2^+_m(gg)$	1.11	−0.62	1.77	0.14	1.06	2.54
$2^+_m(q\bar{q})$	1.10	1.08	−0.11	0.63	−0.33	−0.96

Table 7.4: The expected and observed separation between SM and alternate hypotheses. The expected separation is calculated with a signal strength calculated from data, and is computed for a value of q such that $P(SM < q) = P(J^P > q)$. CL_s is defined to be $P(J^P > \text{Obs})/P(\text{SM} > \text{Obs})$.

8 Search for a Doubly Charged Higgs

A possible extension to the Standard Model particle spectrum is a Higgs triplet (Φ^0, Φ^+, Φ^{++}) with $SU(2)_L \times U(1)_Y$ quantum numbers (3, 2). The model is a Type II "seesaw" mechanism that offers a means for neutrinos to gain their mass, which we know to be very small, but certainly greater than zero. This search for the doubly charged component of the Higgs triplet looks for the pair production of two doubly charged bosons,

$$q\bar{q} \to Z/\gamma^* \to \Phi^{++}\Phi^{--} \to \ell_i^+\ell_j^+\ell_k^-\ell_l^- \tag{8.1}$$

where the bosons decay to same-sign lepton pairs. The leptons are not necessarily of the same flavor.

CMS previously performed a search for a doubly charged Higgs boson using 4.9 fb^{-1} of 7 TeV data [37]. This analysis presented here is performed using 19.7 fb^{-1} of 8 TeV data. As described in Chapter 1, the branching ratios of the doubly charged Higgs are not determined by the model. Therefore, we search for different trial configurations of branching ratios. Namely, we search for cases where the boson decays 100% to ee, $\mu\mu$, and $e\mu$, as well as those listed in Table 1.4, reproduced here:

Benchmark Point	ee	$e\mu$	$e\tau$	$\mu\mu$	$\mu\tau$	$\tau\tau$
BP1	0	0.01	0.01	0.30	0.38	0.30
BP2	1/2	0	0	1/8	1/4	1/8
BP3	1/3	0	0	1/3	0	1/3
BP4	1/6	1/6	1/6	1/6	1/6	1/6

The 7 TeV CMS analysis includes tau final states, however the 8 TeV analysis is performed using only muons and electrons. The strategy is to scan over different hypothesized masses of the doubly charged Higgs boson, and compute an upper limit on the signal strength: $\sigma_{\text{observed}}/\sigma_{\text{SM}+\Phi^{++}}$. This is done for each of the different branching ratio scenarios.

8.1 Event Reconstruction and Selection

The analysis begins with electrons and muons following the selections outlined in Chapter 6. Both this analysis and $H \to ZZ \to 4\ell$ look for a four-lepton final state. However, the topology of the Φ^{++} final state is rather different. We apply the following sequence of selections:

- Trigger threshold:

$$p_T^{\text{leading}} > 20.0\,\text{GeV} \text{ and } p_T^{\text{sub-leading}} > 10.0\,\text{GeV}$$

- Apply isolation to all leptons: $I_{rel}^{pf} < 0.4$
- Require that all pairs of leptons, regardless of charge or flavor, have an invariant mass greater than 12.0 GeV for QCD suppression
- Form same-sign pairs of leptons: $++$ and $--$
- If there are more than four leptons, select the combination where $|m_{\ell^+\ell^+} - m_{\ell^-\ell^-}|$ is minimized

Since we are looking at different trial masses, $m_{\Phi^{++}}$, of the doubly charged Higgs, we apply mass-dependent selections as well:

- Require that the scalar sum of the p_T of the leptons is $s_T > (0.6 \cdot m_{\Phi^{++}} + 130\,\text{GeV})$

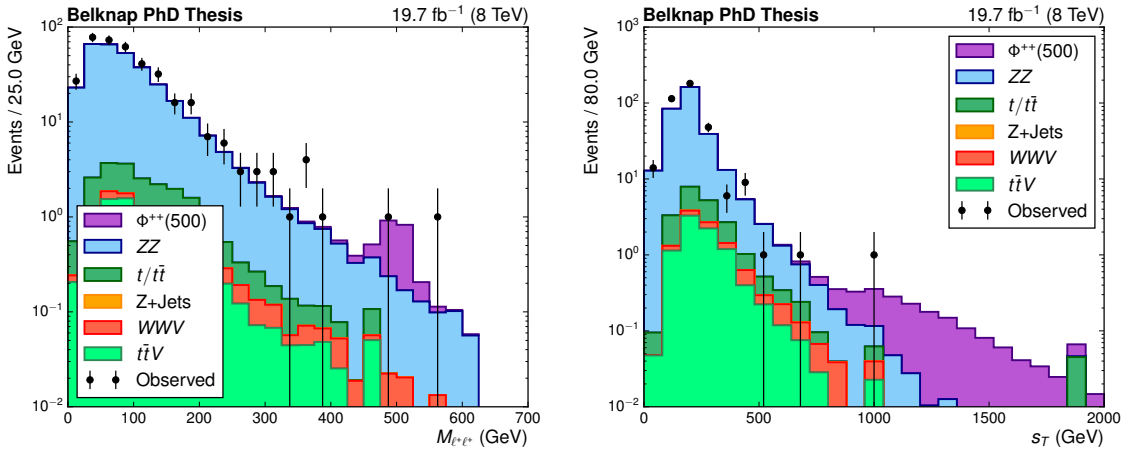

(a) $m_{\ell^+\ell^+}$ (b) s_T

FIGURE 8.1: Distributions of $m_{\ell^+\ell^+}$ and s_T for a mass hypothesis of $m_{\Phi^{++}} = 500\,\text{GeV}$ are shown. These are shown after the 4ℓ event has been selected, but before any mass-dependent selections are made.

- Apply a mass window of

$$0.9 \cdot m_{\Phi^{++}} < m_{\ell^+\ell^+} < 1.1 \cdot m_{\Phi^{++}}$$

$$0.9 \cdot m_{\Phi^{++}} < m_{\ell^-\ell^-} < 1.1 \cdot m_{\Phi^{++}}$$

Distributions of $m_{\ell^+\ell^+}$ and s_T for a mass hypothesis of $m_{\Phi}^{++} = 500\,\text{GeV}$ are shown in Figure 8.1.

8.2 Signal

The signal Monte Carlo samples are generated using PYTHIA 6.4 for the following trial mass points: 110, 130, 150, 170, 200, 250, 300, 350, 400, 450, 500, 600, and 700 GeV. The $\ell^+\ell^+$ invariant mass shapes of the different mass points are shown in Figure 8.2.

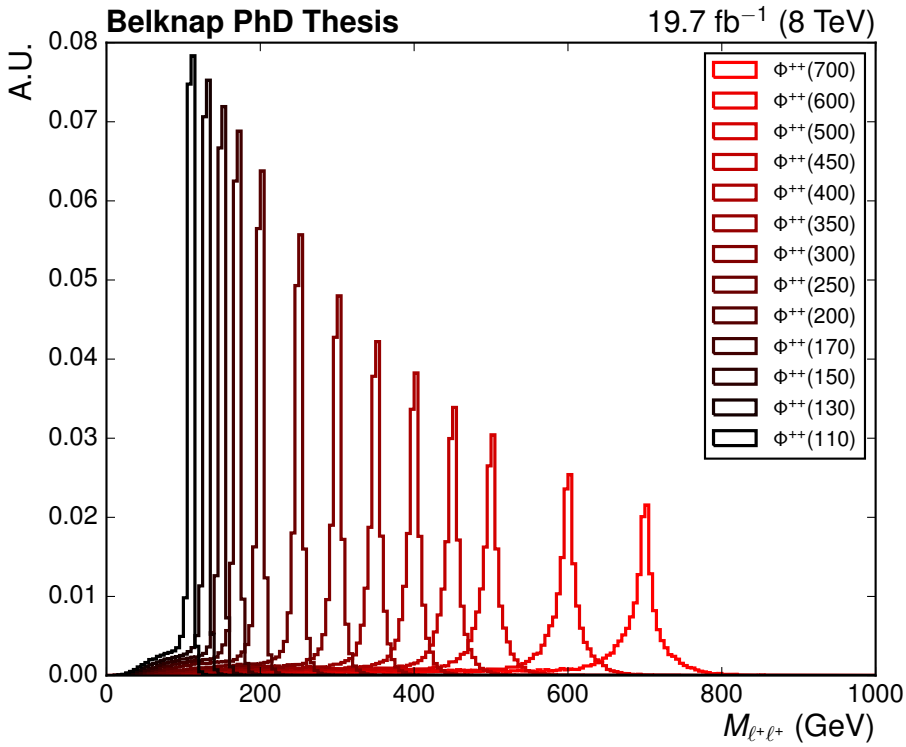

FIGURE 8.2: The $\ell^+\ell^+$ invariant mass spectrum of the different doubly charged Higgs trial masses are shown here. The shapes are normalized to unit area, and not their cross sections.

8.3 Check With SM Higgs and Diboson

To verify that the initially selected leptons were modeled properly, we reproduced the $H \to ZZ \to 4\ell$ selections. Both the doubly charged Higgs selections and this SM Higgs check were performed from the same set of data files. There are a few differences in the selections. The p_T requirement on electrons are lowered from 15 GeV to 7 GeV, the QCD suppression cut is performed using opposite-sign leptons. Other than this, the isolation and identification selections are the same. The selections used for this check are as follows:

- Trigger threshold:

$$p_T^{\text{leading}} > 20.0\,\text{GeV} \text{ and } p_T^{\text{sub-leading}} > 10.0\,\text{GeV}$$

- Require that all opposite-sign leptons have an invariant mass > 4 GeV to suppress QCD
- Apply an isolation requirement of $I_{rel}^{pf} < 0.4$ to all leptons
- Select the opposite-sign same-flavor (OSSF) pair with an invariant mass closest to m_{Z_0} as Z_1
- Of the remaining leptons, select the OSSF pair with the highest scalar p_T sum as Z_2
- Require $40 < m_{Z_1} < 120$ GeV and $12 < m_{Z_2} < 120$ GeV

POWHEG [51] and GG2ZZ [52] Monte Carlo samples were used to model ZZ, and POWHEG Monte Carlo samples were used for $gg \to H \to 4\ell$. We assume a Higgs mass of 125 GeV. The invariant mass plots broken down by channel are shown in Figure 8.3, and they show good agreement between Monte Carlo and data.

8.4 Backgrounds

In the final analysis, we use a data-driven method to estimate the backgrounds. Monte Carlo is still needed to perform the estimate, so we verify the effectiveness of the Monte Carlo by looking at control regions for diboson, single and double top backgrounds. The control regions begin with the selections outlined in the previous section, but they include modifications to enhance the contribution of the process of interest (e.g. ZZ and $t/t\bar{t}$). The mass window and mass-dependent s_T selections are not used in the control regions.

Diboson

Standard Model ZZ is the dominant background in the analysis. POWHEG and GG2ZZ Monte Carlo samples are used to model it. We also include MADGRAPH 4 [50] $Z + jets$,

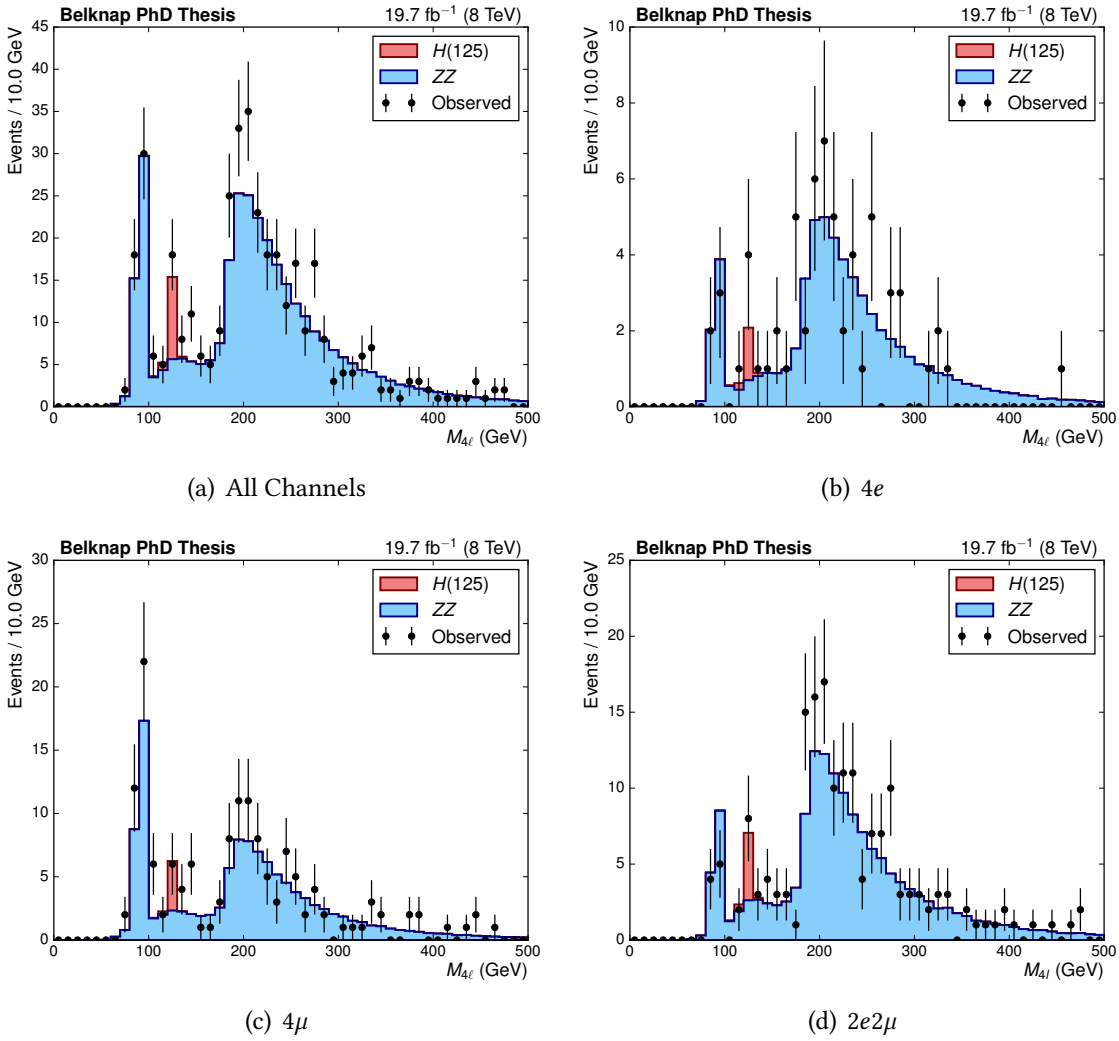

(a) All Channels

(b) $4e$

(c) 4μ

(d) $2e2\mu$

FIGURE 8.3: We use the $H \to ZZ \to 4\ell$ selections as an initial check that the leptons are modeled properly. These are produced from the same n-tuples as the rest of the doubly charged Higgs analysis. They show good agreement between data and simulation.

POWHEG single top, and MADGRAPH 4 double top samples as background to ZZ. This control region is performed using the Φ^{++} topology as described in Section 8.1. We make the following modifications to the base Φ^{++} selections:

- Z-tag: require at least one opposite-sign same-flavor lepton pair where $|m_{\ell^+\ell^-} - m_{Z_0}| <$ 20.0 GeV

- Require $s_T > 150.0\,\text{GeV}$

Histograms of $m_{\ell^+\ell^+}$ and s_T for this control region are shown in Figure 8.4, and show good agreement between Monte Carlo and data.

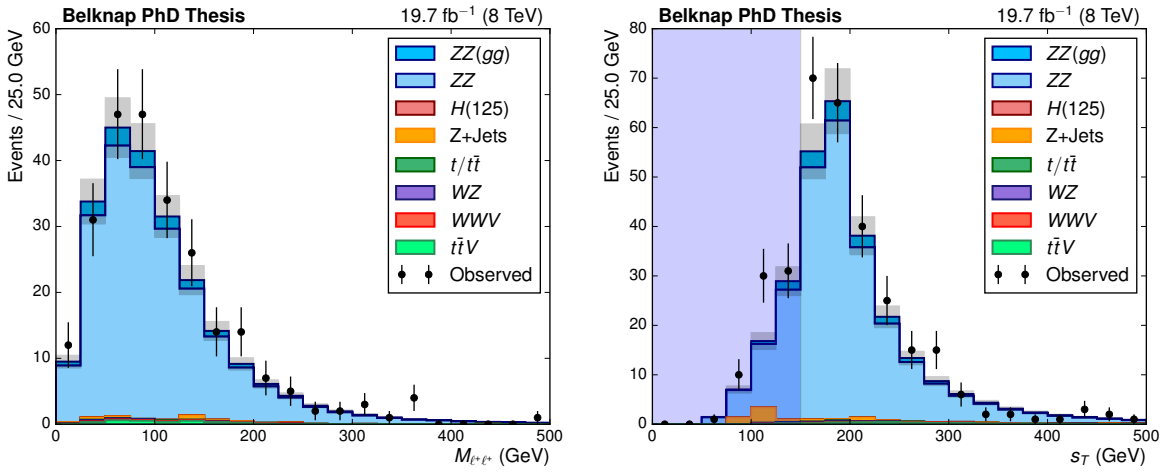

(a) $m_{\ell^+\ell^+}$ (b) s_T

Figure 8.4: $\ell^+\ell^+$ invariant mass and s_T shapes for the ZZ control region. This control region is constructed using Φ^{++} topology rather than $H \to ZZ \to 4\ell$. The gray shaded bands indicate a 10% uncertainty on the Monte Carlo, and the blue shaded region indicates the $s_T > 150\,\text{GeV}$ requirement. The data and Monte Carlo show good agreement.

Single and Double Top

The single top background is modeled using POWHEG, which generates the hard scattering before including the parton shower, and is good for low-multiplicity final states. Double top is modeled using MADGRAPH 4, which is suitable for modeling high-multiplicity final states. We also include $Z + jets$, WZ, WWV, and $t\bar{t}V$ as backgrounds for this control region. This control region uses the base selections with the following modifications:

- The two leptons with the lowest isolation values have $I_{rel}^{pf} < 0.4$, and the two with the highest isolation values have $I_{rel}^{pf} > 0.4$

- Z-Veto: for all opposite-sign same-flavor lepton pairs, require $|m_{\ell^+\ell^-} - m_{Z_0}| > 20.0\,\text{GeV}$
- $s_T > 150\,\text{GeV}$ and $\not{E}_T > 30\,\text{GeV}$

Histograms of $m_{\ell^+\ell^+}$ and s_T for this control region are shown in Figure 8.5, and show reasonable agreement between Monte Carlo and data.

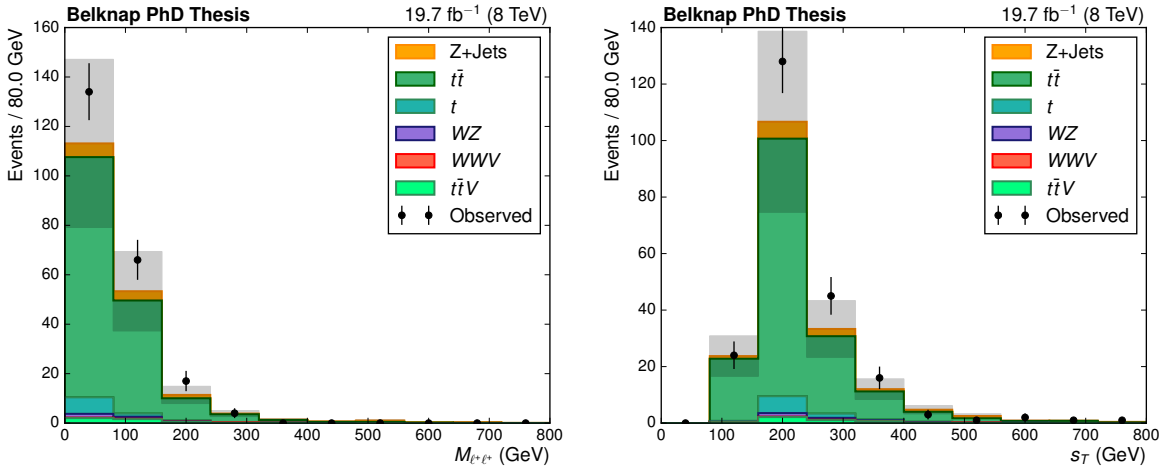

(a) $m_{\ell^+\ell^+}$ (b) s_T

FIGURE 8.5: $\ell^+\ell^+$ invariant mass and s_T shapes for the $t/t\bar{t}$ control region. The shaded bands indicate a 30% uncertainty on the Monte Carlo. The data and Monte Carlo show good agreement.

8.5 Background Estimation

The contribution of the background to the signal region is estimated using a *sideband* method. The signal region is defined in the 2D mass window $(0.9 \cdot m_\Phi^{++},\ 1.1 \cdot m_\Phi^{++})$ for both $m_{\ell^+\ell^+}$ and $m_{\ell^-\ell^-}$. The sideband is defined between $12 < m_{\ell^+\ell^+/\ell^-\ell^-} < 700\,\text{GeV}$, excluding the signal region.

For each hypothesized doubly charged Higgs mass, we compute the ratio, α, of the number of background events in the signal region to the background events in the

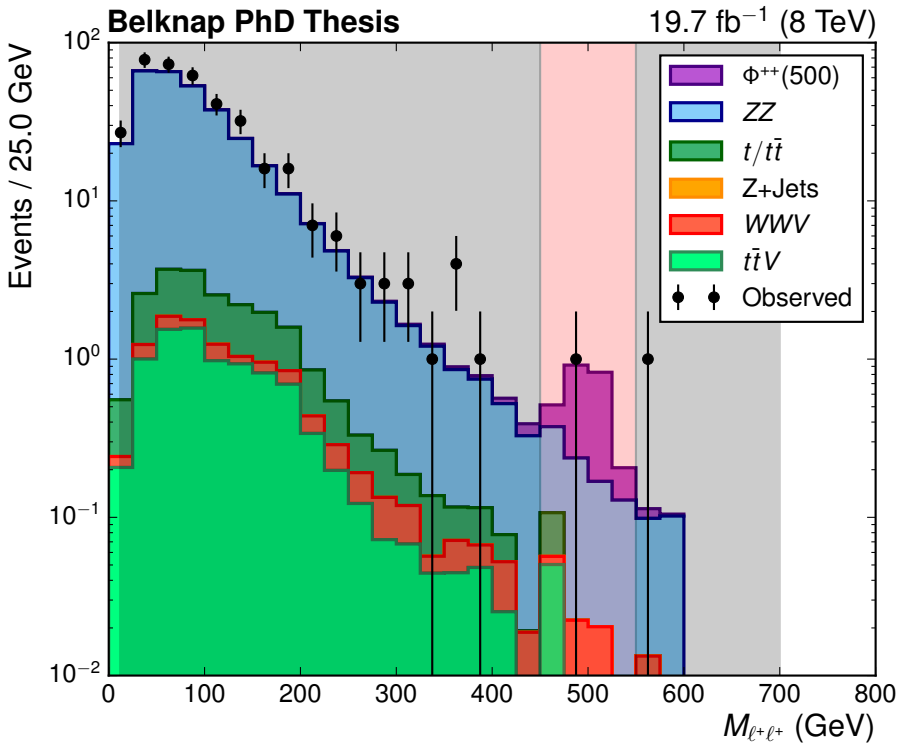

Figure 8.6: The sideband is shown in gray and the signal region is shown in red for the 500 GeV mass point. The signal region is defined in a 2D window of $[0.9 \cdot m_{\Phi^{++}},\ 1.1 \cdot m_{\Phi^{++}}]$ in the $m_{\ell^+\ell^+}$-$m_{\ell^-\ell^-}$ plane. The sidebands are defined in the same 2D plane from 12 to 700 GeV, excluding the signal region.

sidebands using Monte Carlo simulation.

$$\alpha = \frac{N_{SR}}{N_{SB}} \tag{8.2}$$

In the event of low Monte Carlo statistics, we made the following modifications:

- If $N_{SB} = 0$, then $\alpha = N_{SR}$
- If N_{SR} is less than the Monte Carlo statistical uncertainty, the statistical uncertainty is used as α

To estimate the number of background events in the signal region, we obtain the number of events from data that appear in the sideband region for a given mass-point,

N_{SB}^{data}. Together with α, the number of estimated background events in the signal region is

$$N_{BGSR} = \alpha \cdot \left(N_{SB}^{data} + 1\right) \tag{8.3}$$

with relative error $1/\sqrt{N_{SB}^{data} + 1}$. This event rate is modeled using a Gamma distribution with mean $\left(N_{SB}^{data} + 1\right)$, and dispersion $\sqrt{N_{SB}^{data} + 1}$. For each branching ratio scenario and mass point, background estimates computed from Monte Carlo and the sideband method, expected signal yields, and observed events are given in Tables 8.1-8.7. These include the mass-dependent requirements on $m_{\ell^+\ell^+}$, $m_{\ell^-\ell^-}$, and s_T. The uncertainties given on the sideband background estimate reflect the dispersion of the Gamma distribution. The uncertainties for the Monte Carlo estimate reflect Monte Carlo statistical uncertainty.

Mass (GeV)	MC Estimate	Sideband Estimate	Observation	Signal
110	0.3880 ± 0.0169	0.2451 ± 0.0594	0	2310.33 ± 347.17
130	0.2801 ± 0.0146	0.1233 ± 0.0330	0	1409.83 ± 211.80
150	0.1883 ± 0.0119	0.0617 ± 0.0195	1	864.08 ± 129.95
170	0.1229 ± 0.0095	0.0397 ± 0.0126	0	564.17 ± 84.89
200	0.1012 ± 0.0252	0.0212 ± 0.0075	0	297.86 ± 44.81
250	0.0434 ± 0.0054	0.0079 ± 0.0030	0	125.95 ± 18.96
300	0.0180 ± 0.0030	0.0020 ± 0.0010	0	56.63 ± 8.54
350	0.0070 ± 0.0017	0.0006 ± 0.0004	0	27.73 ± 4.18
400	0.0089 ± 0.0022	0.0006 ± 0.0004	0	14.30 ± 2.16
450	0.0034 ± 0.0015	0.0003 ± 0.0002	0	7.83 ± 1.18
500	0.0030 ± 0.0012	0.0001 ± 0.0001	0	4.40 ± 0.67
600	0.0003 ± 0.0003	0.0000 ± 0.0000	0	1.51 ± 0.23
700	0.0000 ± 0.0000	0.0010 ± 0.0010	0	0.54 ± 0.08

Table 8.1: Background, signal, and observed yields assuming a doubly charged Higgs branching ratio of 100% electrons. Background yields estimated from Monte Carlo (MC) and the data-driven method (Sideband) are shown.

Mass (GeV)	MC Estimate	Sideband Estimate	Observation	Signal
110	1.0030 ± 0.0427	0.8241 ± 0.1030	4	2883.88 ± 433.22
130	0.7045 ± 0.0391	0.4024 ± 0.0563	3	1663.39 ± 249.85
150	0.5044 ± 0.0389	0.2322 ± 0.0363	1	1006.03 ± 151.25
170	0.3090 ± 0.0236	0.1336 ± 0.0217	1	658.43 ± 99.03
200	0.2099 ± 0.0203	0.0555 ± 0.0103	0	348.68 ± 52.44
250	0.1051 ± 0.0143	0.0175 ± 0.0039	0	143.91 ± 21.66
300	0.0405 ± 0.0074	0.0054 ± 0.0014	0	63.74 ± 9.61
350	0.0287 ± 0.0066	0.0022 ± 0.0007	0	30.58 ± 4.61
400	0.0215 ± 0.0060	0.0015 ± 0.0005	0	15.92 ± 2.40
450	0.0063 ± 0.0028	0.0004 ± 0.0001	0	8.72 ± 1.32
500	0.0053 ± 0.0024	0.0003 ± 0.0001	0	4.71 ± 0.71
600	0.0000 ± 0.0000	0.0000 ± 0.0000	0	1.71 ± 0.26
700	0.0000 ± 0.0000	0.0030 ± 0.0018	0	0.60 ± 0.09

Table 8.2: Background, signal, and observed yields assuming a doubly charged Higgs branching ratio of 100% electron-muon pairs. Background yields estimated from Monte Carlo (MC) and the data-driven method (Sideband) are shown.

Mass (GeV)	MC Estimate	Sideband Estimate	Observation	Signal
110	0.5752 ± 0.0326	0.4420 ± 0.0674	1	3654.25 ± 548.80
130	0.4462 ± 0.0194	0.2564 ± 0.0405	0	2101.44 ± 315.56
150	0.3604 ± 0.0385	0.1425 ± 0.0256	0	1257.68 ± 189.01
170	0.2408 ± 0.0285	0.0756 ± 0.0151	0	780.29 ± 117.32
200	0.1133 ± 0.0092	0.0268 ± 0.0065	1	415.99 ± 62.54
250	0.0583 ± 0.0064	0.0094 ± 0.0026	0	166.86 ± 25.10
300	0.0339 ± 0.0052	0.0025 ± 0.0010	0	74.05 ± 11.16
350	0.0208 ± 0.0039	0.0011 ± 0.0005	0	36.02 ± 5.43
400	0.0098 ± 0.0023	0.0003 ± 0.0002	0	18.09 ± 2.73
450	0.0048 ± 0.0013	0.0001 ± 0.0001	0	9.68 ± 1.46
500	0.0026 ± 0.0013	0.0001 ± 0.0001	0	5.54 ± 0.84
600	0.0018 ± 0.0009	0.0000 ± 0.0000	0	1.76 ± 0.27
700	0.0024 ± 0.0017	0.0000 ± 0.0000	0	0.64 ± 0.10

Table 8.3: Background, signal, and observed yields assuming a doubly charged Higgs branching ratio of 100% muons. Background yields estimated from Monte Carlo (MC) and the data-driven method (Sideband) are shown.

Mass (GeV)	MC Estimate	Sideband Estimate	Observation	Signal
110	1.6169 ± 0.0558	1.3330 ± 0.1256	5	348.43 ± 49.43
130	1.1845 ± 0.0482	0.6974 ± 0.0716	3	200.49 ± 28.43
150	0.8911 ± 0.0592	0.3969 ± 0.0460	1	120.11 ± 17.03
170	0.6389 ± 0.0545	0.2772 ± 0.0412	1	74.60 ± 10.57
200	0.3744 ± 0.0405	0.1184 ± 0.0202	1	39.76 ± 5.63
250	0.1638 ± 0.0157	0.0292 ± 0.0049	0	15.96 ± 2.26
300	0.0746 ± 0.0090	0.0110 ± 0.0025	0	7.08 ± 1.01
350	0.0495 ± 0.0077	0.0056 ± 0.0017	0	3.44 ± 0.49
400	0.0313 ± 0.0064	0.0049 ± 0.0018	0	1.73 ± 0.25
450	0.0113 ± 0.0031	0.0016 ± 0.0010	0	0.93 ± 0.13
500	0.0080 ± 0.0027	0.0034 ± 0.0018	0	0.53 ± 0.08
600	0.0018 ± 0.0009	0.0021 ± 0.0014	0	0.17 ± 0.02
700	0.0024 ± 0.0017	0.0051 ± 0.0023	0	0.06 ± 0.01

Table 8.4: Background, signal, and observed yields assuming a doubly charged Higgs with BP1 branching ratios. Background yields estimated from Monte Carlo (MC) and the data-driven method (Sideband) are shown.

Mass (GeV)	MC Estimate	Sideband Estimate	Observation	Signal
110	0.9635 ± 0.0367	0.6900 ± 0.0899	1	1001.37 ± 95.52
130	0.7268 ± 0.0242	0.3825 ± 0.0523	0	598.28 ± 57.79
150	0.5488 ± 0.0403	0.2063 ± 0.0322	1	364.45 ± 35.38
170	0.3643 ± 0.0300	0.1213 ± 0.0203	0	235.59 ± 23.03
200	0.2145 ± 0.0268	0.0500 ± 0.0100	1	125.43 ± 12.20
250	0.1017 ± 0.0084	0.0193 ± 0.0042	0	52.00 ± 5.12
300	0.0518 ± 0.0060	0.0066 ± 0.0020	0	23.29 ± 2.31
350	0.0278 ± 0.0043	0.0038 ± 0.0016	0	11.46 ± 1.13
400	0.0187 ± 0.0032	0.0030 ± 0.0015	0	5.88 ± 0.58
450	0.0082 ± 0.0020	0.0024 ± 0.0014	0	3.21 ± 0.32
500	0.0056 ± 0.0018	0.0022 ± 0.0014	0	1.79 ± 0.18
600	0.0020 ± 0.0009	0.0020 ± 0.0014	0	0.61 ± 0.06
700	0.0024 ± 0.0017	0.0031 ± 0.0018	0	0.22 ± 0.02

Table 8.5: Background, signal, and observed yields assuming a doubly charged Higgs with BP2 branching ratios. Background yields estimated from Monte Carlo (MC) and the data-driven method (Sideband) are shown.

Mass (GeV)	MC Estimate	Sideband Estimate	Observation	Signal
110	0.9635 ± 0.0367	0.6900 ± 0.0899	1	1323.30 ± 100.36
130	0.7268 ± 0.0242	0.3825 ± 0.0523	0	774.18 ± 58.56
150	0.5488 ± 0.0403	0.2063 ± 0.0322	1	468.03 ± 35.40
170	0.3643 ± 0.0300	0.1213 ± 0.0203	0	298.04 ± 22.51
200	0.2145 ± 0.0268	0.0500 ± 0.0100	1	159.56 ± 12.05
250	0.1017 ± 0.0084	0.0193 ± 0.0042	0	64.88 ± 4.90
300	0.0518 ± 0.0060	0.0066 ± 0.0020	0	28.93 ± 2.19
350	0.0278 ± 0.0043	0.0038 ± 0.0016	0	14.24 ± 1.08
400	0.0187 ± 0.0032	0.0030 ± 0.0015	0	7.26 ± 0.55
450	0.0082 ± 0.0020	0.0024 ± 0.0014	0	3.93 ± 0.30
500	0.0056 ± 0.0018	0.0022 ± 0.0014	0	2.20 ± 0.17
600	0.0020 ± 0.0009	0.0020 ± 0.0014	0	0.73 ± 0.06
700	0.0024 ± 0.0017	0.0031 ± 0.0018	0	0.27 ± 0.02

Table 8.6: Background, signal, and observed yields assuming a doubly charged Higgs with BP3 branching ratios. Background yields estimated from Monte Carlo (MC) and the data-driven method (Sideband) are shown.

Mass (GeV)	MC Estimate	Sideband Estimate	Observation	Signal
110	2.0053 ± 0.0583	1.5810 ± 0.1390	5	587.13 ± 33.60
130	1.4650 ± 0.0503	0.8235 ± 0.0788	3	342.05 ± 19.54
150	1.0794 ± 0.0604	0.4606 ± 0.0500	2	207.22 ± 11.84
170	0.7624 ± 0.0553	0.3229 ± 0.0433	1	132.13 ± 7.54
200	0.4756 ± 0.0477	0.1417 ± 0.0216	1	70.43 ± 4.02
250	0.2072 ± 0.0166	0.0391 ± 0.0059	0	28.69 ± 1.64
300	0.0925 ± 0.0095	0.0151 ± 0.0030	0	12.73 ± 0.73
350	0.0565 ± 0.0079	0.0082 ± 0.0023	0	6.24 ± 0.36
400	0.0402 ± 0.0068	0.0076 ± 0.0024	0	3.19 ± 0.18
450	0.0147 ± 0.0035	0.0039 ± 0.0018	0	1.71 ± 0.10
500	0.0110 ± 0.0030	0.0055 ± 0.0023	0	0.95 ± 0.05
600	0.0020 ± 0.0009	0.0041 ± 0.0020	0	0.32 ± 0.02
700	0.0024 ± 0.0017	0.0081 ± 0.0029	0	0.12 ± 0.01

Table 8.7: Background, signal, and observed yields assuming a doubly charged Higgs with BP4 branching ratios. Background yields estimated from Monte Carlo (MC) and the data-driven method (Sideband) are shown.

8.6 Systematic Uncertainties

Three global systematic uncertainties are assigned to all final states and branching ratio scenarios. The first is the uncertainty on the integrated luminosity for the 8 TeV dataset, which is estimated to be 2.6%. The second is the uncertainty on the signal cross section, which is 15% for all mass points. The third is the uncertainty on the ratio, α, used in the sideband method, which we estimate to be 10%.

The lepton efficiency systematics are computed by increasing the lepton scale factor by 1σ, and computing the change in yield of the signal Monte Carlo for $m_{\Phi^{++}} = 110\,\text{GeV}$. The lepton scale factors are stored in lookup tables, which are defined up to a p_T of 100 GeV for muons, and 200 GeV for electrons. If a lepton was outside the bounds of the lookup table, the scale factor was set to 1.0, and the uncertainty was set to 2% for electrons, and 0.5% for muons. The systematics are summarized in Table 8.8.

The analysis is also subject to non-constant systematic uncertainties. These arise from the statistical uncertainty associated with the number of data events used in the sideband method. This systematic can be as large as 100% if no data events are observed in the sidebands.

8.7 Exclusion Limits

To search for the doubly charged Higgs, we compute the 95% upper limit on the signal strength for each of the different hypothesized masses [74]. The analysis is a simple unbinned counting experiment, where the number of expected events for a given mass point is given by

$$E = \mu \cdot s + b \tag{8.4}$$

Systematic Category		Systematic
Luminosity		2.6%
Signal Cross Section		15%
Sideband Method Ratio (α)		10%
Leptons in Final State	**Muon Systematic**	**Electron Systematic**
4μ	1.0%	-
$4e$	-	6.6%
$2e + 2\mu$	0.5%	3.2%
$3e + 1\mu$	0.2%	4.7%
$1e + 3\mu$	0.7%	1.6%

TABLE 8.8: The systematic uncertainties are quoted as relative errors. The lepton systematics reflect the uncertainties in the data/MC efficiency correction factors. These systematics are applied to all branching ratio scenarios. The statistical uncertainties associated with the sideband method are not included here.

where s is the expected number of signal events, b is the number of expected background events, and μ is the signal strength. The process begins by building a log-likelihood ratio test statistic

$$q_\mu = -2 \ln \frac{\mathcal{L}(\mu, \hat{\hat{\theta}})}{\mathcal{L}(\hat{\mu}, \hat{\theta})}. \tag{8.5}$$

$\hat{\hat{\theta}}$ is a conditional maximum likelihood estimator of the nuisance parameters for a given signal strength, μ. $\hat{\mu}$ and $\hat{\theta}$ are unconditional maximum likelihood estimators for the signal strength and nuisance parameters.

Using this test statistic, we can build probability distribution functions for signal plus background, and background-only hypotheses. The p-value for an observed value of q_μ with the background plus signal hypothesis is p_μ, and the background-only hypothesis p-value is p_b. Next, we define the CLs value

$$\mathrm{CL_s} = \frac{p_\mu}{1 - p_b}. \tag{8.6}$$

We find the value of μ such that the CLs value is 0.05 to give us the 95% upper limit on the signal strength. To obtain the expected upper limit, we use Monte Carlo of the

background-only hypothesis to obtain a distribution of $\mu_{95\%}$ for each mass point. If an upper limit value for a given mass point falls below 1, then we say that mass hypothesis has been excluded at the 95% confidence level. The excluded mass values are give in Table 8.9, and the upper limits on the signal strength are shown in Figures 8.7 and 8.8.

Benchmark Point	Expected (GeV)	Observed (GeV)
100% ee	564	564
100% $e\mu$	580	580
100% $\mu\mu$	585	585
BP1	388	388
BP2	490	490
BP3	506	506
BP4	436	436

Table 8.9: We exclude at 95% CL hypothesized mass values of the doubly charged Higgs at the quoted mass values and lower. The expected values reflect a background-only hypothesis. As no events are observed for mass points above 200 GeV, the observed values are the same as the expected.

The previously published CMS analysis performed a search for a doubly charged Higgs utilizing the 7 TeV dataset of 4.9 fb^{-1} [37]. They performed the search considering electron, muon, and tau final states, as well as the same branching ratio scenarios presented in this thesis. Additionally, they combined results from associated and pair-production modes of a doubly charged Higgs. They exclude masses 169 to 395 GeV, depending on the branching ratio scenario. Use of the 8 TeV dataset significantly extends the reach of the analysis, even when only considering light leptons and pair-production. The most recent 8 TeV ATLAS results are comparable to those shown in this thesis, as they exclude masses 468 to 551 GeV for a left-handed doubly charged Higgs, and they only consider pair-production with light-lepton final states [39].

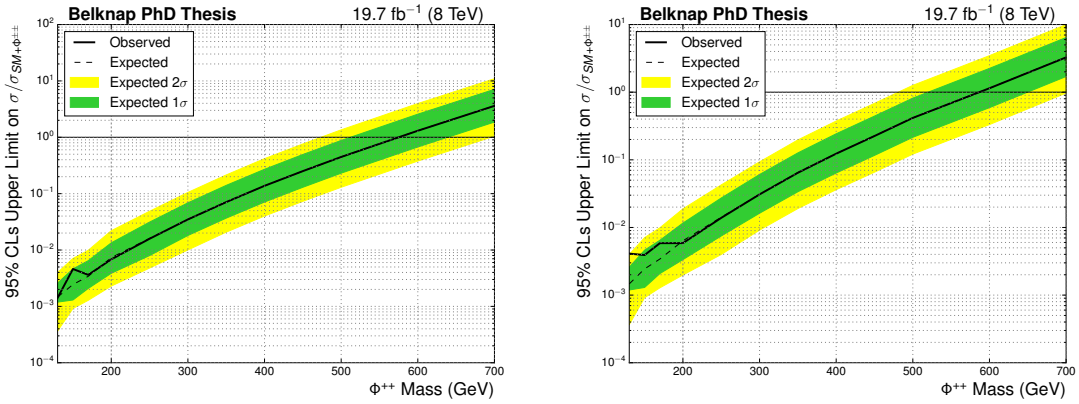

(a) 100% ee

(b) 100% $e\mu$

(c) 100% $\mu\mu$

Figure 8.7: Upper limits at 95% CL when the doubly charged Higgs is assumed to decay 100% to a specific lepton pair. Expected limits are given assuming a background-only hypothesis. The central expected value is shown as a dashed line, and the uncertainty is indicated by the green and yellow bands. The observed values are indicated by a solid black line.

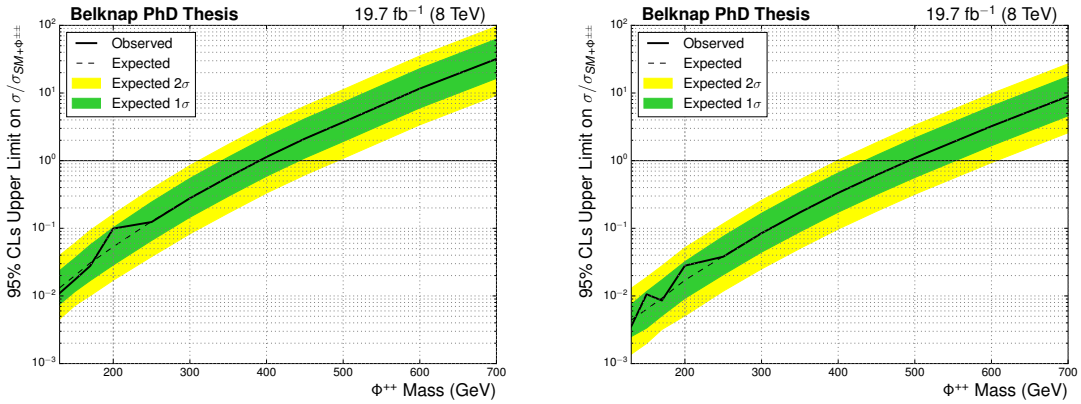

(a) BP1

(b) BP2

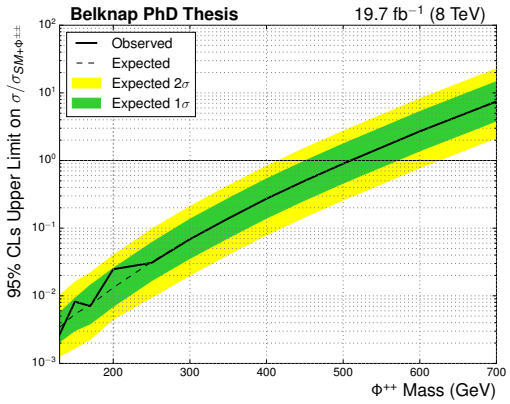

(c) BP3

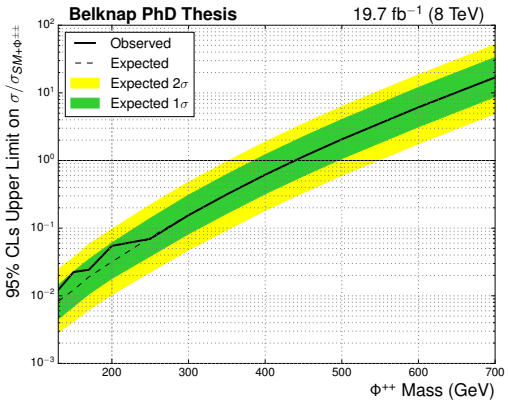

(d) BP4

FIGURE 8.8: Upper limits at 95% CL when the doubly charged Higgs decays according to benchmark points 1-4. Expected limits are given assuming a background-only hypothesis. The central expected value is shown as a dashed line, and the uncertainty is indicated by the green and yellow bands. The observed values are indicated by a solid black line.

9 Summary

Presented here are two analyses which utilize $19.7\,\text{fb}^{-1}$ of 8 TeV LHC proton-proton collision data collected by the CMS experiment: measurement of the spin and parity of the Higgs boson with a mass near 126 GeV, and a search for a doubly charged Higgs boson. These analyses use four-lepton final states, where the leptons include electrons and muons. The leptons are well-identified, well-reconstructed, and isolated.

The spin-parity analysis is performed in the $H \to ZZ \to 4\ell$ channel. Because we consider only electrons and muons, we can fully and precisely reconstruct the kinematics of the event. Additionally, this channel has few and well-understood backgrounds, namely Standard Model ZZ production. This makes this channel very well suited for precision studies of the Higgs boson's properties. The analysis compares the Standard Model pure-scalar, 0^+, hypothesis against four alternate spin-parity hypotheses: 0^-, 0_h^+, $2_m^+(gg)$, and $2_m^+(q\bar{q})$. The data were consistent with the Standard Model expectations in all cases, and the 0^- pseudoscalar hypothesis is excluded at the 95% confidence level.

The doubly charged Higgs analysis searches for the doubly charged component of a Higgs triplet, $(\Phi^0,\ \Phi^+,\ \Phi^{++})$, which is a Type II "seesaw" mechanism. We search for pair production of the doubly charged Higgs which results in a four-lepton final state. The backgrounds are estimated using a data-driven technique, although Standard Model ZZ and $t/t\bar{t}$ processes are the dominant backgrounds. As the branching ratios of the doubly charged Higgs are not fixed by the model, we consider cases where we assume 100% decays

to ee, $e\mu$, and $\mu\mu$ lepton pairs. Additionally, we consider four alternate branching ratio configurations, or "benchmark points", which combine various final state possibilities. The lower expected upper limit at 95% CL on the mass of the doubly charged Higgs is 388 GeV for the benchmark points, and 564 GeV for the 100% BR scenarios. The observed upper limits are the same as the expected, as no events are observed for mass hypotheses above 200 GeV.

9.1 Looking Forward

For the spin-parity analysis, the choice of testing the Standard Model against a selection of specific spin-parity configurations was motivated by the limited amount of data collected so far. A more ideal method of performing the measurement is to fit the coupling parameters of a Higgs boson effective Lagrangian to the data. Because of the number of parameters involved in the fit, performing it requires more data than is currently available. The LHC is beginning Run II at 13 TeV, and is expected to collect $\sim 100\,\text{fb}^{-1}$ of data, so more rigorous studies of Higgs boson properties are in the near future. Analyses conducted on the Higgs boson properties by the CMS and ATLAS collaborations show the boson to be consistent with Standard Model expectations. More precise analyses may reveal deviations (if any exist) from the Standard Model, and the Higgs boson could become a gateway for probing new physics.

For the doubly charged Higgs search, we see a significant improvement in sensitivity at higher mass hypotheses. The 7 TeV CMS analysis was performed with $4.9\,\text{fb}^{-1}$ of data, and the analysis presented in this thesis was performed with $19.7\,\text{fb}^{-1}$ of 8 TeV data, which extended the highest excluded mass hypothesis from 395 to 585 GeV. With $\sim 100\,\text{fb}^{-1}$ of 13 TeV of proton-proton collision data, we can expect to see dramatic improvements in the mass reach of future searches for a doubly charged Higgs boson at the LHC.

References

[1] D. J. Griffiths, *Introduction to elementary particles; 2nd rev. version.* Physics textbook. Wiley, New York, NY, 2008.

[2] **Particle Data Group** Collaboration, K. Olive *et al.*, "Review of Particle Physics," *Chin.Phys.* **C38** (2014) 090001.

[3] E. Giusarma, R. de Putter, S. Ho, and O. Mena, "Constraints on neutrino masses from Planck and Galaxy Clustering data," *Phys.Rev.* **D88** no. 6, (2013) 063515, arXiv:1306.5544 [astro-ph.CO].

[4] M. Kadastik, M. Raidal, and L. Rebane, "Direct determination of neutrino mass parameters at future colliders," *Phys.Rev.* **D77** (2008) 115023, arXiv:0712.3912 [hep-ph].

[5] F. Halzen and A. Martin, *Quarks and leptons: an introductory course in modern particle physics.* Wiley, 1984.

[6] S. Glashow, "Partial Symmetries of Weak Interactions," *Nucl.Phys.* **22** (1961) 579–588.

[7] S. Weinberg, "A Model of Leptons," *Phys.Rev.Lett.* **19** (1967) 1264–1266.

[8] A. Salam, "Weak and Electromagnetic Interactions," *Conf.Proc.* **C680519** (1968) 367–377.

[9] P. W. Higgs, "Broken Symmetries and the Masses of Gauge Bosons," *Phys.Rev.Lett.* **13** (1964) 508–509.

[10] F. Englert and R. Brout, "Broken Symmetry and the Mass of Gauge Vector Mesons," *Phys.Rev.Lett.* **13** (1964) 321–323.

[11] G. S. Guralnik, C. R. Hagen, and T. W. B. Kibble, "Global Conservation Laws and Massless Particles," *Phys.Rev.Lett.* **13** (1964) 585–587.

[12] Y. Gao, A. V. Gritsan, Z. Guo, K. Melnikov, M. Schulze, *et al.*, "Spin determination of single-produced resonances at hadron colliders," *Phys.Rev.* **D81** (2010) 075022, arXiv:1001.3396 [hep-ph].

[13] A. Menon, T. Modak, D. Sahoo, R. Sinha, and H.-Y. Cheng, "Inferring the nature of the boson at 125–126 GeV," *Physical Review D* **89** no. 9, (May, 2014) 095021.

[14] J. Lesgourgues and S. Pastor, "Massive neutrinos and cosmology," *Phys. Rept.* **429** (2006) 307–379, arXiv:astro-ph/0603494 [astro-ph].

[15] **CMS** Collaboration, V. Khachatryan *et al.*, "Observation of the diphoton decay of the Higgs boson and measurement of its properties," *Eur. Phys. J.* **C74** no. 10, (2014) 3076, arXiv:1407.0558 [hep-ex].

[16] **ATLAS** Collaboration, G. Aad *et al.*, "Measurements of Higgs boson production and couplings in diboson final states with the ATLAS detector at the LHC," *Phys.Lett.* **B726** (2013) 88–119, arXiv:1307.1427 [hep-ex].

[17] **LEP Working Group for Higgs boson searches, ALEPH, DELPHI, L3, OPAL** Collaboration, R. Barate *et al.*, "Search for the standard model Higgs boson at LEP," *Phys.Lett.* **B565** (2003) 61–75, arXiv:hep-ex/0306033 [hep-ex].

[18] **CDF, D0** Collaboration, T. Aaltonen *et al.*, "Combination of Tevatron searches for the standard model Higgs boson in the W+W- decay mode," *Phys.Rev.Lett.* **104** (2010) 061802, arXiv:1001.4162 [hep-ex].

[19] **CMS** Collaboration, S. Chatrchyan *et al.*, "Observation of a new boson at a mass of 125 GeV with the CMS experiment at the LHC," *Phys.Lett.* **B716** (2012) 30–61, arXiv:1207.7235 [hep-ex].

[20] **CDF, D0** Collaboration, T. Aaltonen *et al.*, "Higgs Boson Studies at the Tevatron," *Phys. Rev.* **D88** no. 5, (2013) 052014, arXiv:1303.6346 [hep-ex].

[21] **ATLAS, CMS** Collaboration, G. Aad *et al.*, "Combined Measurement of the Higgs Boson Mass in pp Collisions at $\sqrt{s} = 7$ and 8 TeV with the ATLAS and CMS Experiments," *Phys.Rev.Lett.* **114** (2015) 191803, arXiv:1503.07589 [hep-ex].

[22] **CMS** Collaboration, S. Chatrchyan *et al.*, "Measurement of the properties of a Higgs boson in the four-lepton final state," *Phys.Rev.* **D89** no. 9, (2014) 092007, arXiv:1312.5353 [hep-ex].

[23] **CMS** Collaboration, S. Chatrchyan *et al.*, "Study of the Mass and Spin-Parity of the Higgs Boson Candidate Via Its Decays to Z Boson Pairs," *Phys.Rev.Lett.* **110** no. 8, (2013) 081803, arXiv:1212.6639 [hep-ex].

[24] I. Anderson, S. Bolognesi, F. Caola, Y. Gao, A. V. Gritsan, *et al.*, "Constraining anomalous HVV interactions at proton and lepton colliders," *Phys.Rev.* **D89** no. 3, (2014) 035007, arXiv:1309.4819 [hep-ph].

[25] S. Bolognesi, Y. Gao, A. V. Gritsan, K. Melnikov, M. Schulze, *et al.*, "On the spin and parity of a single-produced resonance at the LHC," *Phys.Rev.* **D86** (2012) 095031, arXiv:1208.4018 [hep-ph].

[26] **CMS** Collaboration, S. Chatrchyan *et al.*, "Measurement of Higgs boson production and properties in the WW decay channel with leptonic final states," *JHEP* **1401** (2014) 096, arXiv:1312.1129 [hep-ex].

[27] **ATLAS** Collaboration, G. Aad *et al.*, "Evidence for the spin-0 nature of the Higgs boson using ATLAS data," *Phys.Lett.* **B726** (2013) 120–144, arXiv:1307.1432 [hep-ex].

[28] **CDF, D0** Collaboration, T. Aaltonen *et al.*, "Tevatron Constraints on Models of the Higgs Boson with Exotic Spin and Parity Using Decays to Bottom-Antibottom Quark Pairs," *Phys. Rev. Lett.* **114** no. 15, (2015) 151802, arXiv:1502.00967 [hep-ex].

[29] M. L. Swartz, "Limits on Doubly Charged Higgs Bosons and Lepton Flavor Violation," *Phys.Rev.* **D40** (1989) 1521.

[30] M. L. Swartz, G. Abrams, C. Adolphsen, D. Averill, J. Ballam, *et al.*, "A Search for Doubly Charged Higgs Scalars in Z Decay," *Phys.Rev.Lett.* **64** (1990) 2877–2880.

[31] **L3** Collaboration, P. Achard *et al.*, "Search for doubly charged Higgs bosons at LEP," *Phys.Lett.* **B576** (2003) 18–28, arXiv:hep-ex/0309076 [hep-ex].

[32] **OPAL** Collaboration, G. Abbiendi *et al.*, "Search for doubly charged Higgs bosons with the OPAL detector at LEP," *Phys.Lett.* **B526** (2002) 221–232, arXiv:hep-ex/0111059 [hep-ex].

[33] **DELPHI** Collaboration, J. Abdallah *et al.*, "Search for doubly charged Higgs bosons at LEP-2," *Phys.Lett.* **B552** (2003) 127–137, arXiv:hep-ex/0303026 [hep-ex].

[34] **CDF** Collaboration, D. Acosta *et al.*, "Search for doubly-charged Higgs bosons decaying to dileptons in $p\bar{p}$ collisions at $\sqrt{s} = 1.96$ TeV," *Phys.Rev.Lett.* **93** (2004) 221802, arXiv:hep-ex/0406073 [hep-ex].

[35] **CDF** Collaboration, T. Aaltonen *et al.*, "Search for Doubly Charged Higgs Bosons with Lepton-Flavor-Violating Decays involving Tau Leptons," *Phys.Rev.Lett.* **101** (2008) 121801, arXiv:0808.2161 [hep-ex].

[36] **D0** Collaboration, V. Abazov *et al.*, "Search for pair production of doubly-charged Higgs bosons in the $H^{++}H^{--} \to \mu^+\mu^+\mu^-\mu^-$ final state at D0," *Phys.Rev.Lett.* **101** (2008) 071803, arXiv:0803.1534 [hep-ex].

[37] **CMS** Collaboration, S. Chatrchyan *et al.*, "A search for a doubly-charged Higgs boson in pp collisions at $\sqrt{s} = 7$ TeV," *Eur.Phys.J.* **C72** (2012) 2189, arXiv:1207.2666 [hep-ex].

[38] **ATLAS** Collaboration, G. Aad *et al.*, "Search for doubly-charged Higgs bosons in like-sign dilepton final states at $\sqrt{s} = 7$ TeV with the ATLAS detector," *Eur.Phys.J.* **C72** (2012) 2244, arXiv:1210.5070 [hep-ex].

[39] **ATLAS** Collaboration, G. Aad *et al.*, "Search for anomalous production of prompt same-sign lepton pairs and pair-produced doubly charged Higgs bosons with $\sqrt{s} = 8$ TeV pp collisions using the ATLAS detector," *JHEP* **1503** (2015) 041, arXiv:1412.0237 [hep-ex].

[40] **CMS** Collaboration, S. Chatrchyan *et al.*, "The CMS experiment at the CERN LHC," *JINST* **3** (2008) S08004.

[41] L. Evans and P. Bryant, "LHC Machine," *JINST* **3** (2008) S08001.

[42] N. Metropolis and S. Ulam, "The monte carlo method," *Journal of the American Statistical Association* **44** no. 247, (1949) 335–341.

[43] H.-L. Lai, M. Guzzi, J. Huston, Z. Li, P. M. Nadolsky, *et al.*, "New parton distributions for collider physics," *Phys.Rev.* **D82** (2010) 074024, arXiv:1007.2241 [hep-ph].

[44] A. Martin, W. Stirling, R. Thorne, and G. Watt, "Parton distributions for the LHC," *Eur.Phys.J.* **C63** (2009) 189–285, arXiv:0901.0002 [hep-ph].

[45] R. D. Ball, L. Del Debbio, S. Forte, A. Guffanti, J. I. Latorre, *et al.*, "A first unbiased global NLO determination of parton distributions and their uncertainties," *Nucl.Phys.* **B838** (2010) 136–206, arXiv:1002.4407 [hep-ph].

[46] B. Andersson, G. Gustafson, G. Ingelman, and T. Sjostrand, "Parton Fragmentation and String Dynamics," *Phys.Rept.* **97** (1983) 31–145.

[47] B. Webber, "Parton shower Monte Carlo event generators," *Scholarpedia* **6** no. 12, (2011) 10662. revision 128236.

[48] T. Sjostrand, S. Mrenna, and P. Z. Skands, "PYTHIA 6.4 Physics and Manual," *JHEP* **0605** (2006) 026, arXiv:hep-ph/0603175 [hep-ph].

[49] J. Alwall, R. Frederix, S. Frixione, V. Hirschi, F. Maltoni, *et al.*, "The automated computation of tree-level and next-to-leading order differential cross sections, and their matching to parton shower simulations," *JHEP* **1407** (2014) 079, arXiv:1405.0301 [hep-ph].

[50] J. Alwall, P. Demin, S. de Visscher, R. Frederix, M. Herquet, *et al.*, "MadGraph/MadEvent v4: The New Web Generation," *JHEP* **0709** (2007) 028, arXiv:0706.2334 [hep-ph].

[51] C. Oleari, "The POWHEG-BOX," *Nucl.Phys.Proc.Suppl.* **205-206** (2010) 36–41, arXiv:1007.3893 [hep-ph].

[52] T. Binoth, N. Kauer, and P. Mertsch, "Gluon-induced QCD corrections to $pp \to ZZ \to \ell\bar{\ell}\ell'\bar{\ell}'$," arXiv:0807.0024 [hep-ph].

[53] **LHC Higgs Cross Section Working Group** Collaboration, S. Heinemeyer *et al.*, "Handbook of LHC Higgs Cross Sections: 3. Higgs Properties," arXiv:1307.1347 [hep-ph].

[54] **GEANT4** Collaboration, S. Agostinelli *et al.*, "GEANT4: A Simulation toolkit," *Nucl.Instrum.Meth.* **A506** (2003) 250–303.

[55] **CMS** Collaboration, "Electron reconstruction and identification at sqrt(s) = 7 TeV,".

[56] W. Adam, R. Fruhwirth, A. Strandlie, and T. Todorov, "Reconstruction of electrons with the Gaussian sum filter in the CMS tracker at LHC," *eConf* **C0303241** (2003) TULT009, arXiv:physics/0306087 [physics].

[57] **CMS** Collaboration, S. Chatrchyan *et al.*, "Performance of CMS muon reconstruction in pp collision events at $\sqrt{s} = 7$ TeV," *JINST* **7** (2012) P10002, arXiv:1206.4071 [physics.ins-det].

[58] R. Fruhwirth, "Application of Kalman filtering to track and vertex fitting," *Nucl.Instrum.Meth.* **A262** (1987) 444–450.

[59] **CMS** Collaboration, "Particle-Flow Event Reconstruction in CMS and Performance for Jets, Taus, and MET,".

[60] M. Cacciari and G. P. Salam, "Pileup subtraction using jet areas," *Phys.Lett.* **B659** (2008) 119–126, arXiv:0707.1378 [hep-ph].

[61] M. Cacciari, G. P. Salam, and G. Soyez, "The Catchment Area of Jets," *JHEP* **0804** (2008) 005, arXiv:0802.1188 [hep-ph].

[62] B. P. Roe, H.-J. Yang, J. Zhu, Y. Liu, I. Stancu, *et al.*, "Boosted decision trees, an alternative to artificial neural networks," *Nucl.Instrum.Meth.* **A543** no. 2-3, (2005) 577–584, arXiv:physics/0408124 [physics].

[63] **CMS** Collaboration, "Electron performance with 19.6 fb^{-1} of data collected at $\sqrt{s} = 8$ TeV with the CMS detector.,".

[64] Y. Chen *et al.*, "Electron energy reconstruction using a multivariate regression," *CMS AN* **2012/327** (2012) .

[65] F. Beaudette *et al.*, "Electron momentum determination using boosted regression trees," *CMS AN* **2013/209** (2013) .

[66] M. S. M. Donega and D. Futyan, "Updated measurements of the new Higgs-like boson at 125 GeV in the two photon decay channel," *CMS AN* **2012/374** (2012) .

[67] **CMS** Collaboration, "Commissioning of the Particle-Flow reconstruction in Minimum-Bias and Jet Events from pp Collisions at 7 TeV,".

[68] **CMS** Collaboration, "Particle-flow commissioning with muons and electrons from J/Psi and W events at 7 TeV,".

[69] **CMS** Collaboration, S. Chatrchyan *et al.*, "Measurement of the Inclusive W and Z Production Cross Sections in pp Collisions at $\sqrt{s} = 7$ TeV," *JHEP* **1110** (2011) 132, arXiv:1107.4789 [hep-ex].

[70] A. Menon, T. Modak, D. Sahoo, R. Sinha, and H.-Y. Cheng, "Inferring the nature of the boson at 125-126 GeV," *Phys.Rev.* **D89** no. 9, (2014) 095021, arXiv:1301.5404 [hep-ph].

[71] J. M. Campbell and R. Ellis, "MCFM for the Tevatron and the LHC," *Nucl.Phys.Proc.Suppl.* **205-206** (2010) 10–15, arXiv:1007.3492 [hep-ph].

[72] S. Alekhin, S. Alioli, R. D. Ball, V. Bertone, J. Blumlein, *et al.*, "The PDF4LHC Working Group Interim Report," arXiv:1101.0536 [hep-ph].

[73] N. Amapane *et al.*, "Measurement of the production and decay of a higgs boson in the four-lepon final state," *CMS AN* **2013/108** (2013) .

[74] G. Cowan, K. Cranmer, E. Gross, and O. Vitells, "Asymptotic formulae for likelihood-based tests of new physics," *Eur.Phys.J.* **C71** (2011) 1554, arXiv:1007.1727 [physics.data-an].